Titre: Title:	Additive Manufacturing of Low and High Temperature Resistant Thermoplastic Composites and Sandwich Panels for Sound Absorption
Auteur: Author:	Filippo Iervolino
Date:	2019
Type:	Mémoire ou thèse / Dissertation or Thesis
Référence: Citation:	Iervolino, F. (2019). Additive Manufacturing of Low and High Temperature Resistant Thermoplastic Composites and Sandwich Panels for Sound Absorption [Mémoire de maîtrise, Polytechnique Montréal]. PolyPublie. https://publications.polymtl.ca/4051/

POLYTECHNIQUE MONTRÉAL

affiliée à l'Université de Montréal

Additive Manufacturing of Low and High Temperature Resistant Thermoplastic Composites and Sandwich Panels for Sound Absorption

FILIPPO IERVOLINO

Département de génie mécanique

Mémoire présenté en vue de l'obtention du diplôme de *Maîtrise ès sciences appliquées*

Génie mécanique

Août 2019

POLYTECHNIQUE MONTRÉAL

affiliée à l'Université de Montréal

Ce mémoire intitulé :

Additive Manufacturing of Low and High Temperature Resistant Thermoplastic Composites and Sandwich Panels for Sound Absorption

présenté par **Filippo IERVOLINO**

en vue de l'obtention du diplôme de *Maîtrise ès sciences appliquées*

a été dûment accepté par le jury d'examen constitué de :

Louis Laberge Lebel, président

Daniel Therriault, membre et directeur

Annie Ross, membre

DEDICATION

“you do not just wake up and become the butterfly”

Rupi Kaur

ACKNOWLEDGEMENTS

Firstly, I would like to express my most sincere gratitude to my research supervisor, Professor Daniel Therriault, for having accepted me inside the project and for the financial support. He was a guide and a source of inspiration for me, and he has made me a better researcher and a better person with his suggestions.

Then, I would like to thank Safran Composites and in particular Dr. Nicola Piccirelli for all the feedbacks and suggestions received during the project that helped me to take the right path.

Ina addition, I would like to thank Polytechnique Montréal and *Politecnico di Milano* for giving me the opportunity to do this double degree program and live this unforgettable experience in Montréal.

Moreover, I would like to thank all the LM2 members that worked with me on this project: Dr. Rouhollah Faharani, Yahya Abdeffarai, Dr. Ivonne Otero Navas, Dr. Audrey Diouf-Lewis, Juliette Pierre and Dr. Kambiz Chizari. Working with you was a pleasure and I could not ask for better teammates. I thank also all the other LM2 members, especially Jean-François, Alessandra, Anton, Facundo, Clément, Rui, Shibo and Zana.

I would also like to thank all the people that helped me carrying out the experiments: Matthieu Gauthier for the trainings and suggestions for the polymer characterization, Dr. Ilyass Tabbiai for the help with the DIC, Josué Costa Baptista, Jean Boulvert and Dr. Edith Roland Fotsing for introducing me in the world of acoustic and for their fundamental suggestions, and Isabelle Nowlan for the training on the mechanical testing equipments.

Then I would like to thank my family and my girlfriend Prisca. You were my light in the darkness of my most difficult moments.

I would also like to thank my best friends from Italy, Valag, Peve, Elisa and Micol, and also the OH group: Anna, Balza, Ema, Marco, Teo, Tom, Tobi, Vera and Ciaglia. They always made me smile and helped me to fell less homesick.

Finally, I would like to thank the friends that I found in Montréal: Nicolò, Lucas, Gauthier Benjamin, Vlad, Eduardo, Marina, Ilaria and Eduardo. They were my “Canadian family” and I was lucky to find friends like them.

RÉSUMÉ

Les moteurs d'avion de nouvelle génération ont besoin d'être plus légers et silencieux pour répondre aux règlements sur les émissions de dioxyde de carbone et de pollution acoustique. Comme approche prometteuse, l'industrie aérospatiale a commencé à investiguer la technologie de fabrication additive (FA) par déposition de filament fondu (FDM, de l'anglais *Fused Deposition Modeling*) des polymères et composites. La possibilité de fabriquer des pièces légères et avec des géométrie complexes représente un de plus grands avantages. La FA des thermoplastiques résistant aux températures élevées (HTRT, de l'anglais *high temperature resistant thermoplastic*) présente un intérêt particulier en raison des températures de service relativement hautes (> 100°C) et leurs propriétés mécaniques. La flexibilité de fabrication offerte par la FA permet la fabrication de revêtements acoustiques innovants et aussi une conception plus efficace des géométries acoustiques.

Le projet a pour objectif de couvrir le traitement et la fabrication des matériaux ainsi que la fabrication de panneaux sandwich pour des applications acoustiques. En premier lieu, des composites HTRT présentant des propriétés thermiques et mécaniques améliorées ont été développés. Du Polyétheréthercétone (PEEK) et de la Polyétherimide (PEI) et des alliages PEKK / PEI ont été utilisés comme matrices polymères et ont été mélangés avec des fibres de carbone (CF, de l'anglais *Carbon fiber*) découpées avec deux stratégies de mélange différentes. Les composites mélangés ont été traités avec une machine FDM pour obtenir des filaments avec le diamètre souhaité et des éprouvettes d'essais de traction. Des caractérisations thermiques, morphologiques et mécaniques ont été effectuées. Les matériaux composites développés présentent un excellent comportement à haute température. Grâce à la température de transition vitreuse (T_g) plus élevée du PEI, les alliages PEEK/PEI ont montré une augmentation de la température de transition vitreuse jusqu'à 35°C, augmentant ainsi la température de service du matériau. La microscopie électronique à balayage et la micro-tomodensitométrie ont montré une répartition homogène des fibres et une bonne mouillabilité entre les fibres et les matrices polymères. La présence de porosité, probablement des bulles d'air incorporé au cours du processus de mélange, a été également détectée. Le module d'Young des composites HTRT développés a été évalué à l'aide d'essais de traction sur des filaments et sur des éprouvettes imprimées en 3D. En ce qui concerne les filaments, le PEEK renforcé avec 40% en masse de CF a montré les meilleures propriétés, avec

un module de 20.1 GPa. Le PEEK/PEI (80% en masse/20% en masse) renforcé avec 30% en poids de CF a donné le module d'Young le plus élevé parmi les éprouvettes de traction imprimées en 3D.

Concernant la partie acoustique du projet, différent panneaux sandwich, qui sont composés par une âme, une peau et une peau perforée, en acide polylactique, polyamide pure et renforcée avec CF destinés à l'absorption acoustique à large bande ont été fabriqués par FDM. Des cellules unitaire présentant quatre prismes trapézoïdales ont été développés et l'absorption acoustique a été évaluée à l'aide d'un tube de Kundt en mode réflexion dans la plage de fréquences 500-7000 Hz. Il a été possible d'obtenir un coefficient d'absorption toujours supérieur de 90% sur une plage de fréquences d'environ ~550 Hz. De plus, des panneaux sandwich avec les cellules acoustiques développées ont été caractérisés à l'aide d'un test de flexion trois points. Les résultats ont montré qu'une surface de contact plus élevée entre l'âme et les peaux des panneaux améliore les propriétés mécaniques de la structure et évite le délaminage. Ainsi, l'ajout des congés à l'âme des panneaux sandwich a permis d'améliorer jusqu'à trois fois la charge soutenue maximale.

En bref, le mémoire propose une approche pour mélanger, fabriquer de manière additive et caractériser les composites HTRT. Le fort potentiel des composites PEEK / PEI pour la technologie FDM a également été exploité. De plus, la fabrication par FDM des panneaux sandwich présentant une absorption acoustique à large bande et des propriétés mécaniques porteuses a été démontrée.

ABSTRACT

New generation aircraft engines need to be lighter and quieter to meet the international regulations on the reduction of both carbon dioxide and noise emissions. As a promising approach, aerospace industry has begun to investigate the utilization of Additive Manufacturing (AM) of polymers and composites for the manufacturing of lightweight structures featuring complex shapes. The AM of High Temperature Resistant Thermoplastic (HTRT) has been of particular interest due to their relative high service temperatures (>100°C) and their relatively high mechanical performance. Manufacturing flexibility offered by AM enables the fabrication of innovative acoustic liners and also a more efficient design for acoustic concepts.

This project aims to cover materials processing, manufacturing and the fabrication of sandwich panels for acoustic applications. First, HTRT composites with improved thermal and mechanical properties were developed. Polyether Ether Ketone (PEEK) and Polyetherimide (PEI) and PEEK/PEI blends were used as polymer matrices and are processed with chopped Carbon Fibers (CFs) with two different mixing strategies. The mixed composites were fed into a Fused Deposition Modeling (FDM) 3D printer to obtain 3D printed filaments having a desired diameter and also tensile test specimens. The developed composite materials were then characterized for their thermal, morphological and mechanical behavior. The materials showed excellent behavior at high temperatures. Thanks to the higher glass transition temperature (T_g) of PEI, PEEK/PEI blends showed a maximum increase in the T_g of 35°C with respect to PEEK, thus increasing the maximum service temperature of the materials. Scanning electron microscopy (SEM) and micro-computed tomography (µ-CT) scans revealed a homogeneous distribution of the fibers and a good wetting between CFs and polymer matrices. The presence of voids, probably air bubbles incorporated during the mixing process, was also detected. The Young's modulus of the developed HTRT composites was evaluated with the aid of tensile test on 3D printed filaments and tensile test specimens. Regarding the filaments, PEEK reinforced with 40wt.% of CFs showed the best mechanical properties with a Young's modulus of 20.1 GPa. For the 3D printed tensile test specimens, however, PEEK/PEI (80wt.%/20wt.%) reinforced with 30wt.% of CFs showed the highest Young's modulus (16.6 GPa).

For acoustic side of the project, various innovative sandwich panels, which are composed of a core a facesheets and a perforated facesheet, made of polylactic acid or neat and CFs reinforced polyamide for sound absorption were creteded and manufactured with FDM. Unit cell featuring four trapezoidal prism has bene developed and their sound absorption was evaluated with the aid of an impedance tube in reflection mode in the frequency range 500-7000 Hz. It was possible to obtain an absorption coefficient always higher than 90% over a frequency range of ~550 Hz. Flexural mechanical performance of the sandwich panels featuring the developed unit cells were characterized with the aid of a 3-point bending test. Results showed that a higher contact surface between core and facesheets of the panels improved the mechanical properties of the structure and avoided delamination. Thus, the addition of fillets to the core of the panels at the interface of the core and the facesheets showed an improvement in the maximum sustained load up to 3 times.

In brief, this thesis proposes an approach to process, additively manufacture and characterize HTRT composites. The high potential PEEK/PEI composites for FDM was also exploited. Moreover, FDM of sandwich panels featuring sound absorption and load-bearing mechanical properties was demonstrated.

TABLE OF CONTENTS

LIST OF TABLES

LIST OF FIGURES

LIST OF SYMBOLS AND ABBREVIATIONS

µ-CT	Micro-computed tomography
3DP	Three-dimensional printing
ABS	Acrylonitrile butadiene styrene
ACARE	Advisor council for aviation research and innovation in Europe
AM	Additive manufacturing
CAD	Computer-aided design
CF	Carbon fiber
CFR	Carbon fibers reinforced
CNC	Computer numerical tooling
CNF	Carbone nanofiber
CNT	Carbone nanotube
CO_2	Carbon dioxide
C_p	Heat capacity
CUT	Continuous use temperature
DDOF	Double degree of freedom
DIC	Direct Image Correlation
DIW	Direct Ink Writing
DMA	Dynamic mechanical analysis
D_n (mm)	Diameter of the neck
DSC	Differential scanning calorimetry
E (GPA)	Young's modulus
FAA	Federal aviation administration
FACMO	*Fabrication additive des composites à matrice organique*

FDM	Fused Deposition Modeling
FFF	Fused Filament Fabrication
FL	Flat Length
f_r (Hz)	Resonant frequency
FW	Flat width
GE	General Electric
GnP	Graphite nanoplates
HDT	Heat deflection temeprature
HTRT	High temperature resistant thermoplastic
LEAP	Leading Edge Aviation Propulsion
LM2	Laboratory for multiscale mechanics
L_n (mm)	Length of the neck
LOM	Laminated object manufacturing
LVDT	Linear variable differential transformer
m-DSC	Modulated differential scanning calorimetry
MPP	Micro-perforated panel
NRC	National Research Council of Canada
PA	Polyamide
PCHR	Perforated Composite Helmholtz Resonator
PEEK	Polyether ether ketone
PEI	Polyetherimide
PEK	Polyether ketone
PES	Polyether sulfone
PLA	Poly-lactic acid

SDOF	Single degree of freedom
SEM	Scanning electron microscopy
SLA	Stereolitography
SLS	Selective laser sintering
STL	Standard triangulation language
T_b (°C)	Printing bed temperature
T_c (°C)	Crystallization temperature
T_{ch} (°C)	Chamber temperature
T_{extr} (°C)	Extruder temperature
T_g (°C)	Glass transition temperature
TGA	Thermogravimetric analysis
TiO_2	Titanium dioxide
T_m (°C)	Melting temperature
UTS	Ultimate tensile strength
V_c (mm^3)	Volume of the cavity

LIST OF APPENDICES

CHAPTER 1 INTRODUCTION

The reduction of carbon dioxide (CO_2) and noise emissions produced by aircrafts has become a problem of major interest for the aerospace industry. In 2001, the Advisor Council for Aviation Research and innovation in Europe (ACARE) asked for a reduction of 50% for both fuel consumption and noise emissions produced by aircrafts by 2020 [1]. Given the impossibility to reach this goal, a new program has been established, setting the fuel and noise reduction at 75% and 65% for 2050, respectively [2].

The reduction in weight of the aircrafts, the development of more efficient sound absorbers and the use of multi-functional parts can help to achieve these goals. Nowadays, aircraft manufactures are more and more substituting heavy metallic components with lighter ones made of composite materials. For example , the BOEING 787 is made by 50% by weight of composite materials [3], while the Airbus A350 XWB by 53% by weight [4].The trend of implementing more and more composite materials to reduce the weight is also followed by engines manufacturers. For example, Safran S.A and General Electric (GE) produced the Leading Edge Aviation Propulsion (LEAP) engines, whose fan blades and fan case are made of 3D woven composites [5].

However, aircraft components need to have good mechanical properties while being lighter and more durable. To achieve this challenge, novel fabrication approaches have been employed. One of them is Additive Manufacturing (AM) [6]. AM, otherwise known as three-dimensional printing (3DP), is a fabrication technology based on the addition or the junction of material to obtain the desired geometry using a layer-by layer process. Firstly, the part is modelled using a Computer-Aided Design (CAD) software, then a Standard Triangulation Language (STL) file is created, finally the file is imported in the AM machine and, once the processing parameters are set, the part can be fabricated [7]. Aerospace companies and space agencies such as GE aviation, Safran S.A and NASA, are already using additively manufactured components. GE has produced the fuel nozzle of the Leap Engine through AM, replacing a 20 components assembly with a single part reducing cost and weight. Safran S.A. is implementing AM for the fabrication of functional prototypes and engine’s components. For example, AM was successfully used for engine stator vanes. Finally, NASA fabricated rockets injector through an AM process, drastically reducing the manufacturing time [6].

Nevertheless, the abovementioned examples refer to the AM of metallic components. AM of polymers or composites is not as advanced as the one for metals. The substitution of metallic components with polymeric ones has another obstacle: polymeric materials cannot be used if the service temperature is high. Here, the needs of both improving the AM of polymers to fabricate aerospace certified structures and developing new materials with improved thermal resistance.

The present project aims to address these two challenges. The project is carried out at the Laboratory for Multiscale Mechanics (LM2) in collaboration with the French company Safran Composites in the Framework of the FACMO (*Fabrication Additive des Composites à Matrice Organique*) industrial chair. The research activities for FACMO has a duration of five years. The thesis project covers the first two years of the FACMO industrial chair.

The thesis covers two topics: (i) the development and fabrication with Fused Deposition Modeling (FDM) of thermoplastic composites having high service temperatures and (ii) the development of multi-functional sandwich panels featuring load-bearing mechanical capabilities and noise attenuation. More precisely, for the first topic Polyether Ether Ketone (PEEK) and Polyetherimide (PEI) thermoplastic polymers will be mixed with short carbon fibers (CFs). Their thermal and mechanical properties will be evaluated to achieve the highest glass transition temperature (T_g) and Young's modulus (E) values possible while maintaining the ease of fabrication. For the second topic, sandwich panels featuring multiple Helmholtz Resonator will be developed and acoustically characterized. The sandwich panels featuring the developed resonators will be initially fabricated with Polylactic Acid (PLA) and then with Polyamide (PA).

The thesis is organized as follows. Chapter 2 presents the literature review, focusing on the FDM process, the use of high temperature thermoplastics and its application in the acoustic domain. Chapter 3 explains the objectives of the project. Then, Chapter 4 is devoted to the development of PEEK and PEI based composites for FDM. In Chapter 5, the fabrication of acoustic samples and sandwich panels is presented. Finally, Chapter 6 contains the overall conclusions and recommendations.

CHAPTER 2 LITERATURE REVIEW

In this chapter, a comprehensive literature review on the different AM technologies will be provided. Then the focus will be on the AM of thermoplastic polymers and composites, with particular interest for the FDM process. The principal thermoplastic polymers and composites that can be used will be explained, including High Temperature Resistant Thermoplastic (HTRT) polymers and composites. Possible applications of AM will be exposed, focusing on noise absorbing structures, including acoustic sandwich panels.

2.1 Overview of AM technologies

AM technologies have several advantages over traditional fabrication technologies. It allows producing complex parts that would not be feasible with traditional manufacturing technologies, eliminating most geometrical restrictions on the design. Moreover, additively manufactured parts do not require additional operations, except for post-processing machining if good surface finish or more precise dimensions are required. In addition, AM technologies lead to a significant reduction of waste material, contributing to the reduction of costs. However, some limitations are also present. Firstly, this technology is not suitable for high volume manufacturing, since it is usually characterized by slow build rates, i.e., 0.1-100 mm/s. Then, industrial type high-end printers have a high cost, requiring an investment for the purchase. Finally, each AM technology is material specific and, consequently, not versatile [8], [9].

Several AM technologies exist depending on the used material and the solidification mechanism involved. According to ISO/ASTM 52900:2015 (E) ‘‘Standard Terminology for Additive Manufacturing – General principles – Terminology’’ [10], a first classification can be done between single-step and multi-step AM processes. The former refers to an AM process in which both the basic geometry and fundamental properties of the material are generated in one single step, while the latter indicates a process in which the basic geometry is acquired in a first process and the physical and chemical properties of the material in a second one. An example of a multiple-step process could be the formation of the geometry layer-by-layer with the aid of a binder (first step) and subsequent sintering to consolidate the part (second step).

A second type of classification is based on the adopted materials (i.e., metals, polymers and ceramics). For each of the materials categories, AM technologies are regrouped in different process categories:

- metals: direct energy deposition, powder bed fusion, sheet lamination;
- polymers: material extrusion, material jetting, powder bed fusion, binder jetting, vat photopolymerization, sheet lamination;
- ceramics: powder bed fusion.

Moreover, each of these categories is characterized by a specific AM principle, material distribution, material feedstock, and state of fusion. Figure 2.1 shows a summary on the different process categories and their characteristic of single-step AM process for polymers. [10]

For the purpose of this literature review, only single-step processes for polymers will be considered. In Section 2.1.1 the working principle of each process category for single-step AM of polymers will be explained.

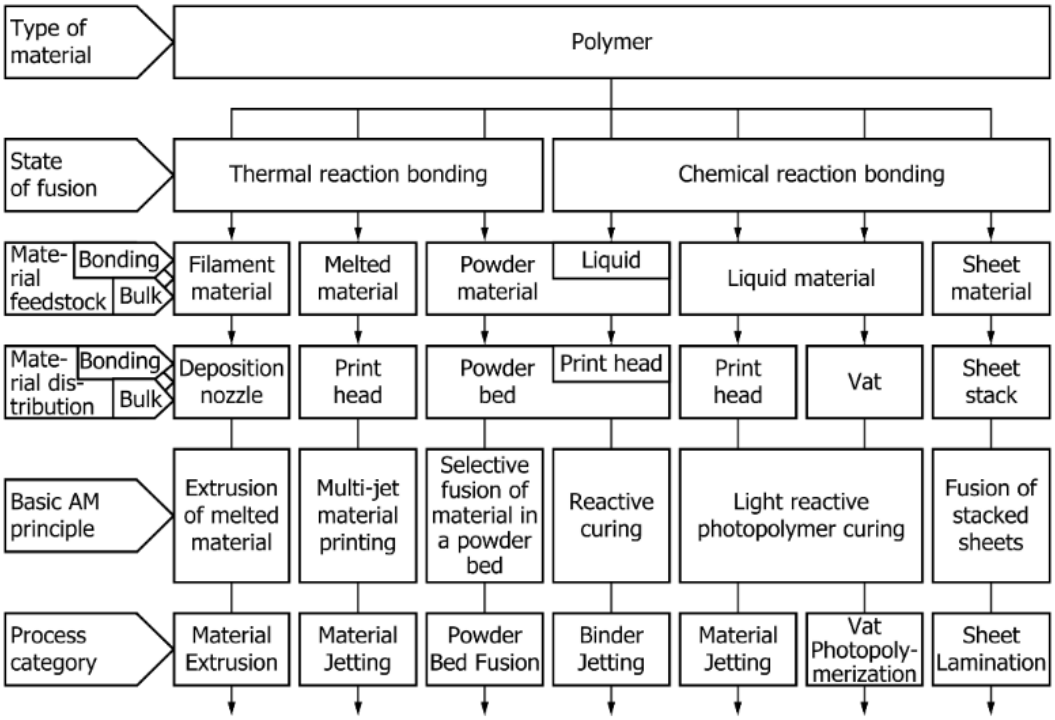

Figure 2.1 Schematic of single-step AM processes for polymers.
Adapted with permission from [10]

2.1.1 AM technologies for polymers

Figure 2.2 represents the working principle of the main AM technologies for polymers. AM for polymeric materials can be divided in five main groups: vat photopolymerization, powder bed fusion, sheet lamination, inkjet printing and material extrusion.

Vat photopolymerization is an AM process in which a photopolymer, in liquid form, is selectively cured by light-based radiation. Thus, a light source, e.g., a laser, targets selectively the liquid resin solidifying it layer-by layer (Figure 2.2a) [11]. Powder bed fusion process relies on the local fusion or sintering of a powder of thermoplastic polymeric material. A roll spreads the powder on the building platform. A laser locally heats up the polymeric powder until the powder particles bond together due to material fusion or sintering (Figure 2.2b) [9], [12]. Inkjet printing is an AM category that is based on the ejection of droplets of an ink through a nozzle. Binder jetting, also known as three dimensional printing technique, is one of the technologies that is included in this group. It relies on particles solidification by mean of a liquid binder. A liquid binder is selectively deposited on the powder to create the geometry. Particles are bonded together thanks to the binder solidification. (Figure 2.2c) [11], [13], [14]. Sheet lamination, also know as Laminated Object Manufacturing (LOM), relies on stacking of sheet materials, which are covered by an adhesive. The adhesive creates the bonding between successive sheets and it can be applied before or during the stacking procedure (Figure 2.2d) [7], [12]. Material extrusion processes includes AM technologies that relies on the continuous deposition of inks or melted polymeric filaments. The deposition of inks is also known as Direct Ink Writing (DIW) [15]–[17]. Inks used in DIW have a shear-thinning behaviour, i.e. the viscosity lowers when increasing the applied shear rate. Figure 2.2e shows the extrusion process using three different techniques (i.e. pneumatic, piston and screw). During the extrusion a shear rate is applied on the material, lowering its viscosity and allowing the extrusion. The ink filaments are deposited layer-by-layer until the whole geometry is fabricated. The main advantages of this technology are its flexibility and the low processing cost. In addition, it is a room temperature process. However, materials available for this technology usually possess weak mechanical properties, therefore the addition of filler is often necessary [10], [13]. Material extrusion of melted polymers is known as FDM, also called Fused Filament Fabrication (FFF) and it will be explained in detail in Section 2.2.

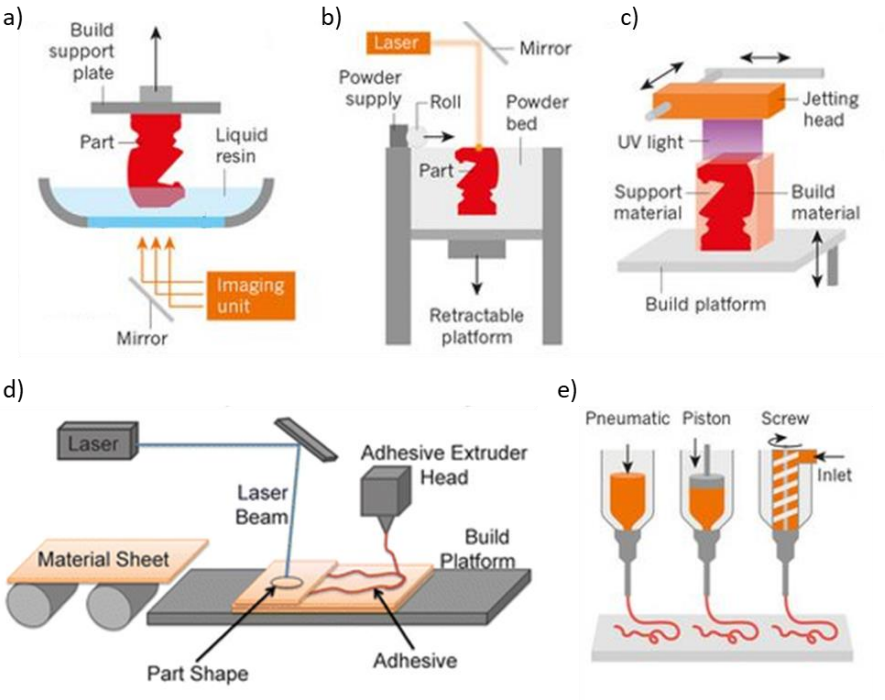

Figure 2.2 Schematics representing the working principle of a) vat photopolymerization, b) powder bed fusion, c) inkjet printing, d) sheet lamination, and e) material extrusion. Adapted with permission from [18], [19]

2.2 Fused deposition modeling

FDM is one of the most popular AM technologies. It was developed by Scott Crump, cofounder and chairman of Stratasys, Ltd., in 1992, with the release of a patent [7], [12], [20], [21]. Figure 2.3 shows the working principle of FDM AM technology. A filament of a thermoplastic polymer is fed into a heated nozzle, placed on a moving head, i.e. printing head [12], [18]. The nozzle is set at a temperature higher than the melting temperature (T_m) or the T_g for semi-crystalline and amorphous polymer, respectively [22]. The polymeric filament, then, is extruded through the nozzle and deposited on the building platform or printing bed. After the extrusion, the material cools down and solidifies [18], [22]. Once a layer is fabricated, the platform lowers or the printing head is elevated on the *z*-direction and a new layer is printed. The process is repeated for each layer until the whole geometry is built.

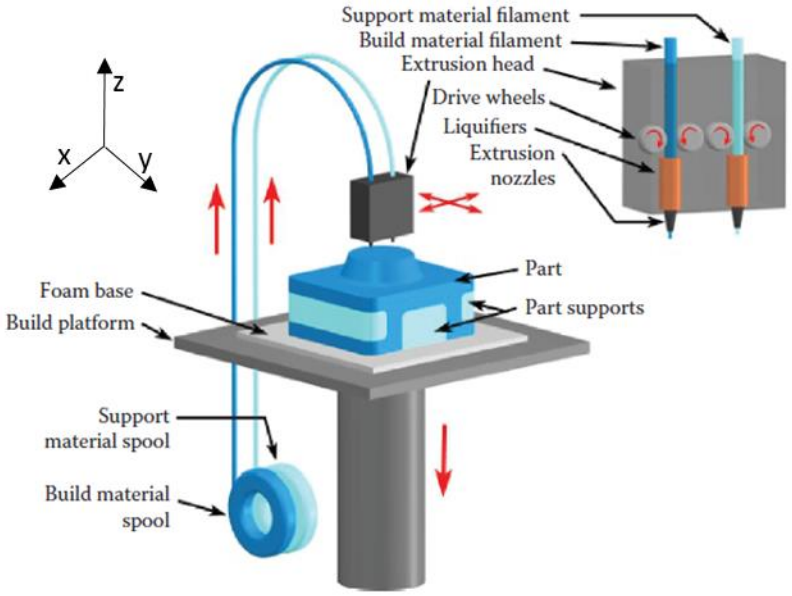

Figure 2.3 Schematic of the FDM fabrication process with dual printing head. Adapted with permission from [20]

2.2.1 Advantages and limitations

FDM technology is widely used for modelling, prototyping, customer-specific parts and fabrication of molds used for tooling thanks to its versatility [20]. Moreover, the expiration of Stratasys's patent in 2009 allowed the development of low-cost and open-source desktop printers, granting the companies to have an FDM system at a competitive price [12], [23].Therefore, FDM became a cost-effective technique able to fabricate complex shapes for which molds, tooling and chemical post-processing are not necessary [7], [9]. In addition, a wide variety of materials is available for this technology, since FDM is compatible with all thermoplastic polymers and their composite, as long as the heated nozzle can reach the processing temperature of the material and the filler content is not too high to make the composites too brittle and viscous [22]. FDM allows also the use of multiple nozzles on the same printing head, for the fabrication of multi-material parts during the same process. For example, build material and support material can be processed at the same time [7], [18].

One of the main limitations of the FDM technology is the difficulty in fabricating spanning structures. The extruded filaments needs to be supported by previously deposited material. Thus, the use of supports is often necessary, producing wastes and slowing down the printing time [7]. In addition, the support material is removed in a second step manually or through dissolution, if an appropriate solvent exists [24]. In general, to assure a good printing quality without using supports it is suggested to avoid cantilevers at an angle higher than 45° [12]. Moreover, the layer-by-layer process produces anisotropic parts, especially for composites due to the alignment of fillers along the printing direction [7], [12]. Moreover, the different layers are usually visible, affecting the surface quality of the fabricated parts. Compared to other AM technologies, FDM has a low resolution, around 40 µm, and the fabrication speed is low. Indeed, the fabrication of huge parts with a complex shape could take days. The complete or partial detachment of the part from the bed, i.e. warping, and delamination between printed layers are other problems that might occur during the fabrication. [7], [20], [23]. Another limitation in FDM technology is the high temperature required to process polymers with a high T_m or T_g, e.g., PEEK and PEI. Most FDM extruders are limited to a temperature of ~260°C, making the processing of the abovementioned materials practically impossible. Additionally, the presence of a heated chamber that can reach temperatures higher than 100°C is often required. Therefore, the development of high-temperature printing heads is necessary, increasing the cost of the machine. In addition, the high viscosity of the molted material and the addition of fillers may cause clogging of the nozzle during the fabrication process. The high temperatures required to allow the extrusion can also cause the degradation of the material [9], [22], [23].

2.2.2 Process parameters

FDM is governed by many processing parameters. The main parameters are related to the slicing of the geometry, the deposition of the material and the temperature settings necessary to achieve high printing quality.

Figure 2.4 shows two schematics representing the main processing parameters that are: layer thickness, build orientation, raster angle and width, air gap, contours number and width, temperature of the extruder, the bed and the chamber [20], [24].

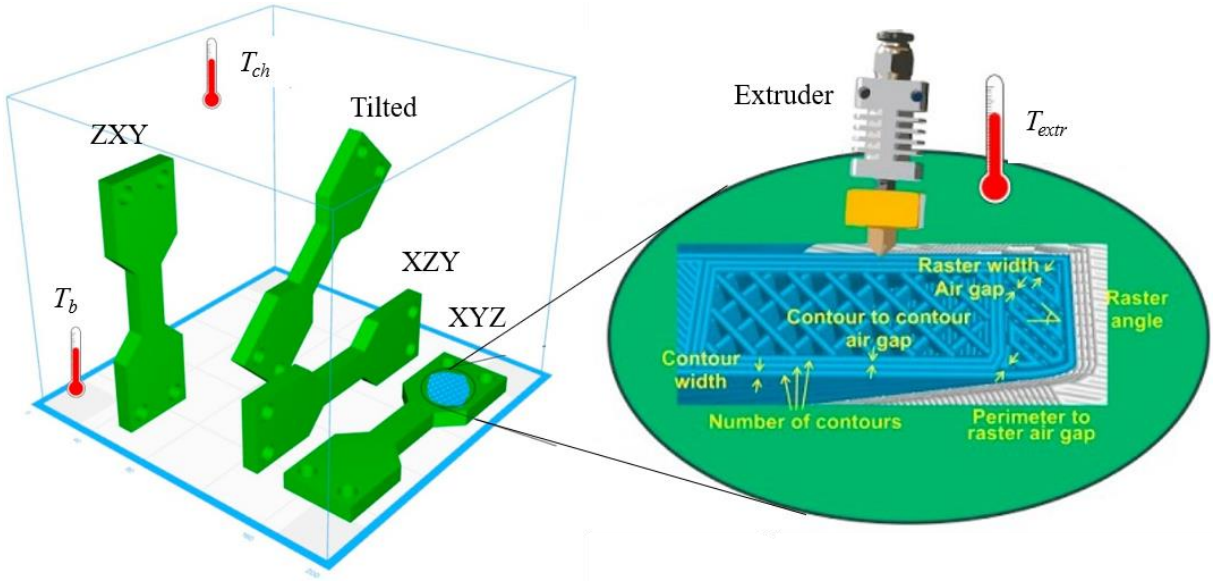

Figure 2.4 a) Schematic of some of the main processing parameters for FDM technology. Adapted with permission from [25]

One of the most important parameters is the layer thickness, which is the height of each deposited layer. Layer thickness usually range from 0.1 to 0.4 mm, depending on the size of the nozzle. The value of the layer thickness has a huge impact on the fabrication time and the surface finish. The use of a small layer thickness greatly increases the printing time, while a big layer thickness leads to a lower surface finish [20], [26].

Build orientation is the angle at which a part is oriented in the building platform with respect to *x*, *y* and *z*-axis [27]. A part can be tilted to achieve the best compromise between the fabrication time, the need of support material, the surface finish and the mechanical properties. Usually parts parallel to the building platform (i.e., XYZ and XZY configurations) have good surface finish and a lower printing time, while parts oriented perpendicularly to the building platform (i.e., ZXY configuration) have better surface finish as well, but the printing time is higher. Intermediate orientation angles causes a lower surface finish and usually requires more support materials [20], [26].

Raster or extrusion width refers to the width of the deposited material after being extruded from the nozzle. The raster width strictly depends on the nozzle diameter, being between 1.2 and 1.5 times larger, because of the swelling phenomenon that affects polymers after extrusion [28]. As

well as the layer thickness, lower raster width results in a better surface finish but a higher fabrication time. Regarding the mechanical properties, the extrusion width has little influence on them [24], [29]. Raster or infill angle, instead, refers to the angle at which the material is deposited after the extrusion with respect to the *x*-axis of the building platform. Therefore, the raster angle has an influence on the accuracy, surface finish and mechanical properties of the fabricated geometry. Parts fabricated at an infill angle of 0° and 90° show the best and worst mechanical properties, respectively [29].

Air gap is the distance between two adjacent rasters. There are three possible situations: air gap equal to zero (adjacent rasters touch each other), positive air gap (adjacent rasters do not touch) and negative air gap (adjacent rasters overlap). On one hand, positive air gaps between rasters causes porosity inside the part and, consequently, an infill percentage lower than 100%. Parts are lighter, allowing a faster and more cost-effective fabrication. On the other hand, zero and negative positive air gap minimize the porosity inside the material. For this reason, they are preferred for the fabrication of structural part. Moreover, negative air gaps contribute to the minimization of voids and improves bonding between adjacent rasters. However, it produces denser parts, increasing the weight, the fabrication time and the cost [26], [29], [30].

Contours or shells are the outermost and innermost perimeters of the geometry. Contours can be single or multiple and they seal the part in the case of infill percentage lower than 100%. Their number and width change the surface finish and the dimensional accuracy of the part. The use of contours is not a necessary feature [20], [26].

Temperature settings should be chosen depending on the material used for the fabrication. There are in general three types of temperature that can be set: the temperature of the extruder (T_{extr}), the temperature of the printing bed (T_b) and the temperature of the chamber (T_{ch}). T_{extr} should be set to allow the fusion of the material. T_{extr} is set above the T_m or the T_g to lower the viscosity of the molten material and facilitate the printing process. However, if the $\underline{T_{extr}}$ is too high, the viscosity of the extruded material is too low and it is not able to keep its shape after being deposited. On the contrary, if the temperature is too low, the material cannot flow properly, causing difficulties in bonding with the other deposited rasters [28]. It has been found that T_{extr} has little influence on mechanical properties, unless T_{extr} is too high leading to the degradation of the material [29]. T_b is set to help the adhesion of the first layer with the building platform and to avoid warping. For this

reason, the part should stay at a temperature close to its T_g. Moreover, the use of a heated bed improves also the interface adhesion between different adjacent layers [31]. T_{ch} allows a more even distribution of the temperature during the fabrication, helping to prevent delamination and warping. These beneficial effects are due to the better bonding that is created between deposited rasters in a heated environment, since the extruded filament stays at higher temperature for a longer period. If T_{ch} is not sufficiently high, the part may detach or deform during the fabrication process. If T_{ch} is too high, dimensional accuracy problems arises [28].

2.3 Materials for FDM

FDM technology is compatible with a wide variety of thermoplastic polymers and their composites. Figure 2.5 shows a pyramidal classification of plastics. Thermoplastic polymers can be classified based on their Continuous Use Temperature (CUT), mechanical performance and semi-crystalline or amorphous nature [32], [33]. Thermoplastic polymers are usually divided in four categories: commodity (CUT < 75°C), engineering (CUT < 140°C), specialty (140°C < CUT < 240°C) and extreme (CUT > 240°C) polymers.

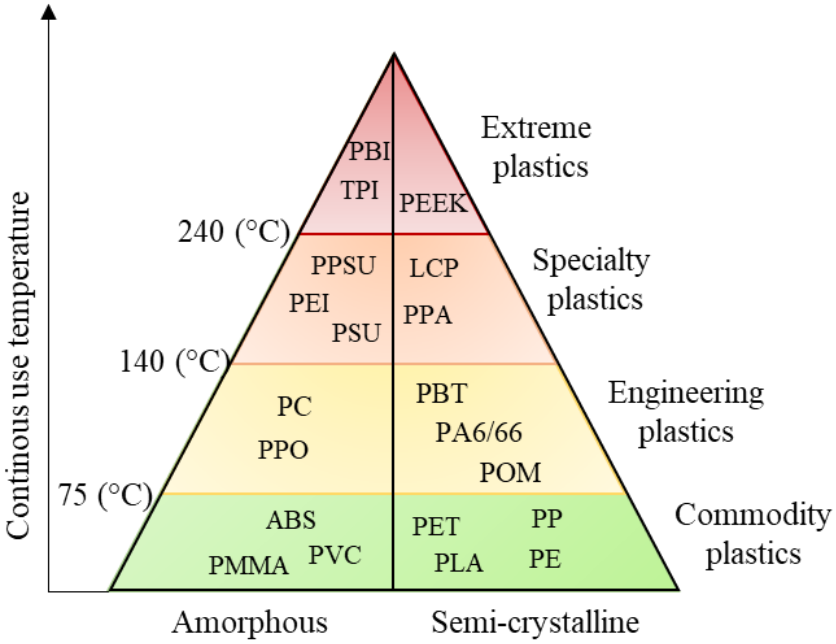

Figure 2.5 Classification of thermoplastic polymers based on their CUT.
Data are extracted from reference [32] and [34]

The most common materials used for FDM are Acrylonitrile Butadiene Styrene (ABS), PLA and PA, having a CUT of ~80°C, ~60°C and ~120°C. They are often used to obtain functional prototypes because of their relatively good mechanical properties and low processing temperatures. [20], [34]–[36]. However, for structural applications at high temperatures the material needs to maintain good mechanical properties. To achieve this goal, high temperature resistant thermoplastic polymers can be used. HTRTs are a type of polymers that has better properties than conventional plastics at elevated temperatures. More precisely, the following definitions can be used for HTRT.

> A more practical definition, and one that is gaining acceptance is a high performance/high temperature polymer retains usable properties at temperatures > 177°C after short-term and long-term exposure to one or more of the following conditions: flowing or static air; mechanical action; chemical action; electrical action; radiation (e.g. ultraviolet, electrons, protons, atomic oxygen, gamma rays, etc.); fluids (e.g. water, solvents of different types, etc.) (P. M. Hergenrother, 2003, pp.7-8)

In addition, they are characterized by a durability of 10000 h at 177°C, a degradation temperature higher than 450°C, a T_g or T_m higher than 200°C and high mechanical properties [34]

HTRTs include PEEK, PEI, polyetherketone, polysulfone, polyethersulfone. Table 2.1 reports some of the most used HTRTs with their characteristic temperature (T_g and T_m) and an example of commercial products available on the market. For the purpose of this literature review, only PEEK and PEI will be considered in this project, since they represent two of the most used HTRT polymers. Their characteristic, properties and typical processing temperature will be provided. Moreover, the works in the literature showing the FDM of these polymers will be reported.

Table 2.1 T_g, T_m and example of commercial products of the main HTRTs [34]

Name	**Commercial product**	**T_g (T_m), °C**
Bispenol A polysulfone	Udel™ P-1700	190
Polyethersulfone (PES)	Victrex™ PES 4800G	220
Bisphenol polysulfone	Radel™ R-5000	220
Polyether ketone (PEK)	Victrex™ PEK	162 (373)
Polyether ether ketone (PEEK)	Victrex™ PEEK 450G, Solvay™ Ketaspire KT-820	143 (334)
Polyetherimide (PEI)	Ultem 1010, Ultem 1000	217

2.3.1 Polyether ether ketone

PEEK is a semi-crystalline thermoplastic polymer, with a T_g of 143ºC and a T_m of 334ºC [34]. The molecular structure of the repeating units of PEEK is shown in Figure 2.6. The presence of the aromatic rings in the backbone of the polymer chains gives rigidity to the system. The rotation and folding of the chain is limited by the aromatic assembly [37]. In addition, the electron delocalization on the aromatic rings generates resonance stabilization, resulting in materials with high activation energy [38], [39]. Compared to amorphous materials, like PEI, it has the advantage of maintaining its mechanical properties above T_g. At temperatures below the T_g, the Young's Modulus of a polymer is relatively high due to the rigidity of crystalline and amorphous phases. After the T_g, a drop in the Young's modulus is observed and it is caused by the presence of the amorphous phase. The extent of the drop is related to the amorphous/crystalline ratio. Therefore, the presence of a crystalline phase allows the material to maintain mechanical properties after the T_g. The mechanical properties of the material at temperatures higher than the T_g are controlled by the crystalline phase [40]. In addition it has a better resistance to creep, wear and chemical attack [35], [41]. One additional advantage of PEEK is its biocompatibility, which makes it suitable for some biomedical applications. Other application fields could be aerospace and automotive

industry, considering the very good mechanical and chemical properties at high temperatures [42]–[44].

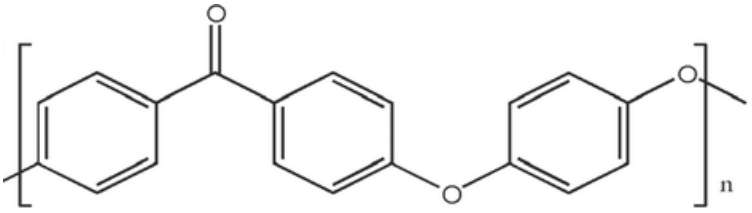

.

Figure 2.6 Molecular structure of PEEK repetitive unit. Adapted with permission from [45].

Several studied were performed on the effect of temperature settings (T_{extr}, T_b and T_{ch}) for FDM of PEEK [42], [46]–[48]. Xiaoyong *et al.* investigated the effect on using a heated printing bed and chamber during the FDM fabrication process [42]. They found out that the presence of both a heated bed and chamber significantly improved the mechanical properties of PEEK. The tensile strength was 71.2 MPa, while in the absence of a heated bed and chamber was only 46.2 MPa. The use of a heated bed and chamber produced a better adhesion between printed layers, leading to better mechanical properties.

The presence of warping deformation (i.e. the bending or twisting of a part, initially flat, caused by internal stresses or a rapid cooling) during the printing process is also highly influenced by the various temperature settings [49]. Figure 2.7 shows the effect of T_{extr} and T_{ch} on the warping deformation of additively manufactured PEEK samples. T_{ch} was varying from 90 to 130°C. Higher T_{ch} led to slower cooling and, consequently, less internal stresses. The warping deformation decreased with increasing the T_{ch}, with a maximum of 1.93 mm at 90°C and 0.65 mm at 130°C. Regarding the T_{extr}, it was varied from 340 to 360°C. In this case, the warping deformation shows a minimum, with a value of 0.65 mm, at 350°C. T_{ch} has a greater influence on the warping deformation than T_{extr} [46].

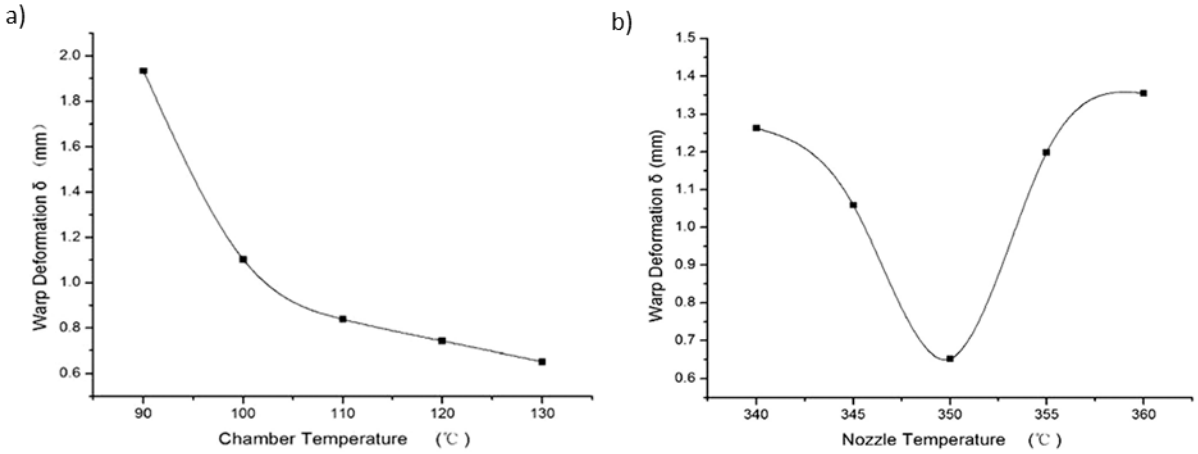

Figure 2.7 Influence of a) T_{ch} and b) T_{extr} on warp deformation.
Adapted with permission from [46]

Studies were also conducted on the influence of layer thickness and raster angle during the printing process [43], [44], [47]. Wu *et al.* investigated the effect on the mechanical properties of three different layer thickness (i.e., 200, 300 and 400 μm) and three different raster angle stacking sequences (i.e., 0°/90°, 30°/-60° and 45°/-45°) with the aid of tensile, bending and compression tests [43]. The highest tensile, bending and compressive strengths were obtained for a layer thickness of 300 μm and raster angle of 0°/90°. The layer thickness of 400 μm led to the worst mechanical properties, while no significant difference was found for the 30°/-60° and 45°/-45° stacking sequences. Rahman *et al.* studied the effect of different raster angles on tensile, compressive, bending and impact properties [44]. Similarly to the abovementioned study, sample fabricated at 0° showed the best mechanical properties. Regarding the impact test, the absorbed energy for samples oriented at 0° was one order of magnitude higher than the ones oriented at 90°. Contrary to what was observed regarding the layer thickness, Wang *et al.* showed that a layer thickness of 100 μm had a beneficial effect on the mechanical properties [47]. A higher layer thickness, on the contrary, promotes stratification of additively manufactured parts.

2.3.2 Polyetherimide

PEI is an amorphous polymer with a T_g of 217ºC [50]. Figure 2.8 shows its chemical structure. As PEEK, aromatic rings are present in the molecular chain giving rigidity to the system, resonance stabilization and high activation energy [38], [39]. PEI has high mechanical properties, high

temperature stability, flame resistance, good electrical properties and good chemical stability [51]. The main drawback of PEI is its high level of hygroscopicity, i.e. the tendency of absorbing moisture from the environment, making the storage in an oven and a control of the moisture content during the fabrication necessary [52]. PEI is used in the aerospace, automotive and medical fields [53], [54].

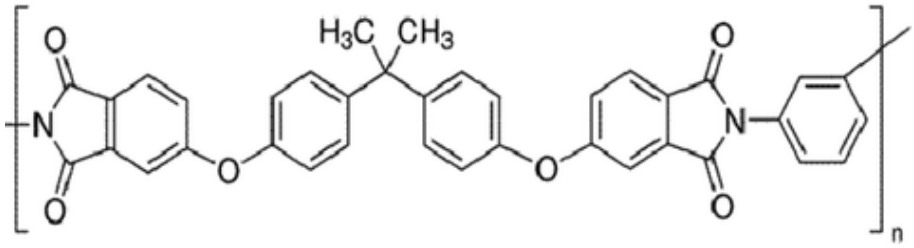

Figure 2.8 Molecular structure of PEI repetitive unit. Adapted with permission from [45].

Previous works related to the evaluation of the mechanical properties of FDM additively manufactured PEI specimens are present [55]–[58]. Spikowski *et al.* studied the effect of the build orientation on the mechanical properties of PEI [55]. They fabricated PEI tensile test specimens, i.e. dogbones, parallel (XYZ and XZY configurations) and perpendicular (ZXY configuration) to the building platform. In addition, the effect of a negative air gap was evaluated. XYZ and XZY dogbobes showed a higher tensile strength. While, the use of a negative air gap (denser part) caused an increase of both Young's modulus and tensile strength. Additively manufactured parts were also compared to injection molded parts. Young's modulus and tensile strength of the FDM specimens were 75% and 87% of the one of the injected molded part, respectively.

Taylor *et al.* evaluated the fracture toughness of Ultem 1010 PEI samples fabricated with three different building orientations and four raster angles [56]. Figure 2.9 shows the results of the mechanical tests. The specimens printed along the *z*-direction had a decrease in the critical stress intensity factor, due to the layer oriented in the same direction of the crack propagation. For layers oriented perpendicular to the propagation of the crack, the raster angle that provided the highest toughness was 0°. The effect of build orientation and raster angle on flexural strength was also evaluated. XYZ, XZY and ZXY configurations with raster angle stacking sequences of 45°/-45° and 0°/90° were tested. The ZXY build orientation had the lowest value of yield strength, with no

influence of the raster angle, while the XZY orientation had the highest value. Moreover, the stacking sequence 45°/-45° provided better results than the 0°/90°, with a yield strength of ~115 MPa compared to ~100 MPa of the 0°/90° configuration [57].

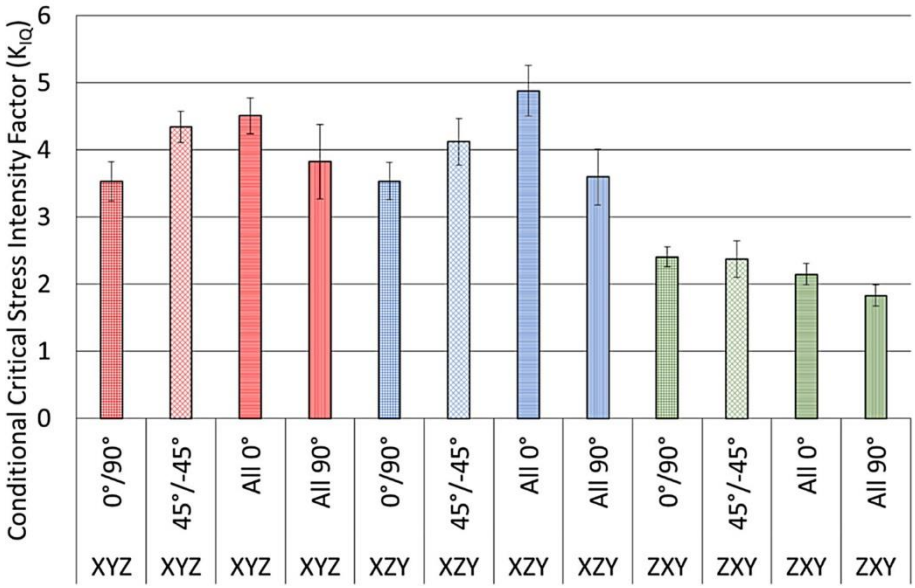

Figure 2.9 Effect of the variation of building orientation and raster angle on the conditional critical stress intensity factor of FDM PEI specimens. Adapted with permission from [56]

Mechanical properties of AM PEI parts under traction were investigated by Bagsik and Scöppner [58]. Dogbones were printed with different build directions and air gaps. The ZXY configuration showed the worst properties for the strength and the strain at break, due to the printed layers oriented perpendicularly to the loading direction. In addition, the use of a negative air gap helped to improve mechanical properties.

Some studies were carried out to evaluate the effect of the moisture content inside PEI filaments [52]. Chuang *et al.* studied the moisture content of two different type of PEI commercial filaments: Ultem 9085 and Ultem 1000 [52]. Ultem 9085 showed a porosity of 5-8% after the printing process, while the porosity was 25% for Ultem 1000. The difference is explained by the higher viscosity of Ultem 1000 that is three times the one of Ultem 9085. Therefore during the printing process, T_{extr} had to be raised from 375°C (used for Ultem 9085) to 420°C to allow the extrusion of the filament. The authors also linked the increase in void content to the expansion of a slight amount of degradation gases. To reduce the amount of porosity, the storage in an oven at a temperature higher

than 150°C for at least 12h is suggested. Alternatively, a feeding system for FDM machine was designed to avoid contact with the atmosphere. The filament spool is stored in a box containing a desiccant to control the level of humidity. Polytetrafluoroethylene tubes were used to connect the box to the FDM printing head, avoiding exposure to the atmosphere [59].

The mechanical performance of additively manufactured PEI at high temperature were also investigated. Figure 2.10 shows the results of a 3-point bending test performed on FDM specimens tested at different temperatures (25°C, 80°C, 120°C, 150°C, 177°C and 205°C). The flexural modulus exhibited a drop of ~400 MPa at 205°C with respect to the value exhibited at room temperature. Instead, the yield strength exhibited a drop of ~10 MPa at 150°C with respect to the value obtained at room temperature. [57].

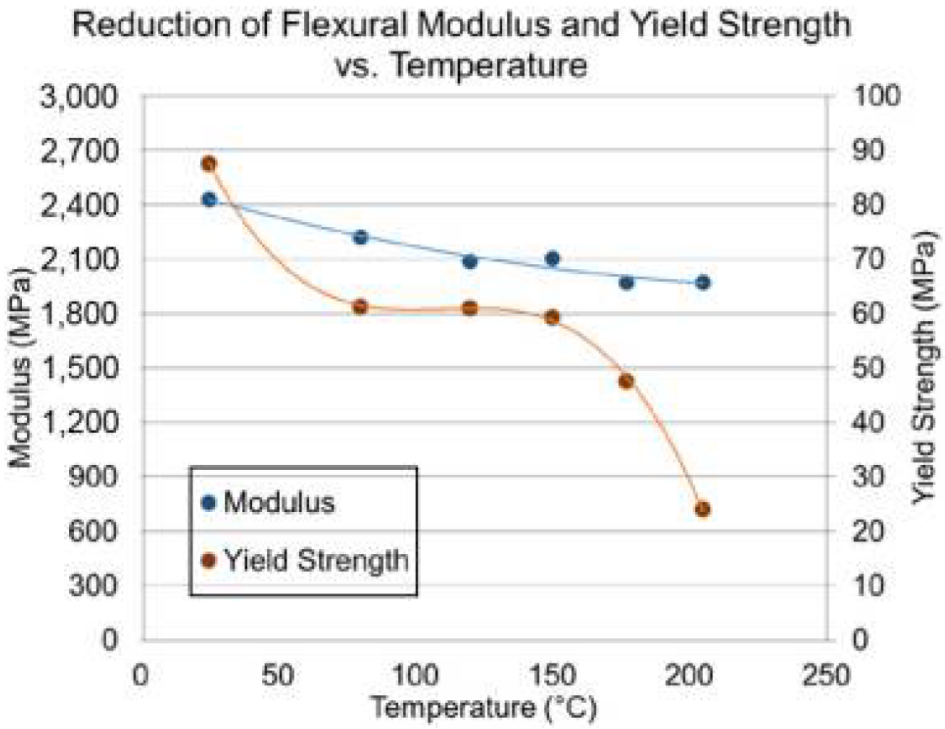

Figure 2.10 Effect of the environmental temperature on FDM PEI samples tested under a 3-point bending test. Adapted with permission from reference [57]

2.3.3 PEEK/PEI blends

Polymer blending refers to the mixing of two or more different polymers to obtain a new one. With polymer blending, it is possible to tailor the material properties, combining the benefits of two or more different polymers while limiting their negative features. Polymer blends can be miscible, partially miscible and immiscible. Miscible blends contain one homogenous phase and behave like a single polymer. When the polymers are miscible only in a specific composition range, the blend is considered partially miscible. Finally, immiscible blends are heterogeneous and contains two distinct phases. The presence of a single T_g is the main criterion to establish miscibility because it means that the two materials are mixed at the molecular level [60]. For miscible polymers, T_g of the blend is directly related to the weight fraction and to the T_g of the constituent of the blend, following the Fox equation (Equation 1):

$$\frac{1}{T_g} = \frac{w_1}{T_{g1}} + \frac{w_2}{T_{g2}} \tag{1}$$

where T_g is the glass transition of the blend, T_{g1} and T_{g2} are the glass transition temperatures of the constituents of the blend and w_1 and w_2 are the weigh fraction of the constituent of the blend [60]–[62].

PEEK and PEI can be mixed to obtain miscible polymer blends due to their similar chemical structure. Moreover, the two polymers have similar processing temperatures, allowing an efficient mixing without material degradation. Their miscibility is proven by the presence of a single T_g for all the PEEK/PEI compositions. [61], [63]. The main advantage of mixing PEEK and PEI is the increase of the T_g of the material. PEEK has a T_g of ~145°C and close to this temperature its modulus decreases drastically [61], [64]. The addition of PEI increases the T_g following the Fox equation (Equation 1), making the material capable of operating at higher temperatures. Table 2.2 reports the T_g and T_m of different PEEK/PEI blends. T_g and T_m were measured using Differential Scanning Calorimetry (DSC). DSC is a thermal analysis technique that measures the change in the heat capacity (C_p) with a change in the temperature. A sample having a known mass is heated or cooled and the changes in the C_p are monitored as changes in the heat flow. Therefore, DSC curves are usually represeted as heat flow vs. temperature. DSC can be used to detect transitions such as melting and glass transition temperatures and curing state. T_g is a second order transition, therefore

it is necessary to compute the derivative of the heat flow with respect to time and the T_g is located at its maximum. The melting is an endothermic transition (i.e. a transition that requires a heat supply to happen) and it generates on the DSC curve an endothermic peak. The maximum of the endothermic peak is usually the T_m. [65]. The blending mechanism of PEEK and PEI led to a reduction of the T_m when the concentration of PEI in the system is increased. During the crystallization of the blend, PEI is rejected into the amorphous domain of PEEK, causing a change in the amorphous composition of PEEK. Thus, a reduction in the chains mobility occurs, causing the reduction of the T_m [61], [63], [66]. The phenomenon is even more evident when the PEI content is relatively high, e.g., PEEK/PEI 70wt.%/30wt.% blend.

Table 2.2 Characteristic temperatures (T_g and T_m) of neat PEEK/PEI blends with different composition [61]

PEEK/PEI (wt.%/wt.%)	**T_g (°C)**	**T_m (°C)**
100/0	155	341
90/10	164	339
80/20	168	339
70/30	172	338
50/50	188	332
30/70	200	332
0/100	220	N/A

2.3.4 PEEK, PEI and PEEK/PEI blends with the addition of fillers

Addition of fillers such as short CFs [67]–[73], carbon nanotubes (CNTs) [74]–[78], graphene [50], [79], alumina [80], nano titanium dioxide [45], gadolinium [81], hydroxyapatite [82]–[85], etc. to PEEK and PEI has significantly improved their tribological and thermal behaviours. The lightweight and the strength of the short CFs make them a versatile filler for a variety of applications. Contrary to CNTs, CF price is lower and their straight structure avoids interlocking,

which is very common in CNTs. Interlocking may result in the formation of agglomerates that will cause a reduction of the mechanical properties. [86]. Kumar *et al*. [73] showed that in dynamical mechanical testing, the storage modulus and the glass transition temperature are increased when CFs are added to PEI. However, they found that treatment of CFs with a mixture of sulfuric acid and nitric acid, allowed a better dispersion of the CFs in the matrix and improved their adhesion with PEI, resulting in a further enhancement of the storage modulus and the T_g.

The addition of carbon nanofibers (CNFs) to PEEK showed also that the tensile strength and stiffness improve with increasing the CNFs content up to 15wt.%. When the CNFs concentration was higher than 10wt.%, the material began to show a brittle behavior. The T_g was not affected by the addition of CNFs [68].

Researchers have studied the addition of fillers to PEEK/PEI blends. Dìez-Pascual and Dìez-Vincent studied the addition on nano-TiO_2 to the blend [45]. They selected the blend PEEK/PEI (70wt.%/30wt.%) as the composition that mostly optimizes PEEK and PEI benefits. The addition of nano-TiO_2 provided an increase in the Young's modulus and tensile strength of 41% and 19% without affecting the biocompatibility of the polymer matrix, respectively.

Regarding the FDM of PEEK and PEI composites, very few works are present in the literature. PEEK/CNT and PEEK/CNT/Graphite nanoplates (GnP) composites were successfully printed by FDM [74], [87]. Figure 2.11a shows that the addition of CNT up to 5wt.% did not influence the Ultimate Tensile Strength (UTS) of neat PEEK [74]. Figure 2.11b highlights that the addition of GnP to the PEEK/CNT composites provided an increase in the Young's modulus, with the PEEK/CNT 3wt.%/GnP 3wt.% composition that reached ~3.75 GPa, leading to an improvement of ~25% with respect to neat PEEK. However, the elongation at break was reduced. PEEK/CNT/GnP showed also improved electrical and thermal conductivity [87].

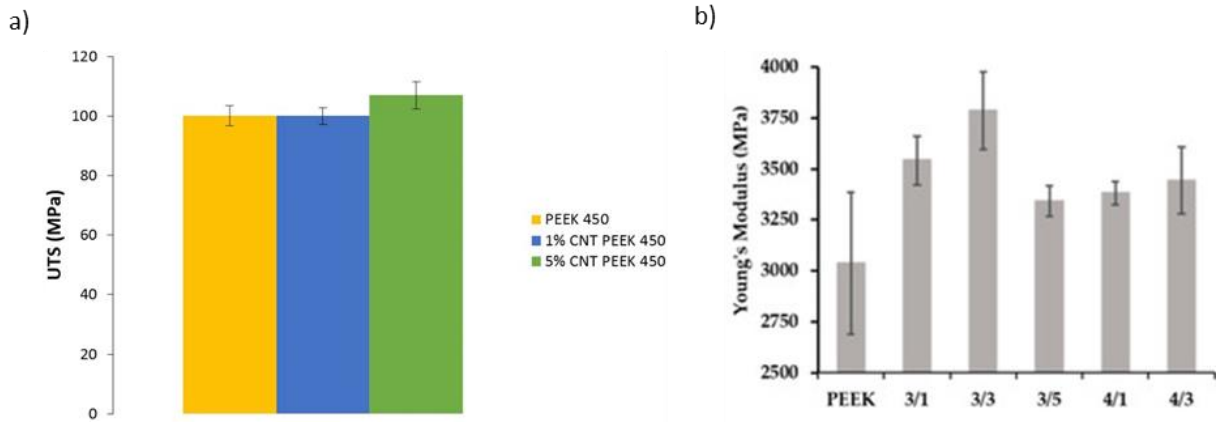

Figure 2.11 a) UTS of FDM PEEK/CNT composites. b) Young's modulus of FDM PEEK/CNT/GnP composites. Composites are named according to the ratio CNT/GnP. Adapted with permission from [74], [87]

Stepashkin *et al.* successfully fabricated a PEEK/CF 20wt.% filament suitable for FDM AM using a single-screw extruder with a processing temperature of 400°C [88]. Then, the composite filament was additively manufactured using a T_{extr} of 380°C, a T_b of 95°C and a layer height of 0.25 mm. Figure 2.12 shows Scanning Electron Microscopy (SEM) images of the fracture surface of the fabricated composites. The presence of a large amount of defects, probably caused by an improper choice of the printing parameters, negatively affects the printing quality. Discontinuities are present at the interface between printed layers, as well as defects and voids inside the polymer matrix. These defects make the FDM parts less dense that the ones produced by casting.

Chuang *et al*. fabricated by FDM PEI/CF composites [52]. The studied materials were Ultem 9085 and Ultem 1000 with 10wt.% of short CFs. They evaluated the moisture content of the filament and evaluated their mechanical properties. Figure 2.13 displays optical micrographs of the cross section of the as-received, dried, and FDM-extruded filaments. The extrusion through the FDM nozzles caused an increase of the porosity due to the expansion of moisture during the printing process. Drying the filament before the FDM extrusion helped to reduce the moisture content and, consequently, the void content. Regarding the mechanical properties, Ultem 1000 increased the Young's modulus by 38%, the tensile strength, by 23% and reduce the strain-to-failure by 55% after the addition of CFs. It was shown that drying the filaments to reduce the amount of moisture had a beneficial effect on the mechanical properties.

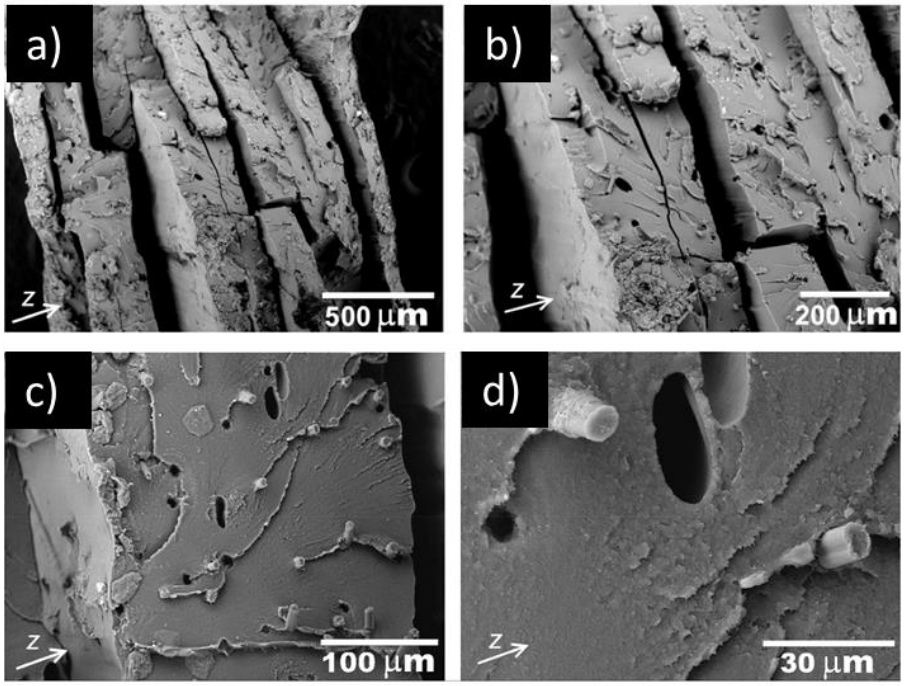

Figure 2.12 SEM images of the fracture surface of PEEK/CF FDM specimens. It is possible to highlight the presence of voids between different layers (a,b) and flaws inside the polymer matrix (c,d). Adapted with permission from [88]

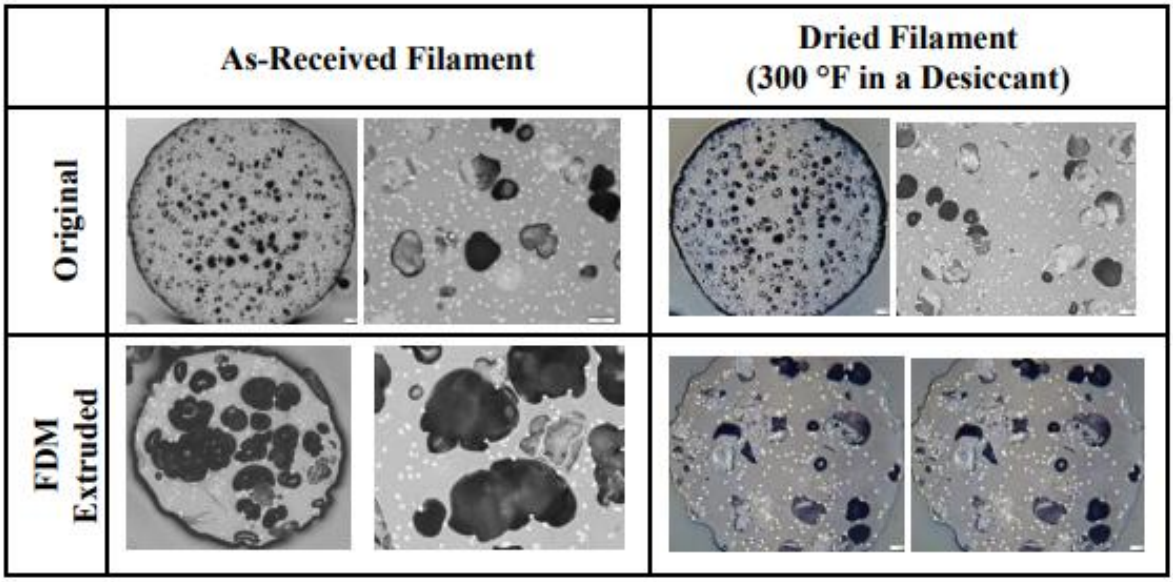

Figure 2.13 Optical micrograph of the cross section of PEI/CF 10wt.% as-received, dried and FDM-extruded filaments. This figure is taken from [52] and used with permission of NASA

In brief, several works are present in the literature reporting the FDM of neat HTRT polymers. Studies on their printing parameters, i.e., T_{extr}, T_b, T_{ch}, layer thickness, raster angles and building orientation were carried out to maximize the printing quality and the mechanical properties of the printed parts, avoiding fabrication defects (e.g., warping and delamination). Concerning FDM of PEEK and PEI reinforced with fillers, very few works investigated the mechanical properties of such materials. Table 2.3 shows the summary of the works regarding the FDM of PEEK and PEI composites reported in this literature review. The difficulties in printing HTRT composites were highlighted since printing defects like delamination, discontinuities and voids in the polymer matrix were often present in the printed samples

Table 2.3 Summary of the reported works regarding the FDM of reinforced HTRT composites

HTRT polymer	**Filler**	**Printing temperature**	**Main conclusions**	**Reference**
PEEK	CNT	T_{extr} = 365 °C	No significant effect of CNT on UTS	[74]
	CNT/GnP	T_{extr} = 400°C	Increase in the *E* of ~25%	[87]
	Short CF	T_{extr} = 380 °C	Discontinuities between layers Voids and defects inside the polymer matrix	[88]
PEI	Short CF	T_{extr} = 420 °C	FDM causes an increase of porosity *E* increased by 38%, tensile strength increased by 23%, elongation at break reduced by 55%	[52]

2.4 FDM in the aerospace field

FDM is used in the aerospace industry for the fabrication of layup tools, which are normally fabricated with Computer Numerical Control (CNC) tooling. FDM helps to reduce the fabrication time leading also to a significant reduction of the cost of the part [6], [89], [90]. Other manufacturing tools such as molds, templates, jigs, fixtures and surrogates can be fabricated by FDM. FDM is used also for the fabrication of end-use parts, i.e., parts that are ready to be sold to costumers [91]. The majority of them are represented by interior parts made of Ultem 9085, which

is a material meeting the Federal Aviation Administration (FAA) regulations of flame retardancy, smoke and toxcity [90]. Regarding the fabrication of functional part, the use of FDM is under development. For example, NASA fabricated a composite vane made of PEI/CF [52], [92]. NASA also fabricated parts made of PEI for sound attenuation such as perforated access panels and acoustic sandwich panels, i.e. acoustic liners. Acoustic and sandwich structures will be covered in detail in Section 2.4.1 and Section 2.4.2.

2.4.1 Acoustic application for aerospace structures

AM represents an interesting fabrication technology for acoustic application due to the easiness in obtaining complex shapes starting from a CAD file. Different type of acoustic structures can be fabricated, an example is represented by Helmholtz resonators, which are a passive system for noise attenuation. Figure 2.14a represents a Helmholtz resonator. It consists of a cavity (with a volume V_c) connected to the surrounding environment by a neck (with a diameter D_n and a length L_n). The sound absorption mechanism of Helmholtz resonators can be explained with the aid of an analogous mechanical system, represented by a spring-mass-damper system, as shown in Figure 2.14b. The volume of air contained in the neck can represented by a mass, while the volume of air inside the cavity can be represented by a spring. During oscillations, the air contained in the volume of the cavity (the spring) is alternately compressed and expanded. The sound entering into the neck is dissipated by friction against the walls of the neck during the oscillation [93]–[99]. The sound absorption happens at the natural frequency of the resonator, since the oscillation is highly amplified by the resonance. The natural frequency of the resonating chamber depends on the geometric parameters of the resonator, i.e. D_n, L_n and V_c, as shown in Equation 2 [94], [96]:

$$f_r = \frac{c}{2\pi}\sqrt{\frac{\pi D_n^2/4}{V_c L_n}} \tag{2}$$

where f_r is the resonant frequency of the resonator and c is the speed of sound in the medium of interest. Usually, Helmholtz resonators are used for sound dissipation at low frequency (e.g., < 1000 Hz). Another important parameter for the Helmholtz resonator is the length of the cavity.

There are two possible situations depending on the ratio between cavity length and neck diameter. When the cavity length is bigger that the neck diameter (i.e., ratio > 1) there is a purely axial propagation of the soundwave. Instead, when the cavity length is smaller than the neck diameter (i.e., 0.1 < ratio < 1), there is a radial propagation of the soundwave [100]. Dickey and Selamet reported that the major effect of wave motion is the change of the location of the resonance frequency. Cavity length smaller than the neck diameter causes a reduction in the resonance frequency [101].

The main drawback is the narrow band of absorbed frequency. To overcome this limitation, it is possible to tune multiple Helmholtz resonators to broaden the absorbed frequency range. Dual Helmholtz resonator, in which two necks or two cavities are connected in series, characterized by the presence of two absorption peaks, have been developed. The dual resonator was formed by connecting a cavity to the end of a Helmholtz resonator. To create the additional absorption peak, a hole was opened between the two cavities [102], [103]. Zhao and Morgans studied a system featuring multiple Helmholtz resonators tuned by changing the area of the necks. The developed structure was created to damp unstable combustion system [104]. Instead, Wang and Huang studied the acoustic properties of a parallel arrangement of micro-perforated panels (MPPs) featuring different cavity depths. The physical explanation regarding the sound absorption was investigated. It was found that the parallel absorption mechanism is influenced by the geometry of the MPP absorber array. The absorption of the MPP absorber array changes using different widths and spatial arrangement of the cavities. Additionally, slight improvements occurred at certain off resonance frequencies [105].

Only a few works have reported acoustic structures produced by AM so far. Figure 2.15 shows some structures fabricated with an AM process. Perforated panels [106] and porous polycarbonate material [107] were produced by stereolitography (SLA) (Figure 2.15a). Taking advantage of AM versatility, they were able to test different perforation ratios and perforation angles to find the best acoustic absorption behavior. Setaki *et al.* [108] studied different absorbers based on the passive destructive interference principle (Figure 2.15b). They produced thirty-one different geometries through Selective Laser Sintering (SLS), for complex internal air paths [108], [109]. Fotsing *et al.* [110] implied direct ink writing for the fabrication of an array of micro-rods (Figure 2.15c). The structures were characterized by a broadband sound absorption starting from 2500-3000 Hz.

Finally, Cai *et al.* reported the fabrication through AM of ultrathin sound absorbing panels featuring a coplanar spiral tube (Figure 2.15d) [111]. The structures had an absorption peak at low frequencies (250 – 400 Hz) depending on the geometrical parameters of the panel.

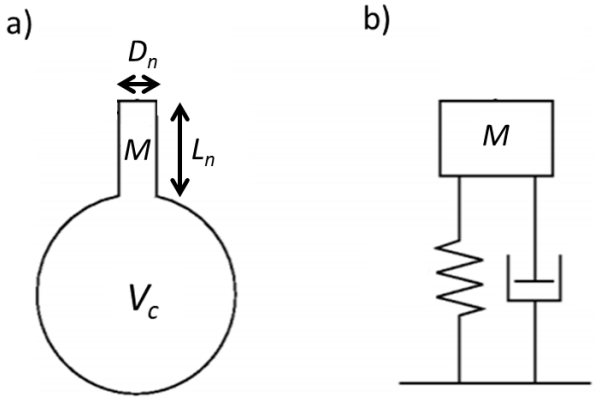

Figure 2.14 a) Schematic representing a cylindrical Helmholtz resonator. b) Spring-mass-damper system representing the mechanical analogy with Helmholtz resonators. Adapted with permission from [96]

Zhang and Hu developed and fabricated with FDM an acoustic metasurface made of PLA featuring a labyrinth-like shape [112]. The structures were able to absorb sound at low frequencies, in the range of 100-200 Hz. Also Liu *et al.* fabricated a multi-unit metasurface [113]. Figure 2.16 shows the additively manufactured sample and its absorption coefficient (α) curve. The sample exhibited almost perfect absorption between 450 and 1360 Hz. This result was achieved by the creation of a multi-order absorption mechanism separating single Helmholtz resonator chambers by mean of a plate with a small perforation, placed on the lateral wall of the resonator. This particular type of Helmholtz resonator was called Perforated Composite Helmholtz Resonator (PCHR). A single PCHR produced two absorption peaks, the first being generated by the traditional Helmholtz resonator while the second by the addition of the perforated plate, thus increasing the range of absorbed frequencies. The overall metasurface featured four PCHRs, generating eight absorption peaks, and four traditional Helmholtz resonators, generating four absorption peaks. Therefore, the metasurface was characterized by a total of twelve absorption peaks.

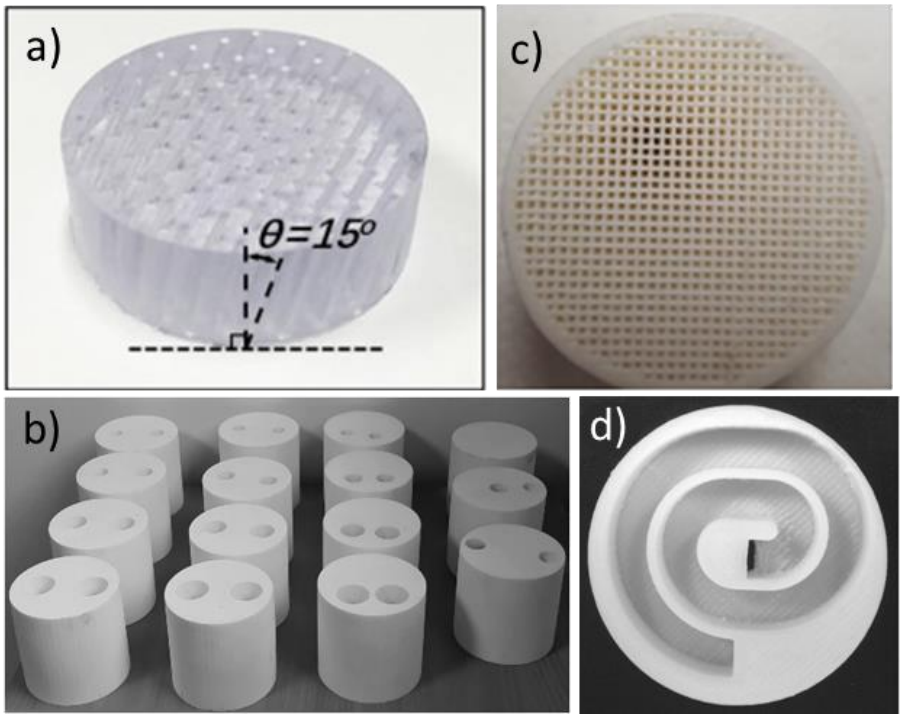

Figure 2.15 Different type of acoustic structures obtained by AM: a) Porous polycarbonate material, b) Passive destructive interference principle devices, c) Array of micro-rods, d) Absorbing panel featuring a coplanar spiral tube. Adapted with permission from [107], [109], [110] and [111]

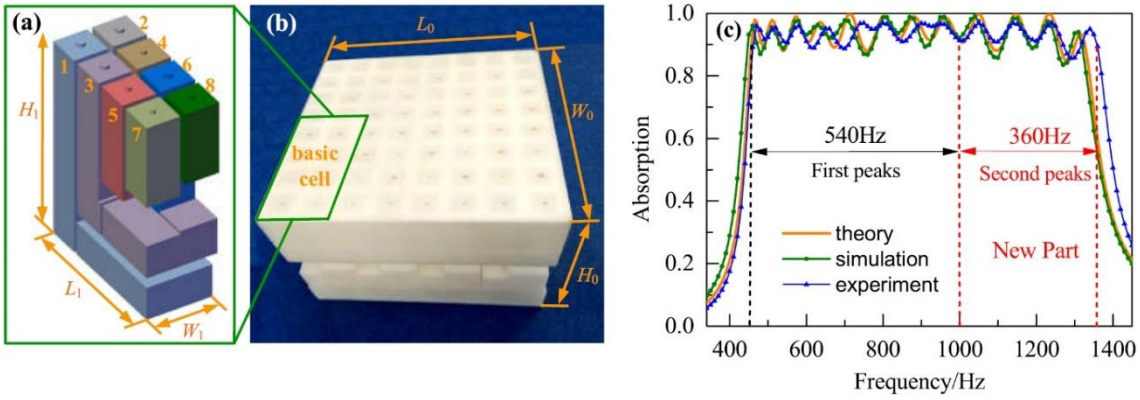

Figure 2.16 a) Schematic of the multi-unit metasurface cell. Unit 1 to 4 are PCHRs, while unit 5 to 8 are Helmholtz resonators. b) Additively manufactured sample of the multi-unit metasurface. c) Sound absorption results of the multi-unit metasurface. The first peaks refer to the absorption peaks generated by the Helmholtz resonators, while second peaks refer to the additional peak generated by the PCHRs. Adapted with permission from [113]

2.4.2 Sandwich panels

Sandwich panels can provide low density, thermal insulation, acoustic damping, etc. [114]. Acoustic liners represent a particular type of sandwich panel and they are classified based on the number of honeycomb cell layers, i.e., Single Degree Of Freedom (SDOF) have one honeycomb cell layer while Double Degree Of Freedom (DDOF) have two honeycomb cell layers. Figure 2.17 shows a schematic of SDOF and DDOF acoustic liners. SDOF consists of a solid backplate, a honeycomb core and a perforated facesheet (Figure 2.17a). The solid backplate and the perforated facesheet are much thinner than the core and they are made of a stiffer material, while the core is lighter and more compliant. The facesheets (or skins) carry the bending and in-plane loads, while the core guarantees the integrity of the structure by transferring loads between the facesheets and resisting to the transverse shear [115]. DDOF presents a double honeycomb core, separated by an additional porous facesheet (Figure 2.17b). The use of two honeycomb cell layer creates two different resonant cavities connected in series, thus creating two absorption peaks. However, the weight and thickness of the panels are increased [116].

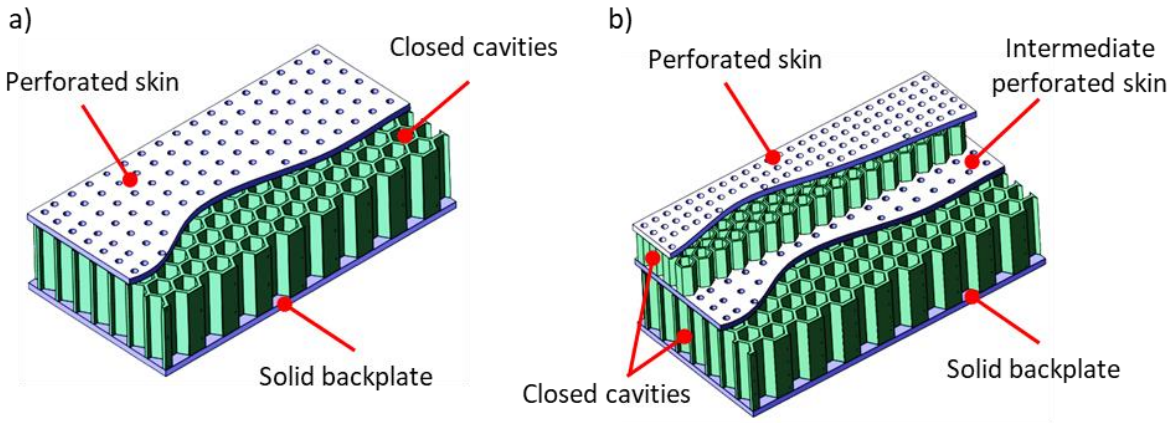

Figure 2.17) SDOF acoustic liner. b) 2DOF acoustic liner. The presence of a perforated skins, closed cavities and solid backplates is highlighted

Micro-Perforated Panels (MPPs) represent a type of acoustic liner that has the perforated facesheet featuring multiple sub-millimeter perforations. The advantage of this technology is the possibility to achieve sound absorption in a broader range of frequencies starting from mid-frequencies. However, absorption at low frequencies is more difficult to obtain for MPPs and, therefore, they do not represent the most suitable choice when low-frequency absorption is aimed [117]–[120].

Some researchers combined MPPs with a core that presented perforations itself to enhance acoustic performances [121], [122]. Yang *et al.* designed a type of core that was a combination of a traditional honeycomb core and of a corrugated core, calling it honeycomb-corrugation hybrid core. Heterogeneous perforations were also present on the core, in addition to the perforations already present on the top facesheet [121]. Their simulations showed an average absorption coefficient of 0.75 over the frequency range between 500 and 1000 Hz. Meng *et al.* 3D printed with FDM and tested corrugated sandwich panel acoustic samples with a diameter of 100 mm, showing the feasibility of fabricating perforated sandwich structures with a corrugated core [122]. However, they just fabricated a sample of reduced dimensions (i.e., a cylindrical sample with a diameter of 100 mm) suitable for the acoustic characterization. Moreover, the effect of the addition of perforations on the corrugation of sandwich panels was investigated, claiming that perforations in the corrugation helped to improve the acoustic performance of the structure.

Lin *et al.* developed a continuous degree of freedom core for acoustic liners, in which a plurality of resonant cells were present [123]. They obtained a broadband sound absorption from ~1000 to ~2700 Hz with an absorption coefficient always greater than 80%. Similarly, Peng *et al.*developed a sandwich panel with nine resonant cells featuring broadband sound absorption [124]. Figure 2.18 shows the disposition of the resonant cells, their features and their absorption coefficient. Each cell is a Helmholtz resonator and posses a perforation, a neck (the top facesheet) and a cavity (a single honeycomb cell). Simulations showed that tuning the diameter of the perforations it was possible to obtain an almost perfect absorption in the range of frequencies 600–1000 Hz.

A drawback of sandwich panels is that they usually require several manufacturing steps, e.g. facesheets fabrication, core fabrication and bonding the facesheets to the core [114], [125]. Moreover, core geometries are limited by conventional fabrication techniques such as extrusion, expansion, milling and corrugation [126]–[128]. Therefore, AM is an interesting alternative with the ability to address the aforementioned fabrication issues.

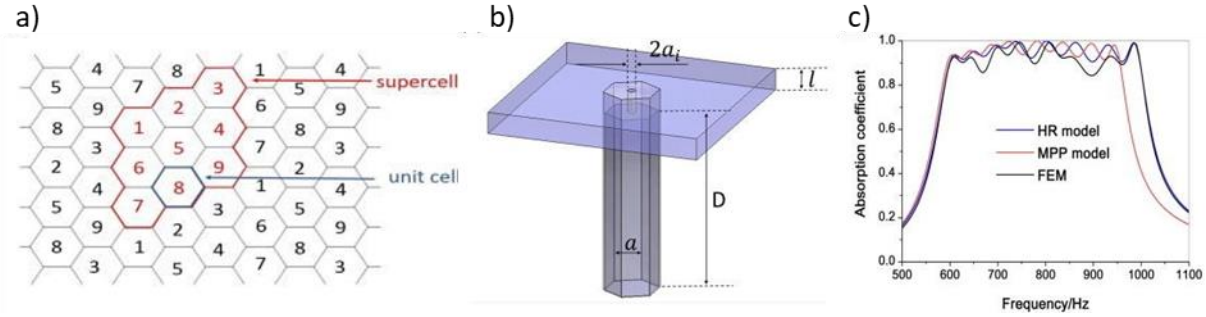

Figure 2.18 a) Representation of the arrangement of the nine unit cells. b) Constituting element of each unit cell: perforation, top facesheet and honeycomb cavity. c) Results of the sound absorption behaviour provided by analytical and finite element models.
Adapted with permission from [124]

Some works on the AM of sandwich panels are present in the literature, even though the acoustic application is not reported. Sarverstani *et al.* fabricated sandwich panels for energy absorption made of PLA [127], [128]. Figure 2.19 shows the fabricated sandwich panels featuring three different core geometries, i.e, rectangular, hexagonal and auxetic. Moreover, the flexural stiffness, the quasi-static and the dynamic energy absorption of the panels were investigated. The feasibility of using FDM to fabricate single-material sandwich panels in one-step was also provided. Bagsik *et al.* fabricated sandwich structures made of PEI in one-step with an FDM process [129]. The effect of the structure width, wall thickness, top facesheet thickness and geometry (i.e., honeycomb, tube and rectangle) and building orientation (i.e., XYZ and ZXY) of the core was investigated. It was shown that core oriented longitudinally (perpendicular to the application of the force) showed an improvement in the flexural stiffness by ~165% and in the maximum loading force by 50%. Core oriented longitudinally had the interfaces between printed layers oriented in a more favorable direction, leading to an improvement of the mechanical properties. In addition, it was determined that the top layer thickness had the greatest influence on the strength among the other studied parameters. Some studies are also present on the production by AM of the core of sandwich panels [130], [131]. In these cases, the core is then bonded to the facesheet with a separated process. It was claimed that cores produced by FDM had higher compressive strength and lower specific strength than conventional Nomex cores [130].

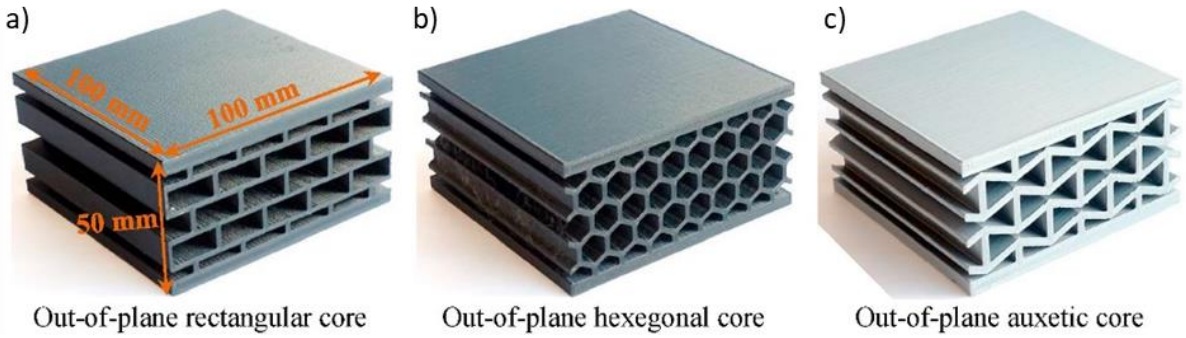

Figure 2.19 Sandwich panels fabricated by FDM featuring rectangular (a), hexagonal (b) and auxetic (c) core geometries. Adapted with permission from [127]

In conclusion, sandwich panel for sound absorption have been investigate in the literature. Studies were carried out to developed sandwich panel with an improved sound absorption behavior. However, most of these works concern analytical or numerical simulation without providing experimental validation of their models. Additionally, the acoustic characterization is usually performed on sample of reduced dimensions. Concerning the manufacturing of the panels, works studying the mechanical properties of sandwich panels manufactured by FDM are present in the literature, but they are limited to the fabrication of only the core of the panel or to single–material processes. Moreover, the characterization of both acoustic and mechanical properties is very often not present.

Table 2.4 Summary of the reported works concerning sandwich panels

Authors	**3D printed features**	**Sound Absorption**	**Main conclusions**
Yang *et al.* [121]	Not 3D printed	$\alpha > 0.75$ between 500 - 100 Hz	Honeycomb-corrugation hybrid core. Perforations on the core Only simulations
Meng *et al.* [122]	Facesheets and core	Absorption peak at ~500Hz	Perforations on the core increases sound absortion
Lin *et al.* [123]	Not 3D printed	$\alpha > 0.8$ between 100 - 2700 Hz	N/A
Peng *et al* [124]	Not 3D printed	$\alpha > 0.8$ between 100 - 2700 Hz	Nine resonant cells Only simulations
Sarvestani *et al.* [127], [128]	Facesheets and core	N/A	Use of different core geometries Flexural properties and energy absorption One-step FDM of single-material panels
Bagsik *et al.* [129]	Facesheets and core	N/A	Studied parameters: panel width, core wall thickness, top facesheet thickness, geometry and building orientation of the core Longitudinal cores had better mechanical properties
Pollard *et al.* [130] Li *et al.* [131]	Core	N/A	Use of different core geometries FDM core had higher compressive strength and lower specific strength than Nomex cores

CHAPTER 3 OBJECTIVES OF THE WORK

The challenges of manufacturing with FDM HTRTs, such as PEEK and PEI, are related to the high processing temperature and the high viscosity of the materials. The majority of the FDM 3D printers available on the market does not allow the processing of such materials, since a high-temperature printing head is necessary. In addition, a building platform capable of reaching relative high temperatures (~200°C) and a heated enclosure are necessary features to successfully 3D print HTRTs. Moreover, the high viscosity of the HTRTs in the molten state does not allow an easy processability of the materials, making the printing process very challenging. Therefore, researchers focused on the optimization of the processing parameters to obtain good quality prints, and not on the investigation of the mechanical properties.

Concerning the AM of sandwich panels, the majority of the works found in the literature focused on evaluating the acoustic properties of samples of reduced dimensions. The sample size limitation is due to the set-up for the acoustic characterization, e.g., the impedance tube test, that usually requires circular samples with a diameter ranging between 30 to 100 mm. Additionally, tests performed on sandwich panels of bigger dimensions would not allow a quick characterization since the fabrication by FDM would require a high amount of time. Moreover, there is a lack of information in the literature regarding multi-material FDM of sandwich panel.

The materials and the structures developed in the thesis are studied for aerospace applications. More specifically, the industrial partner of the project is interested in using 3D printed composite materials and sandwich panels in their jet engine fan cases. The thesis presents a preliminary study on the abovementioned topic.

Some requirements were established for the materials and the panels. The composite materials are supposed to be used in zones of the engine subjected to relatively high temperatures and mechanical stresses. Consequently, the composite material should have a Young's modulus of at least 15 GPa at room temperature and it should be able to maintain mechanical properties at a temperature of 100°C. Instead, the sandwich panels are supposed to be used for both acoustic and mechanical applications. The panels should be able to absorb sound over a frequency range of 500 Hz starting at 600-700 Hz. Moreover, they should be able to withstand mechanical load.

The selected 3D printing technology was FDM. These technologies allow the fabrication of thermoplastic composite with almost no limits on the printable geometry. The technology was preferred to other, such as SLS for two main reasons. First, FDM parts are characterized by the alignment of the fillers along the printing direction, allowing to obtain higher mechanical properties. Second, it allows the fabrication of hollow part, an essential feature for the fabrication of acoustic sandwich panels. Concerning the materials, PEEK and PEI were chosen based on their elevated T_g that allows them to be used as structural components at relative high temperature. CF were used because they are a filler that gives a very high stiffness to the composite when used as reinforcements for thermoplastic polymers.

Based on the abovementioned considerations, the followings objectives (O) and sub-objectives (S.O) have been determined for the project:

O. 1. FDM 3D printing of HTRT composite materials able to operate at relatively high service temperatures (i.e., >100°C) and having improved mechanical properties (E >15GPa).

- S.O. 1. Obtaining a composite filament suitable for FDM 3D printing with a small-scale process.
- S.O. 2. Performing a preliminary characterization of FDM extruded filaments.
- S.O. 3. Scale-up of the process and manufacturing of dogbone samples.

O. 2. FDM 3D printing of single and multi-material sandwich panels able to absorb sound over a wide range of frequencies (~500 Hz) and to sustain loads.

- S.O. 1. Development and acoustic characterization of the sandwich panel unit cell.
- S.O. 2. Manufacturing and mechanical characterization of sandwich panels.

CHAPTER 4 DEVELOPMENT AND AM OF HIGH-TEMPERATURE RESISTANT THERMOPLASTIC COMPOSITES

In this chapter, the development, the fabrication and the characterization of PEEK/CF, PEI/CF and PEEK/PEI/CF composites is reported. The composites were produced by two different melt mixing approaches. Then the composites were processed with an FDM machine to obtain thin filaments and additively manufactured parts. Thermal, mechanical microscopic and characterization were carried out on the HTRT composites.

4.1 Characterization techniques

Thermal properties have been evaluated with the aid of modulated DSC (m-DSC) to obtain the characteristic temperatures (i.e., T_g, T_m andT_c) of the materials. SEM and micro-computed tomography (μ-CT) analyses were carried out to obtain more information on the CFs and the microstructure of the materials. Finally, the mechanical properties of the fabricated materials were evaluated with the aid of tensile tests.

4.1.1 Thermal characterization

The m-DSC was used to measure the T_g of the materials. The tests were carried out in a DSC Q1000 TA instruments (New Castle,USA) at a rate of 20ºC/min and an amplitude of 1.27°C from 100°C to 200°C. The mass of the samples was ~10 mg. During m-DSC, the heating is performed applying a linear and a sinusoidal heating rate at the same time, instead of using just a linear heating rate as for the standard DSC. The use of two different heating rates allows to separate reversible and irreversible transitions caused by the heating [132]. Thus, the T_g is determinable with higher precision.

4.1.2 Mechanical characterization

Figure 4.1 shows the methodology that was used for the mechanical test of composites filaments. After being mixed (Figure 4.1a) and extruded with the FDM machine (Figure 4.1b), tensile mechanical tests were carried on the composite filaments. MTS Insight electromechanical testing machine (Eden Prairie, USA) was used for the test. The machine was equipped with a 100 N load cell. The filaments were incapsulated in epoxy tabs. Tests were carried out according to ASTM

D3822 standard [133]. Testing speed was set at 10 mm/s. Six filaments for each formulation were fabricated and tested. The composite threads were polished and annealed at 100, 150 and 200°C for 24h before the test. The displacement was measured with the aid of Direct Image Correlation (DIC) technique (Figure 4.1c). A speckle pattern was attached to the grips and placed right behind the filament (Figure 4.1d). Two high speed cameras took pictures each 250 ms during the test with the aid of Vicsnap software. Then the pictures were imported into VIC3D software to analyze the displacement of the speckle pattern. Therefore, DIC is used as a Linear Variable Differential Transformer (LVDT), i.e. a displacement sensor. The obtained data were used to compute the Young's modulus. The peak stress was not computed because the grips holding the filaments in place were applying a pressure on the filament, causing a stress concentration in these regions.

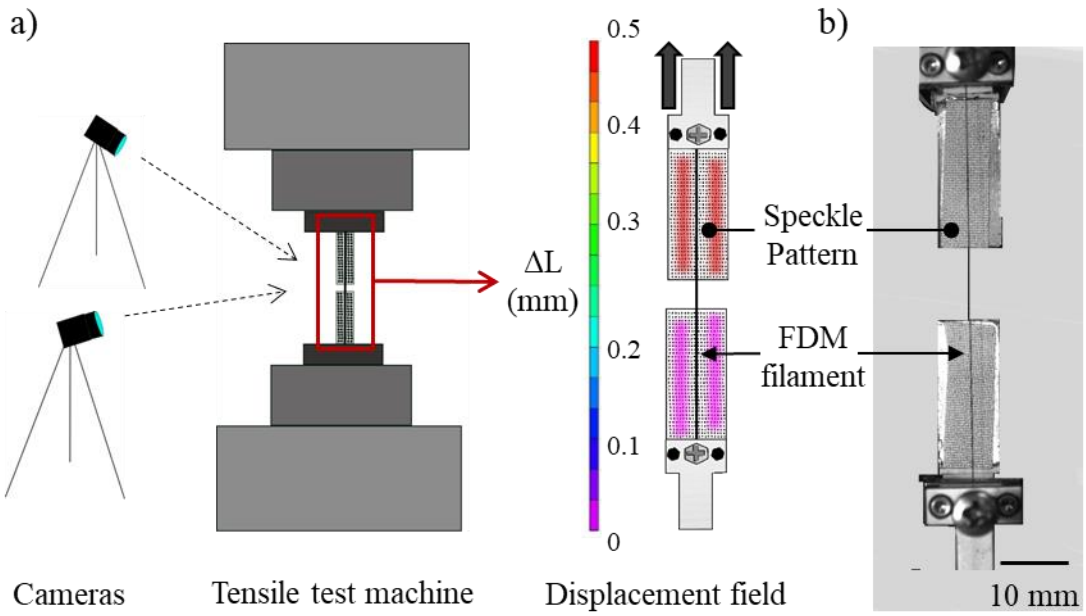

Figure 4.1 Methodology used for the mechanical characterization of composite filaments. a) Tensile test set-up that includes two high-speed camera and a tensile test machine, visualization of the displacement field. b) Picture of the testing set-up

Regarding the AM of tensile test specimens, the MTS Insight machine (Eden Prairie, USA) was equipped with a 50 kN load cell. Tests were carried out according to ASTM D638 standard [134]. ASTM Type IV as specimen geometry was used due to the limited amount of available material. Testing speed was set as 3.75 mm/s. Three samples per composite formulation were fabricated and

tested. The dogbones specimens were polished and annealed at 150°C for 24h before the tests. Figure 4.2 shows the specimen set-up for the DIC tensile test. The specimens were covered with a white paint and let them dry for 30 minutes. Then a speckle pattern was applied on the white paint. The DIC was used to measure the strain field on the surface of the composite. As a result, the deformation field of the entire region covered by the speckle pattern is computed.

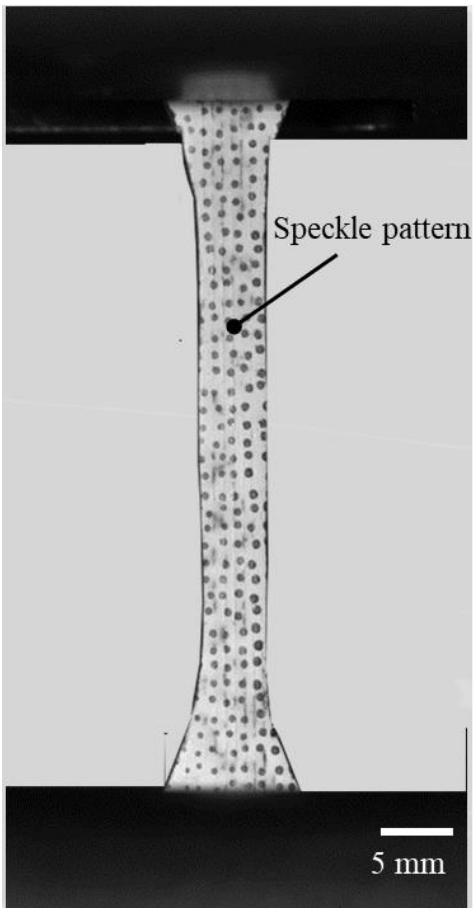

Figure 4.2 Pictures of the set-up for the mechanical characterization of the tensile test specimens. The location of the speckle pattern is highlighted

4.1.3 Microscopy

SEM was used to further understand the CFs interaction with PEEK, PEI or PEEK/PEI, as well as to observe the fracture surface of the composites. Before observation in the SEM, the samples were coated with gold to avoid electrostatic charge accumulation on the surface The microscope used in

this study is the JEOL JSM7600F (Peabody, USA), and it was operated at an acceleration voltage of 5 kV.

However, no information was available on the distribution of voids and CFs inside the material using SEM, since it is possible to only observe a cross-section and not the entire volume. To overcome this limitation, scans with µ-CT were carried out. µ-CT was performed to evaluate the distribution and the dispersion of the CFs inside the polymer matrix and the presence of porosity. A Xradia 520 Versa provide by Zeiss Canada (Toronto, Canada) and it was operated at an acceleration voltage of 50 kV, a power of 4 W and an exposure time of 10 s per scan.

4.2 Manufacturing and characterization of composite filaments

4.2.1 Mixing with micro-extruder

A micro-extruder was used. It allowed the processing of little amount of material (i.e., 5 cm^3) to perform a prelaminar characterization of the mixed composites.

PEEK 90G from Victrex (West Conshohocken, USA) and PEI ULTEM 1010 from Sabic (Long Sault, Canada) were mixed with chopped CFs. The CFs used above were Panex PX35 with 1.5wt.% sizing agent type 83 compatible with PEEK and PEI [135] from Zoltek Corporation (Bridgeton, USA). The materials properties are listed in Appendix A. The polymers and the CFs were dried overnight in an oven at 150ºC before mixing. The mixing was performed by using an Xplore micro-extruder (Sittard, Netherlands), shown in Figure 4.3. A 0.7 filling factor (i.e., the ratio between the volume of processed material and the volume of the mixing chamber) was selected to facilitate a good mixing of the CFs in the PEEK and PEI matrices and to avoid overflow of the mixture. The CFs and the polymer pellets were dry mixed by hand before being fed to the micro-extruder. Feeding of PEEK, PEI and CFs was carried out during 2-3 min, followed by a 10 min period of mixing. The extrusion was done at constant force to ensure a good homogeneity of diameter of the extruded composite filaments. The extruded filaments had a diameter of ~1.5-1.9 mm and a length of ~1.0-1.5 m. The temperature during mixing was set constant at 370ºC and the mixing speed was fixed to 100 rpm. Table 4.1 summarizes the different composites manufactured. The processed PEEK/PEI (wt.%/wt.%) concentrations were 90/10, 80/20, 70/30, 60/40, 50/50 and 40/60. CFs were added to the polymer matrix with a concentration of 30, 35, 40, 45 and 50wt.%.

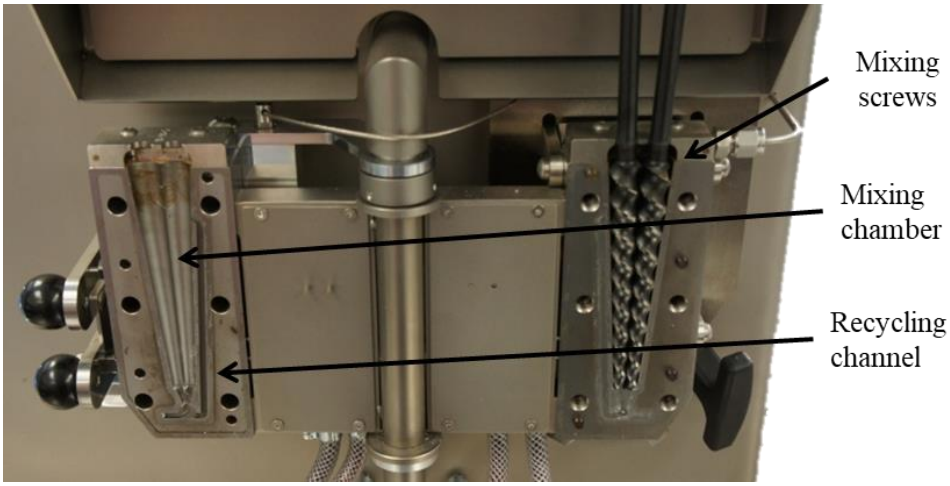

Figure 4.3 Image of Xplore micro-extruder used to mix PEEK and PEI with CFs. The locations of the mixing screw, the mixing chamber and the recycling channel are highlighted

Table 4.1 Summary of all the formulation obtained after mixing with the micro-extruder

PEEK 90G (wt.%[1])	**PEI (wt.%[1])**	**CF (wt.%)**
-	-	0, 30
-	30	0, 30
100	-	0, 30, 35, 40, 45, 50
90	10	0, 30
80	20	0, 30, 35, 40, 45
70	30	0, 30, 35
60	40	0, 30, 35, 40
50	50	0, 30
40	60	0, 30
-	100	0, 30

4.2.2 Manufacturing of FDM extruded filaments

Figure 4.4 sows the methodology used to obtain FDM extruded filaments. Thin filaments, with a diameter of ~0.3-0.6 mm, made of the composites previously processed with the micro-extruder (Section 4.2.1) were obtained using an FDM machine (AON M2 FDM 3D printer, Montréal, Canada). The 3D printer is equipped with a heated chamber that can go up to 120°C and a heated bed that can reach 200°C. The printer has also two independent extruders, manufactured by Dyze Design (Montréal, Canada), that can reach ~500°C. The composite filaments were fed into the FDM machine and extruded through the FDM nozzle. The diameter of the nozzle was 0.6 mm and the temperature was set to 400°C to ensure a good flow of the material. After the extrusion through the 3D printer nozzle, the filaments were cut to obtain six threads of ~15 cm long

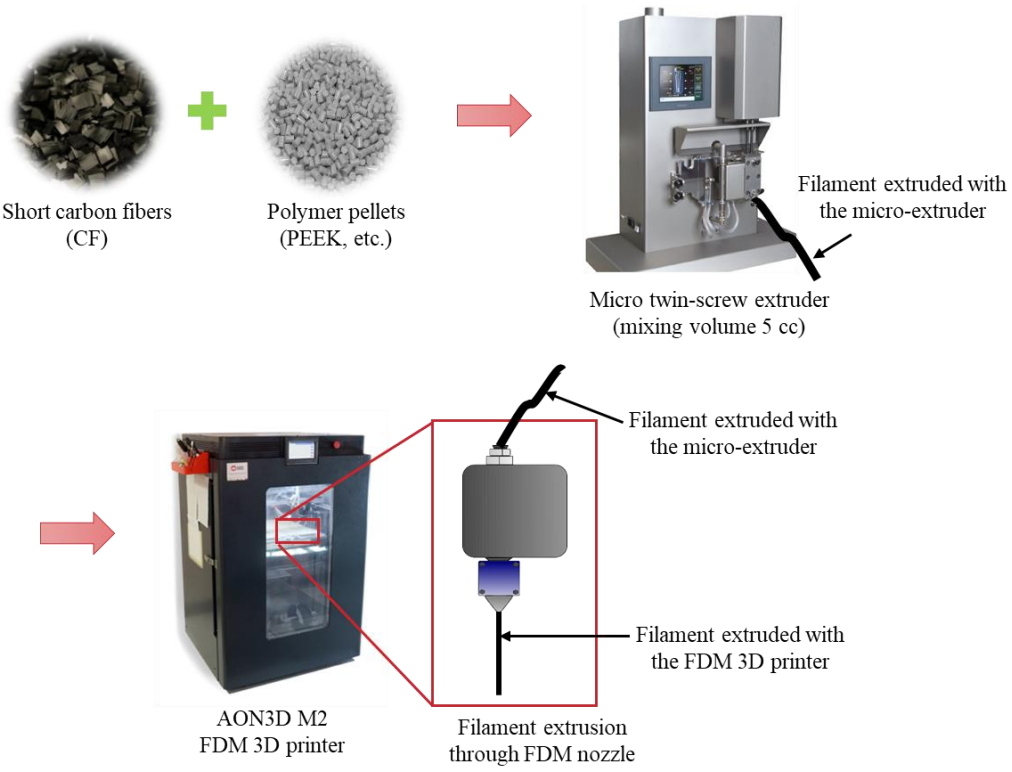

Figure 4.4 Schematic showing the methodology used for the fabrication of FDM extruded composite filaments. CFs and polymer pellets were mixed with the micro-extruder to obtain a diameter with a diameter suitable for the FDM machine (~1.75 mm). The filament is extruded a second time with the FDM printer to obtain a thinner filament with a dimeter of ~0.6 m

4.2.3 m-DSC results

Figure 4.5 shows the T_g predicted using the Fox equation (Section 2.3.3) and the T_g measured by m-DSC for each neat PEEK 90G/PEI composition. It can be observed that the glass transition temperatures obtained from m-DCS followed well the behavior predicted by the Fox equation. The maximum difference between the measured and predicted values was just 4.1°C. The glass transition temperature of the blends was intermediate between the one of PEEK (143°C) and of PEI (217°C). Moreover, the results highlighted that the addition of PEI in the blend led to an increase of the T_g. Therefore, the PEEK/PEI (90wt.%/10wt.%) blend had a T_g of 146°C (3°C higher than the one of PEEK) and the PEEK/PEI (40wt.%/60wt.%) blend of 178°C (35°C higher than the one of PEEK).

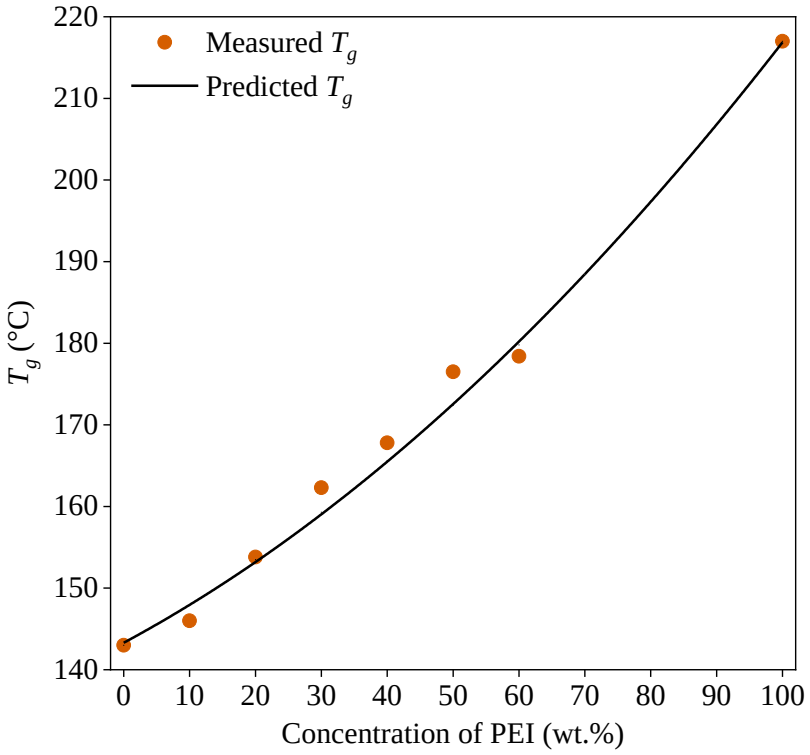

Figure 4.5 Comparison between the T_g predicted by the fox equation and the T_g measured with m-DSC for PEKK, PEI and PEEK/PEI neat polymers

4.2.4 SEM on composite filaments

Figure 4.6a shows the morphology of the fracture surface of PEEK/PEI (80wt.%/20wt.%)/CF 30wt.% filament after being processed with the micro-extruder. Thus, the PEEK/PEI (80wt.%/20wt.%)/CF 30wt.% composition was chosen to explain the results as relevant example. First, it is possible to observe an overall good dispersion of CFs inside the polymer matrix, since no big agglomerates of CFs are present. Moreover, CFs appears to be aligned along the extrusion or printing direction. However, air bubbles are detected and some of them are highlighted with arrows in the picture. The amount of these voids is important and they are homogeneously distributed inside the composite filament. Their size is around 30-60 μm. The air bubbles are probably generated during the mixing process, due to the difficulties in evacuating moisture gas or other volatiles because of the high viscosity of the molten composites. Figure 4.6b shows a magnified region of the abovementioned PEEK/PEI (80wt.%/20wt.%)/CF 30wt.% filament. In the picture, four arrows indicate the position of CFs that appear to be completely covered by the matrix, meaning that there is a good wetting between the CFs and the polymer matrix. No discontinuities at the interface between the polymer and the fibers are detected.

Figure 4.6c shows the morphology of PEEK/PEI (80wt.%/20wt.%)/CF 30wt.% filament after being extruded through the FDM nozzle. The morphology appears to be very similar to the one of the filament processed with the micro-extruder. However, a debonding of the CFs can be observed (Figure 4.6d). The debonding is probably caused by the mechanical force applied to the filament to create the surface fracture. Therefore, the FDM did not have a negative effect on the interaction between the fibers and the polymer matrix. shows a magnified region of the filament. μ-CT of CFs reinforced composites

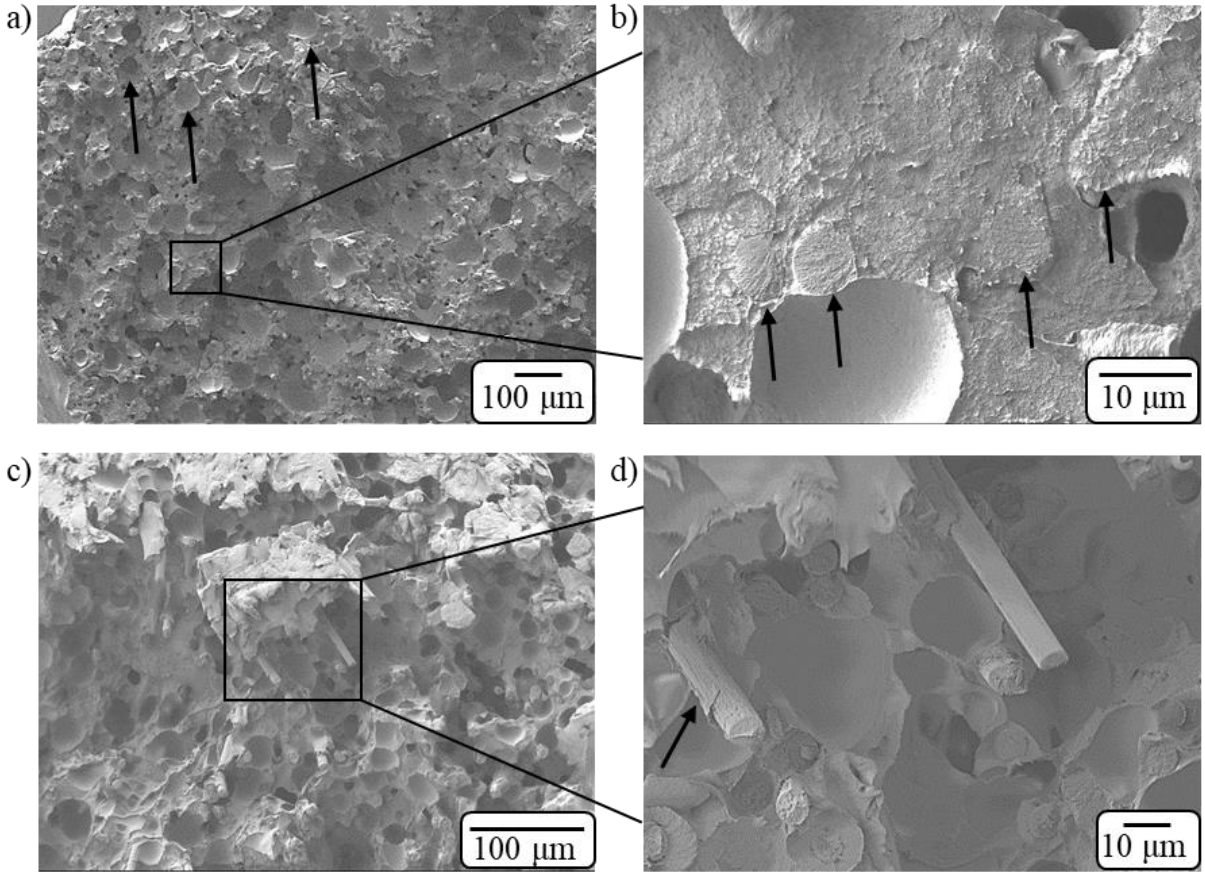

Figure 4.6 Representative SEM images of the fracture surface of PEEK/PEI (80wt.%/20wt.%)/CF 30wt.% after a,b) extrusion and c,d) 3D printing, showing presence of air bubbles, the distribution of CFs and the good wetting between CFs and the polymer matrix

4.2.5 µ-CT on composite filaments

The goal of the analysis of the µ-CT scans was to evaluate the amount of voids in the whole volume of the samples. In addition, the effect of processing the material with FDM on the porosity level will be evaluated. Figure 4.7 shows the images along the XY and the XZ planes of a PEEK/CF 40wt.% processed with the micro-extruder. The scans confirm the presence of the air bubbles, which can be observed in the whole volume of the extruded sample. The voids have a size of 80-100 µm. The µ-CT scans also clearly show the alignment of the fibers along the direction of extrusion (i.e. along the *z*-axis). The fibers appear to be as light grey circle, representing their radial

cross section, in the XY plane (Figure 4.7a), while in the YZ plane (Figure 4.7b) it is possible to observe their longitudinal cross-section. Their length varies from ~150 to ~250 µm.

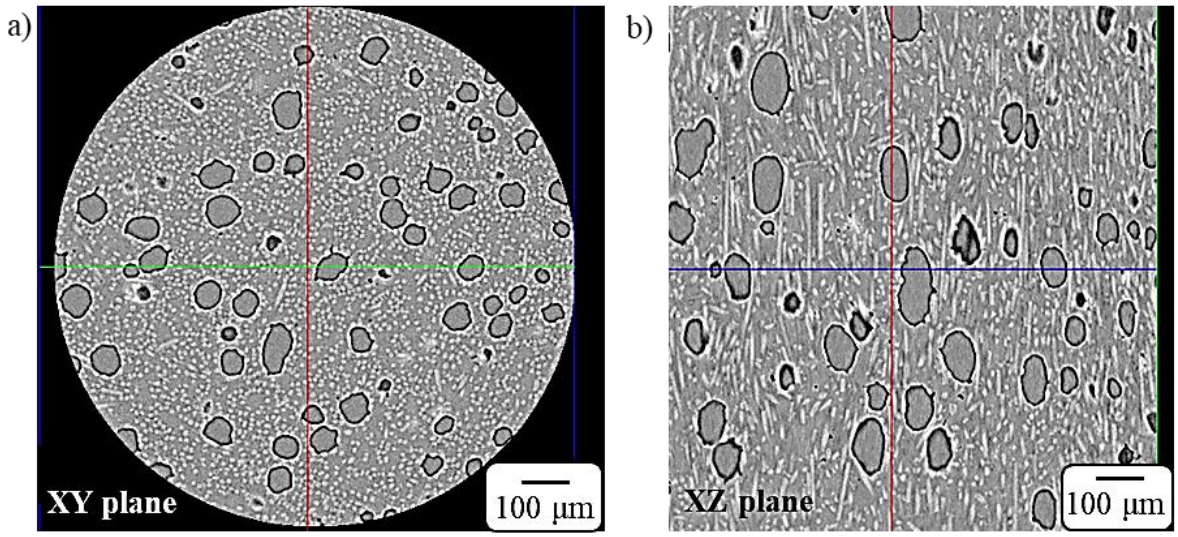

Figure 4.7 Images of µ-CT scans of a PEEK/CF 40wt.% processed with the micro-extruder along a) the XY and b) XZ plane

Figure 4.8a and Figure 4.8b show the scans along the XY plane of a PEEK/CF 40wt.% filament extruded form the FDM nozzle. The images still show the presence of air bubbles. However, the size of the voids is smaller for the FDM extruded filament, being ~40-60 µm, almost the half compared to the filaments processed with the micro-extruder. The reduction in size can be reconducted to the additional melting of the material that occurs during the printing process. In addition, it can be observed that the size of the voids is larger at the center of the filament than towards the external portions, probably due to the higher difficulties for moisture gas trapped inside the molten material to escape from the center of filament.

Figure 4.8-c and Figure 4.8d show the scans in the XY plane for a PEEK/PEI (80wt.%/20wt.%)/CF 30wt.%. It is possible to observe that the number of air bubbles is much lower than the case of PEEK/CF 40wt.%. The size of the air bubbles is slightly lower, at 30-40 µm. The important reduction in the void content might be explained by the lower viscosity of the polymer matrix, due the addition of PEI. A lower viscosity may facilitate air bubbles to the escape. However, the hypothesis was not verified by a rheological test.

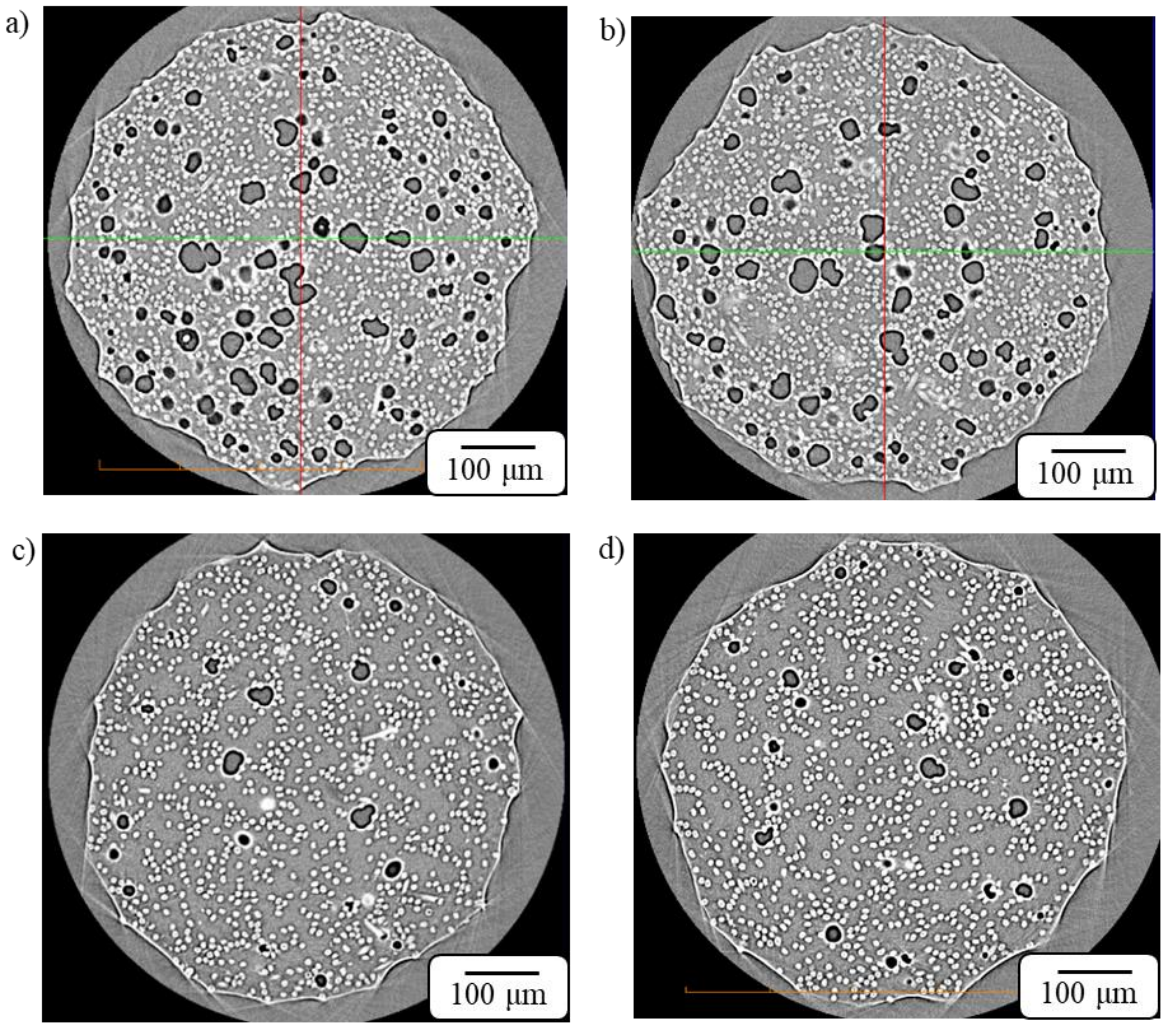

Figure 4.8 Images of µ-CT scans along two different XY planes of a) PEEK/CF 40 wt.% and b) PEEK/PEI (80wt.%/20wt.%)/CF 30wt.% extruded filaments with a 0.6 mm nozzle

4.2.6 Tensile test results on FDM extruded composite filaments

Figure 4.9a shows two representative stress-strain curves of neat PEEK 90G and PEEK 90G reinforced with 30wt.% of CFs supplied by Zoltek. Results showed that the portion of the curve in the elastic domain was much steeper for the composite than for the neat polymer. Additionally, the composite had a peak stress of 87 MPa and it broke at a deformation lower than 1%. The neat polymer, instead, had a lower peak stress (i.e., 78 MPa), but it showed plasticity after yielding, breaking at a deformation of 10%. Therefore, the composite was much stiffer and much more brittle.

Neat and CFs reinforced polymers featuring six different blend compositions, from PEEK/PEI (90wt.%/10wt.%) to PEEK/PEI (40wt.%/60wt.%), were tested. As before, CFs provided by Zoltek and a concentration of 30wt.% were chosen for all the formulations. Figure 4.9b shows the Young's modulus of the abovementioned neat and CF reinforce blends. The neat polymers showed similar values of Young's modulus between each others, ranging from 2.9 to 3.6 GPa. The PEEK/PEI (80wt.%/20wt.%) composition had the highest *E*, while PEEK/PEI (70wt.%/30wt.%) the lowest. Concerning the composites, PEEK/PEI (80wt.%/20wt.%) and PEEK/PEI (60wt.%/40wt.%) showed the best mechanical results, with a Young's modulus of 14.1 GPa and 14.0 GPa, respectively. Considering the statistical variations in the measurements, these values are comparable with that of the PEEK/CF 30 wt.%. The 90/10, 70/30, 50/50 and 40/60 PEEK/PEI (wt.%/wt.%) CFs reinforced blends exhibited lower mechanical properties. In the case of PEEK/PEI (50wt.%/50wt.%) and PEEK/PEI (40wt.%/60wt.%), the amount of PEI is probably too high, affecting the mechanical properties. However, it is still not clear the reason why the 80wt.%/20wt.% and 60wt.%/40wt.% compositions have a better Young's modulus than the one of 90wt.%/10wt.% and 70wt.%/30wt.%. To confirm our conclusions, the mixing of the whole compositions should be repeated.

The effect of the annealing temperature was investigated on PEEK/CF 30wt.% and PEEK/PEI/CF 30wt.% composite filaments. The composites were annealed at a temperature of 100, 150 and 200°C for 24h. Figure 4.10a shows the results of the mechanical tests. Considering the statistical variations in the measurements, only the PEEK/CF 30 wt.% and PEEK/PEI (90wt.%/10wt.%) composites showed a significant improvement in the Young's modulus when the annealing was performed at 200°C. The composites annealed at 150°C showed an increase in mechanical properties just for the PEEK/PEI (60wt.%/40wt.%) composite.

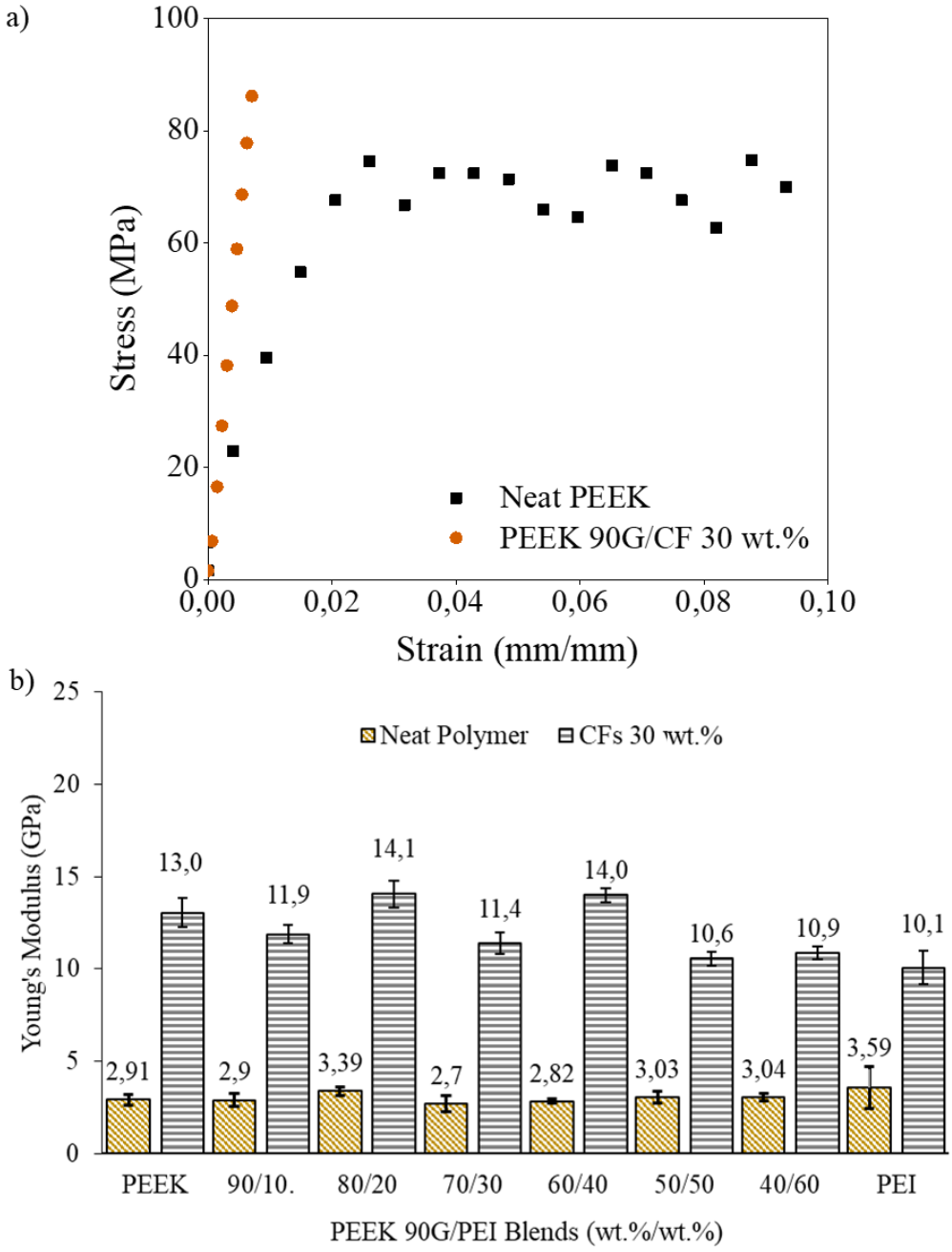

Figure 4.9 a) Representative stress-strain curves of neat and 30wt.% CFs reinforced PEEK extruded filaments. b) Effect on the Young's modulus of different PEEK/PEI blend polymer matrices on neat and 30wt.% CFs reinforced extruded filaments

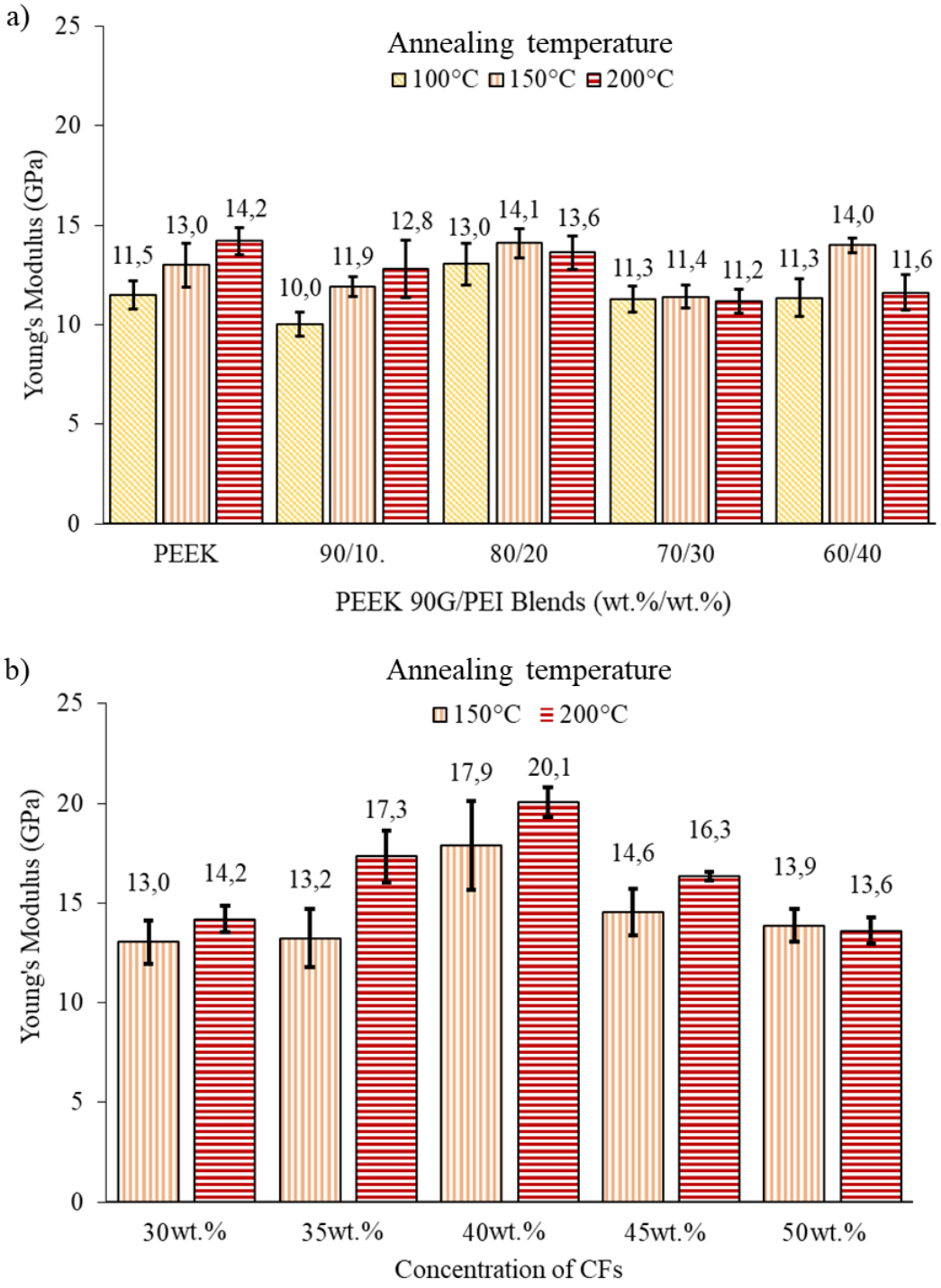

Figure 4.10 a) Effect on the Young's modulus of the annealing temperature of PEEK/PEI/CF composites. b) Effect of the concentration of CFs and of the annealing temperature on the Young's modulus of PEEK/CF composites

The effect of the concentration of CFs was also investigated. PEEK/CF filaments with 30, 35, 40, 45 and 50wt.% of CFs were annealed at 150 and 200°C. Figure 4.10b reports the values of Young's modulus. The composites having 40wt.% of CFs showed the best mechanical properties, with a modulus of 17.9 and 20.1 GPa for the samples annealed at 150 and 200°C, respectively. After 40wt.%, the value the Young's modulus decreased probably due to excessive breakage and/or agglomeration of the CFs. The composite with the highest concentration of CFs (50wt.%), showed the worst mechanical properties and a very high brittleness. It is possible to observe that samples annealed at 200°C showed a higher Young's modulus than the samples annealed at 150°C.

The PEEK/PEI formulations of 80wt.%/20wt.% and 70wt.%/30wt.% were selected in order to have the best compromise between a high Young's modulus and a high T_g. Consequently, these two formulations were processed with the Bülher and Brabender extruders. The PEEK/PEI (80wt.%/20wt.%) compositions exhibits the best mechanical properties, while PEEK/PEI (70wt.%/30wt.%) has a higher T_g. The composition 60wt.%/40wt.% was not chosen, even tough the good mechanical properties and the high T_g. PEI has a lower chemical resistance than PEEK, therefore the high amount of PEI in the 60wt.%/40wt.% blend could reduce the chemical resistance of the blend.

4.3 Manufacturing and characterization of composite dogbones

4.3.1 Mixing with Bülher and Brabender extruders

The mixing apparatus was changed due to the need of obtaining higher quantities of material to be able to fabricate additively manufactured parts. Figure 4.11 summarizes the whole process used to obtain composite filaments suitable for FDM. PEEK 90G from Victrex (West Conshohocken, USA) and PEI ULTEM 1010 from Sabic (Long Sault, Canada) were mixed with types of CFs: Panex PX35 with 1.5wt.% sizing agent type 83 compatible with PEEK and PEI from Zoltek Corporation (Bridgeton, USA). Analysis of the length of as received fibers was performed, the results can be found in Appendix B.

PEEK and PEEK/PEI blends were processed with CFs using the AST Research Center-National Research Council of Canada (NRC) facilities. The polymers and the CFs were dried overnight in an oven at 150°C before mixing. Polymers and CFs were mixed with a Bühler 20 mm twin-screw

extruder from Bühler Group (Uzwil, Switzerland). The extruder was set with the following temperature profile (from the feeding to the exit): 345-350-355-355-360°C. The rotation speed of the screws was 150 rpm and the total flow rate was 2 kg/h.The obtained composites were extruded and cut in pellets and dried for 3-4 h at 150°C.

The pellets were then processed with a Brabender single-screw extruder from Branbender Technologie GMBH & CO. KG (Duisburg, Germany) to obtain a filament of ~ 1.75 mm. The extruder temperature profile was 330-335-335-340°C, with the screw rotation speed set at 20 rpm. The filament diameter was controlled with the aid of a real-time monitoring system. After the extrusion, the filament was collected in a spool with Filabot Spooler form Filabot (Barre, USA). Finally, the spools were dried for an additional 3-4 h at 150°c and packed under vacuum in plastic bags. In both cases, the cooling of the filament was accelerated passing the extruded filament through a water bath. Table 4.2 summarizes all the processed formulations. PEEK was mixed with 30, 40 and 45wt.% of CFs provided by Zoltek. Attempts were made to mix PEEK with 50wt.% of CFs, however the material was not easily extrudable due to its excessive brittleness. PEEK/PEI blends were processed with 30wt.% of CFs provided by Zoltek. Based on the results obtained in the micro-extruder phase, the 80wt.%/20wt.% and 70wt.%/30wt.% PEEK/PEI concentrations were chosen.

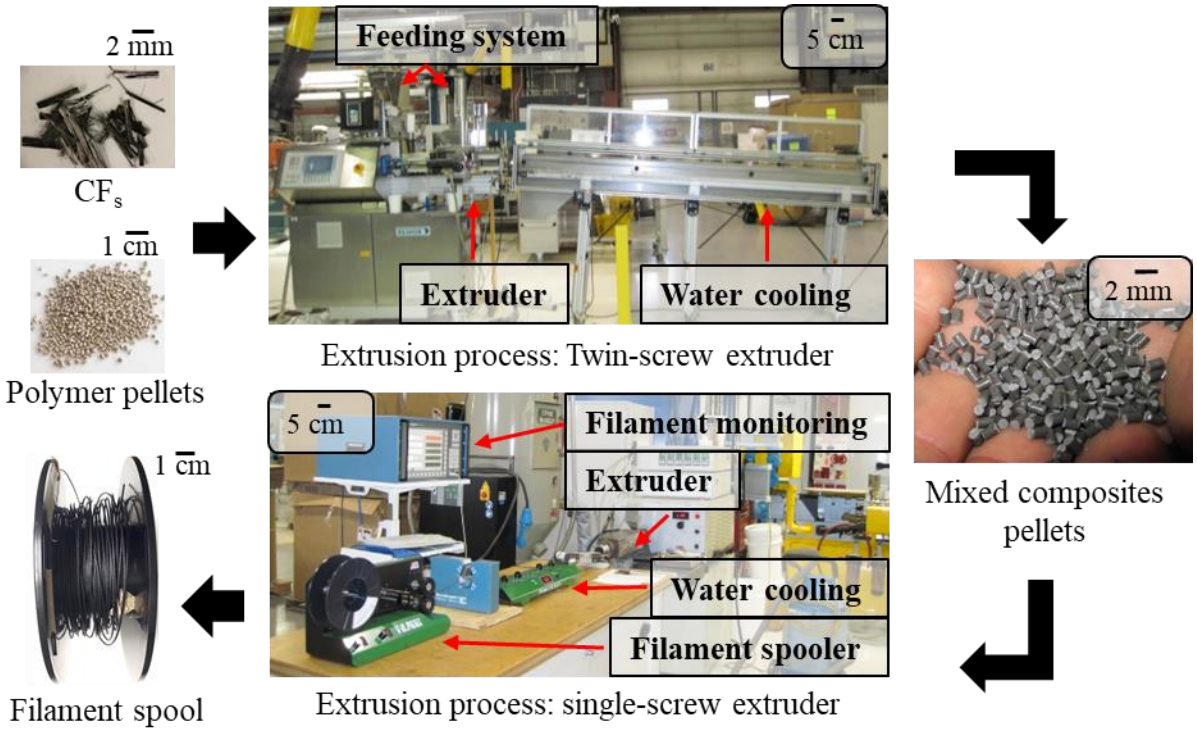

Figure 4.11 Set-up used to obtain composite filaments suitable for the FDM: CFs and PEEK or PEEK/PEI polymer pellets are fed into the twin-screw extruder, the composite is extruded and cut into pellets, these pellets are fed into the single-screw extruder and a spool of the mixed PEEK/PEI (70wt.%/30wt.%)/CF 30wt.% composite is obtained

Table 4.2 Formulation obtained after mixing with Bülher and Brabender extruders

PEEK 90G (wt.%[1])	**PEI (wt.%[2])**	**CFs concentration (wt.%)**
100	-	30, 40, 45
		30
		30
80	20	30
70	30	30

[1] With respect to total amount of polymer in the composite

4.3.2 Manufacturing of dogbone specimens

The composite materials obtained with Bülher and Brabender extruders were also processed with the FDM machine to fabricate tensile test specimens, i.e., Type IV dogbones (ASTM D638 [134]). Table 4.3 shows a summary of the characteristic of the printed specimens highlighting their printing parameters. The 3D printed formulations were: PEEK/CF 30wt.%, PEEK/CF 40wt.%, PEEK/PEI (80wt.%/20wt.%)/CF 30wt.% and PEEK/PEI (70wt.%/30wt.%)/CF 30wt.%. The formulation PEEK/CF 45wt.% was not printable. In this case, the brittleness of the filament was probably caused by the excessive amount of CFs in the composite. Since CFs are responsible for the brittle behavior of thermoplastic composites, a higher concentration of CFs leads to more brittle materials. It was found that in the case of PEEK/CF 45wt.%, the concentration of CFs was too high, due to the excessive brittleness of the composite.

Table 4.3 Printing temperatures, infill angle and number of printed samples

Composite (matrix/CFs wt.%)	**Printing parameters**	**Infill angle**	**No. of samples**	**Comments**
PEEK/CF 30wt.%	T_{extr} = 375°C T_b= 180°C	0° (FL)	6	Nozzle clogging experienced
		90° (FL)	3	Nozzle clogging experienced
PEEK/CF 40wt.%	T_{extr} = 375°C T_b= 200°C	0° (FL)	6	Nozzle clogging experienced T_b at 180°C caused warping
PEEK/PEI (80wt.%/20wt.%)/ CF 30wt.%	T_{extr} = 385°C T_b= 180°C	0° (FL)	6	Increase T_{extr} to 385°C improved printability
		90° (FL)	6	Increase T_{extr} to 385°C improved printability
PEEK/PEI (70wt.%/30wt.%)/ CF 30 wt.%	T_{extr} = 385°C T_b= 180°C	0° (FL)	6	Nozzle clogging experienced

The software Simplify 3D was chosen as the slicing tool. A nozzle with a diameter of 0.6 mm was used because smaller nozzles did not allow the extrusion of the composites. The use of a heated bed, a heated chamber and a raft, i.e. sacrificial layers on which the part is printed, were necessary to avoid warping during the printing process. Moreover, to promote the adhesion of the first layer, parts were printed on a PEI building platform. T_{ch} was set 120°C to be as close as possible to the T_g PEEK (i.e., 143°C). Two different infill angles were used: 0° and 90°, i.e., Flat Length (FL) and Flat Width (FW) configurations, respectively. One extra layer at the top and one at the bottom of the specimens were added with an infill angle of 90° for FL configuration and of 0° for FW as sacrificial layer for the polishing process. The samples were printed with a layer height of 0.2 mm and without shell. The printing speed was set at 30 mm/s to avoid warping, higher printing speed resulted in warping and detachment form the building platform.

To determine the other printing parameters, 5 cm-sided cubes were printed for each formulation to perform a preliminary printing test. The goal was to ensure that there was a zero air gap between adjacent rasters and to ensure a good flow of the materials through the FDM nozzle. For all the composites, it was found that a raster width of 0.68 mm and an extrusion multiplier (i.e. scaling factor of extruded material with respect to the nominal amount) of 0.95 gave no air gap between rasters. Regarding T_{extr}, initially it was found that a temperature of 375°C allowed a relatively easy printing of all the materials. However, the printing failure for dogbone samples made of PEEK/CF 30wt.% and PEEK/CF 40wt.% were due to nozzle clogging. Therefore, for the other materials, i.e., PEEK/PEI (80wt.%/20wt.%)/CF 30wt.% and PEEK/PEI (70wt.%/30wt.%)/CF 30wt.%, T_{extr} was raised to 385°C to lower the viscosity of the materials and facilitate the extrusion through the FDM nozzle.

4.3.3 μ-CT results on composite dogbones

Figure 4.12 shows the μ-CT scans on the XY, YZ and XY planes, as well as of a 3D reconstruction of the scanned volume of a 3D printed PEEK/PEI (80wt.%/20wt.%)/CF 30wt.% tensile test specimen to evaluate the microstructure of an actual 3D printed part. The specimes was printed in FL configuration, meaning that all the layers were oriented along one direction. Particular attention is given also to the quality of the interface between different printed layers. Clear discontinuities between the different layers were present and they are highlighted by the arrows in the images. The

porosity present at the interface of the printed layers is caused by the FDM process and could affect mechanical properties. The discontinuities might be related to the layer thickness and/or the extrusion multiplier values (i.e., 200 µm and 0.95, respectively). The layer thickness might be not optimal for this material and the extrusion multiplier should be higher to avoid the presence of the discontinuities.

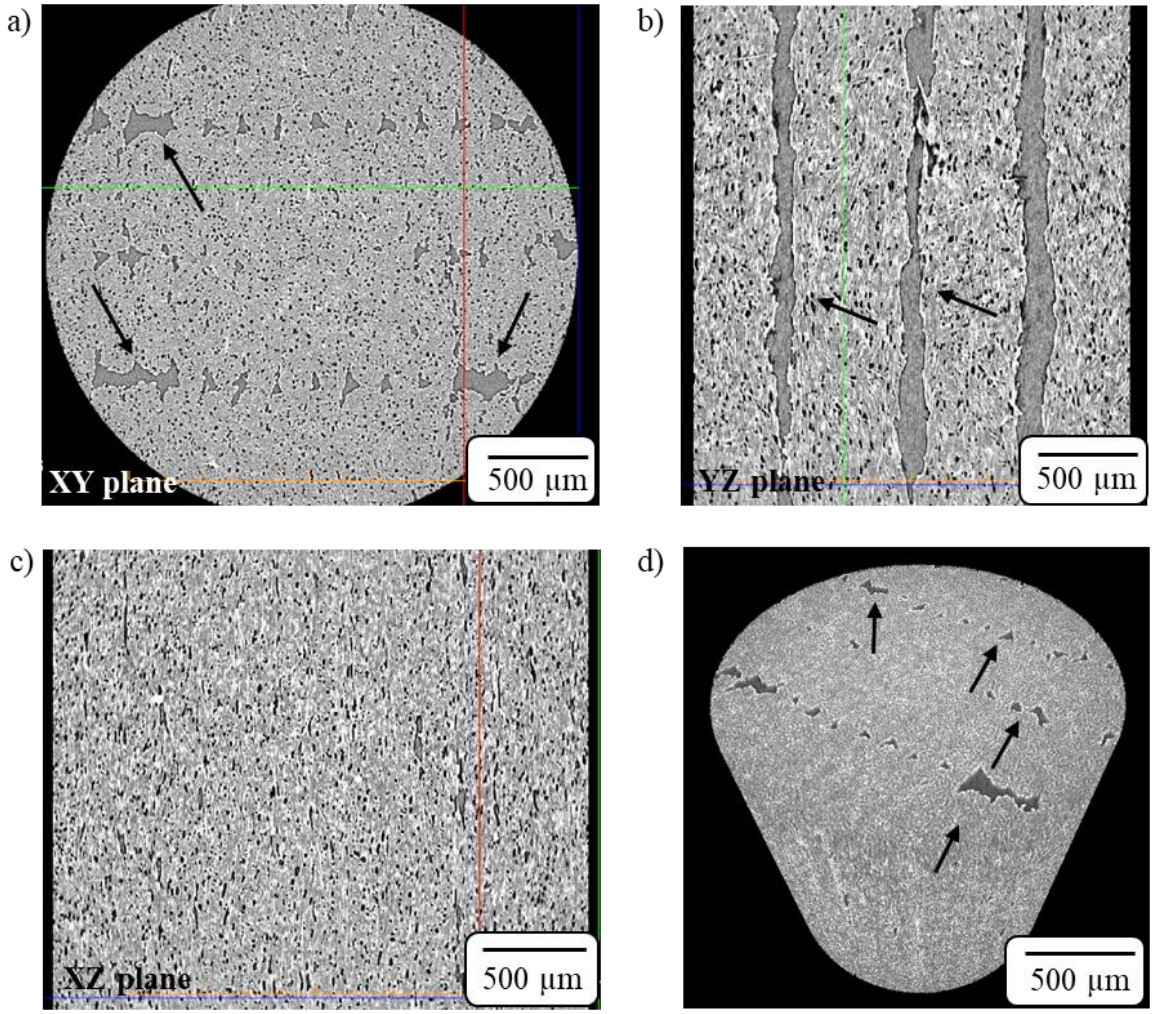

Figure 4.12 a-c) Images of µ-CT scans of a PEEK/PEI (80wt.%/20wt.%)/CF 30wt.% 3D printed dogbone along the a) XY, b) YZ and c) XZ planes. d) 3D reconstruction of the whole scanned volume

4.3.4 Tensile test results on 3D printed composite dogbones

Tensile tests were carried out on dogbones to evaluate the mechanical properties of additively manufactured parts. PEEK/CF 30wt.%, PEEK/CF 40wt.%, PEEK/PEI (80wt.%/20wt.%)/CF 30wt.% and PEEK/PEI (70wt.%/30wt.%)/CF 30wt.% tensile test specimens were successfully manufactured and tested. The dogbones made of PEEK/PEI (80wt.%/20wt.%)/CF 30wt.% printed at 385°C showed a better printability, with much less printing failures experienced. However, dogbones made of PEEK/PEI (70wt.%/30wt.%)/CF 30wt.% did not show a significant improvement in the printability and nozzle clogging was still present.The other formulation processed with the Bülher and Brabender extruders could not be processed with FDM, as explained in Section 4.2.2. The dogbones were printed in FL and FW configuration, as shown in Figure 4.13.

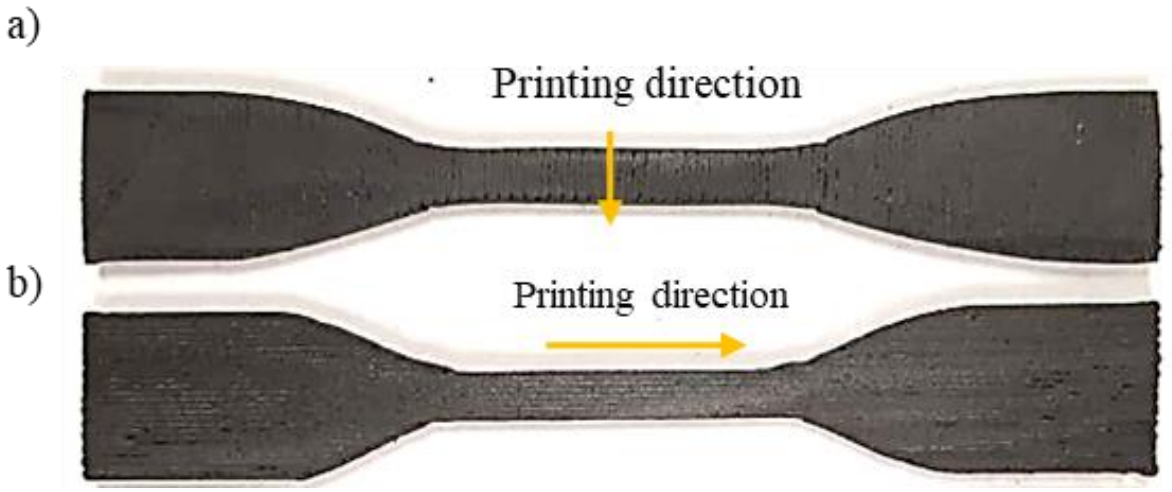

Figure 4.13 Dogbone samples made of PEEK/CF 30wt.% printed in FW (a) and FL configuration (b).

Two different batches were compared to evaluate the quality and the repeatability of the printing process. The FW configuration was not manufactured for PEEK/PEI (70wt.%/30wt.%)/CF 30wt.% and PEEK/CF40wt.% due to a lack of material. For the same reason, the second batch of dogbones was not manufactured for the PEEK/CF 30wt.% formulation.

Figure 4.14a shows the results of the mechanical tests of PEEK/CF dogbones printed in the FL configuration. PEEK/CF reinforced with 30wt.% shows a Young's modulus of 15.3 GPa, while the one reinforced with 40wt.% of 12.2 GPa. In addition, the Young's modulus of dogbone samples

coming from two different batches show similar values, however the difference in the error bars between the two set of measurements indicated that the process is characterized by a slight variability. Figure 4.14b shows the Young's modulus of PEEK/PEI (80wt.%/20wt.%) and PEEK/PEI (70wt.%/30wt.%) reinforced with 30wt.% of CFs. The highest Young's modulus (i.e. 16.6 GPa) was obtained for the PEEK/PEI (80wt.%/20wt.%)/CF 30wt.% printed in the FL configuration. These results are consistent with the Young's moduli obtained from the composite filaments. However, PEEK (70wt.%/30wt.%)/CF 30wt.% exhibited a lower modulus (i.e. 13.3 GPa).

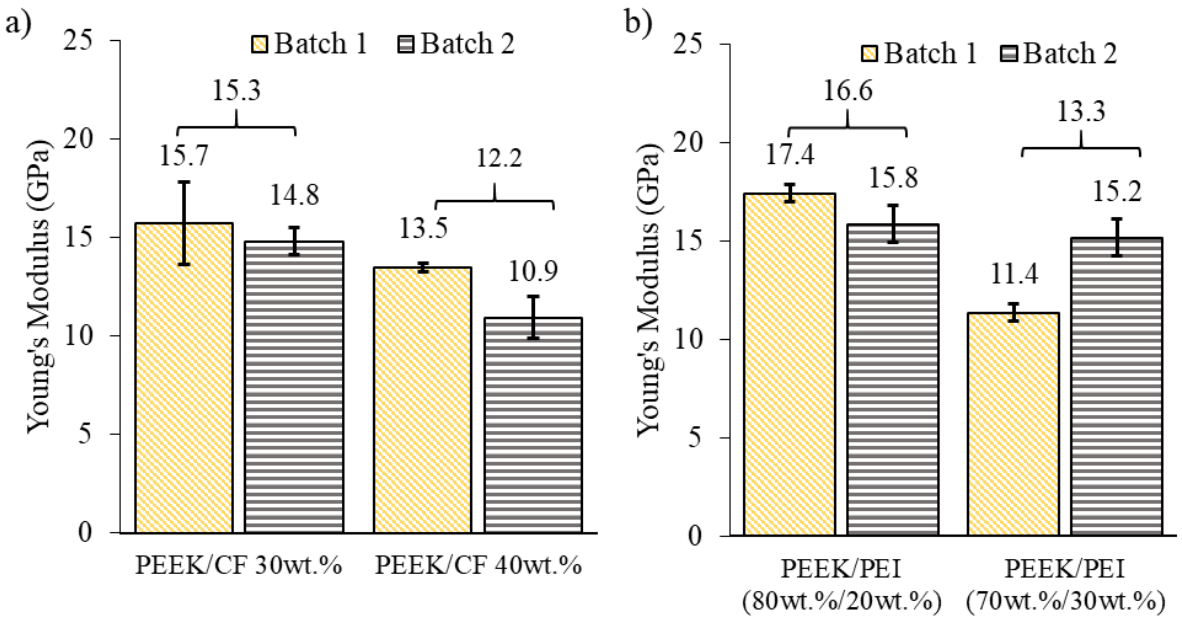

Figure 4.14 a) Young's modulus of PEEK/CF dogbone printed in the FL configuration at different concentration of CFs. b) Young's modulus of PEEK/PEI (80wt.%/20wt.%)/CF 30wt.% and PEEK/PEI (70wt.%/30wt.%)/CF 30wt.% dogbone samples printed in the FL configuration.

Figure 4.15 shows the different types of fracture observed during the tensile tests. It is possible to observe three main type of cracks: longitudinal, longitudinal originating at the fillet and transversal originating at the fillet. The longitudinal cracks propagate over the specimen length following the loading direction. The crack follows the interface between two adjacent rasters, probably due to a weak interface between them. The longitudinal and transversal cracks that start at the fillet of the tensile test specimen are probably due to the presence of a printing defects on the fillets, from which the crack originates.

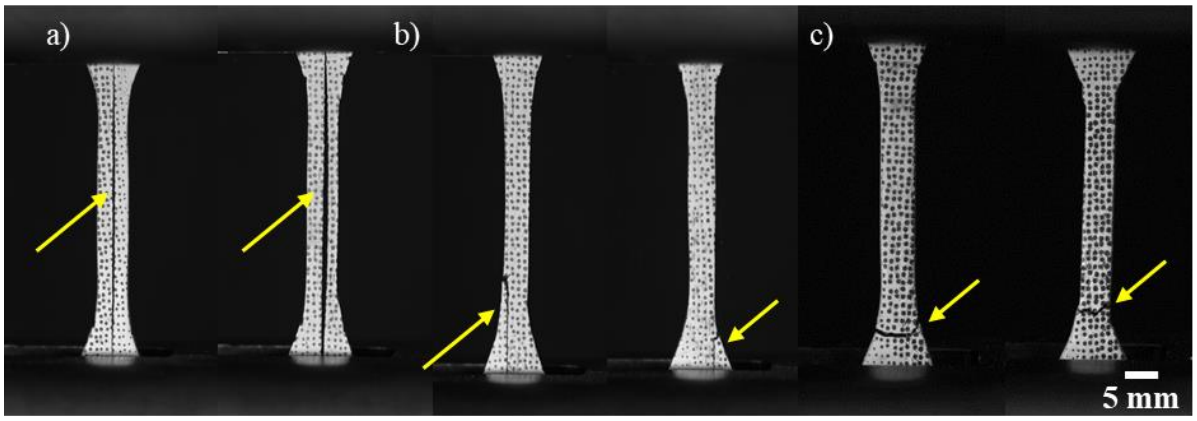

Figure 4.15 Pictures taken during the traction test showing different type of fractures on dogbone specimens printed in the FL configuration showing: a) a longitudinal crack, b) a longitudinal crack generated at the fillet, c) a transversal crack generated at the fillet. The arrows indicate the position of the cracks

4.4 Chapter conclusion

PEEK, PEI and PEEK/PEI blends were processed with CFs with the objective to prepare a composite for FDM applications. Thermal characterization was performed using m-DSC. The morphology and microstructure were observed with SEM and µ-CT scans. Tensile tests were carried out to evaluate the Young's modulus of 3D printed filaments and tensile test specimens

The addition of PEI to PEEK produced an increase in T_g, which is proportional to the concentration of PEI in the system. The trend of the experimentally measured T_g matched the values predicted by the Fox equation, proving the good miscibility of the blends and the quality of the mixing. The use of PEEK/PEI blends as polymer matrix instead of PEEK allowed to improve the service temperature of the material, which is directly related to the T_g, without renouncing to PEEK's properties, such as its chemical resistance.

SEM and µ-CT scans were carried out on extruded and additively manufactured specimens featuring CFs provided by Zoltek. SEM highlighted a good wetting between the CFs and the polymer matrix.. However, the presence of many air bubbles with a size of 80-100 µm was detected. The FDM process seems to have beneficial effects on the porosity, since the 3D printed composite filaments showed a reduction in the void size. In addition, 3D printed PEEK/PEI

(80wt.%/20wt.%)/CF 30wt.% showed a huge reduction in the amount of voids. The lower amount of air bubbles could be explained by the lower viscosity of the material, however further investigations are necessary to confirm this hypothesis. Scans of a 3D printed tensile test specimen highlighted the presence of a gap between adjacent layers, meaning that the printing parameters has to be improved to achieve a better layer-to-layer adhesion.

Mechanical tests were performed on 3D printed filaments and dogbone specimens. Table 4.4 reports a summary of the most relevant results for the two used mixing strategies, i.e. micro-extruder and Bühler and Brabender extruders. For the composite filaments processed with the micro-extruder, the best results were shown by PEEK/CF 40wt.%, which featured a modulus of 20.1 GPa. Among the blends, the PEEK/PEI (80wt.%/20wt.%)/CF 30wt.% had the best properties, with a Young modulus of 14.1 GPa. Moreover, it was observed that performing annealing the samples at a temperature higher than the T_g of PEEK provided a further increase of the stiffness.

Regarding the tensile tests of additively manufactured tensile test specimens, PEEK/CF 30wt.% and PEEK/PEI (80wt.%/20wt.%)/CF 30wt.% gave the highest Young's modulus (i.e. 15.3 and 16.6 GPa, respectively). The composite blends showed mechanical properties even superior to the ones obtained form tensile test of filaments, probably because the PEEK/PEI (80wt.%/20wt.%) featured a higher printability, which means that the material is able to flow better during the FDM printing process. A rheological study test would be an additional test to confirm this hypothesis.

Figure 4.16 compares polymer and composites materials available on the market and used for FDM with the HTRT composites developed in this project. Our composites had a higher Young's modulus that the composites commercially available. Therefore, our composites represent an improvement concerning the mechanical properties with respect to the materials that is possible to purchase nowadays. The comparison also proves that our composites could be interesting for the 3D printing and the aerospace industry.

In conclusion, HTRT composites reinforced with CFs were successfully mixed, 3D printed and characterized. PEEK/CF 30wt.% and PEEK/PEI (80wt.%/20wt.%)/CF 30wt.% seem to be the most suitable materials for FDM, since they showed good mechanical properties and good printability. Particular interest should be paid to the PEEK/PEI blends, especially the 80wt.%/20wt.%

composition, because it allows also to increase the T_g of the material and, consequently, increase its maximum service temperature.

Table 4.4 Summary of the tensile test results for PEEK/CF 30wt.%, PEEK/CF 40wt.%, PEEK/PEI (80wt.%/20wt.%)/CF 30wt.% and PEEK/PEI (70wt.% /30wt.%)/CF 30wt.%

Composite (matrix/CFs wt.%)	**Type of specimen**	**Mixing strategy**	**Young's modulus (GPa)**
PEEK/CF 30wt.%	Filament	Micro-extruder	14.2
	Filament	Bühler and Brabender extruders	17.9
	Dogbone FL	Bühler and Brabender extruders	15.3
PEEK/CF 40wt.%	Filament	Micro-extruder	20.1
	Filament	Bühler and Brabender extruders	12.6
	Dogbone FL	Bühler and Brabender extruders	12.2
PEEK/PEI (80wt.%/20wt.%)/ CF 30wt.%	Filament	Micro-extruder	14.1
	Filament	Bühler and Brabender extruders	13.0
	Dogbone FL	Bühler and Brabender extruders	16.6
PEEK/PEI (70wt.%/30wt.%) /CF 30wt.%	Filament	Micro-extruder	11.4
	Filament	Bühler and Brabender extruders	11.0
	Dogbone FL	Bühler and Brabender extruders	13.3

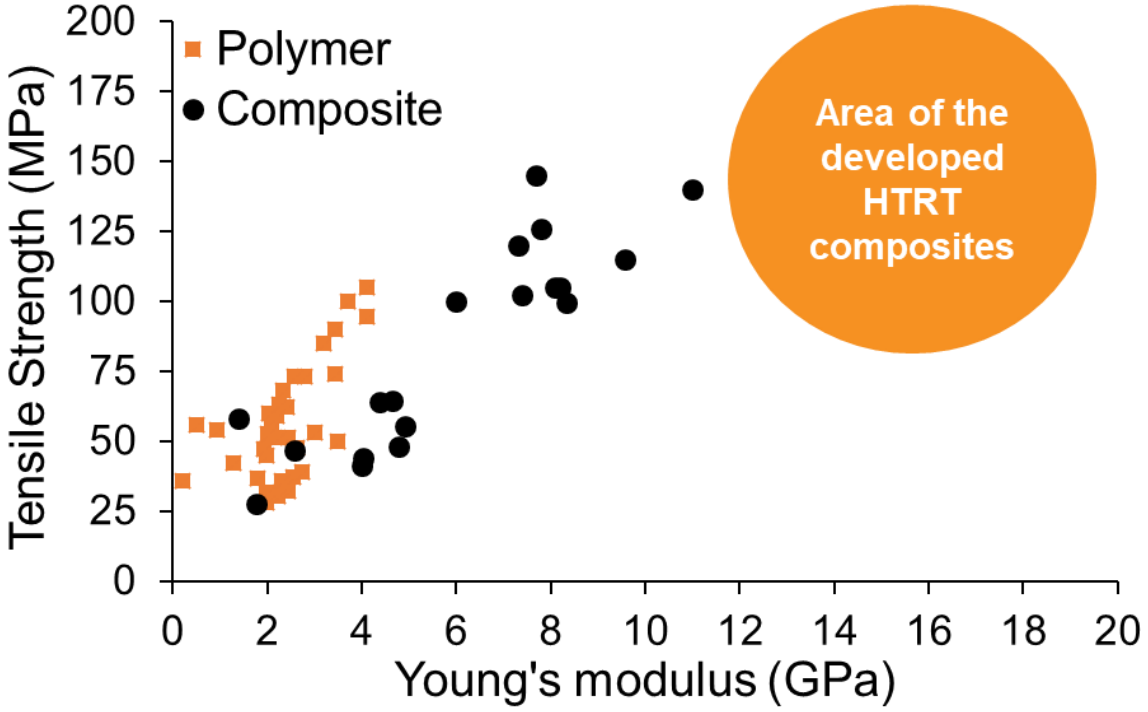

Figure 4.16 Comparison between the mechanical properties of commercially available polymer and composite used for FDM and the developed HTRT composites. Data extracted from *Senvol.com*

CHAPTER 5 DEVELOPMENT AND ADDITIVE MANUFACTURING OF SANDWICH PANELS FOR SOUND ABSORPTION

In this chapter the development and the fabrication of sandwich panels for sound absorption are reported. Firstly, the development of the repetitive units of the sandwich panels is explained. Then, the absorption coefficient of the structure is evaluated with the aid of impedance tube tests. Finally, the mechanical properties of additively manufactured sandwich panels are investigated with the aid of a 3-point bending test.

5.1 Materials and FDM

A Pro2 FDM 3D printer (Raise3D, USA) was used. The printer has a dual extruder, equipped with 0.4 mm diameter nozzles and a cooling fan. The extruders can reach up to 300°C, while the building platform can be heated up to 110°C. A heated enclosure is not available. Simplify3D was chosen as slicing software.

The selected material to fabricate the acoustic samples was Raise3D Premium PLA filament (Raise3D, USA). PLA is the ideal candidate to perform preliminary studies due to its low price and printing ease. Therefore, all the acoustic measurements were performed on PLA additive manufactured samples. T_{extr} was set at 210°C and T_b at 60°C. The extrusion width was 0.4 mm, the extrusion multiplier 0.9 and the printing speed 60 mm/s. The infill angle was ±45° and the layer height 0.2 mm. The cooling fan was kept at 60% of its full speed for all the layers, unless for the first one, for which the cooling fan was turned off to promote a better adhesion to the printing bed.

Sandwich panels were fabricated using Raise3D Premium PLA (Raise3D, USA), Carbon Fiber Reinforced (CFR) PA (3DXTech, USA) and alloy 910 (Taulman, USA) as neat PA, also known as nylon. All the panels were printed with an infill angle of 0° for the facesheets and ±45° for the core. 0° was chosen to maximize the mechanical properties of the facesheets, thanks to the alignment of the fibers during the printing process. The layer height was set as 0.25 mm to reduce the printing time and the printing speed was 60 mm/s. The cooling settings were the same as the ones describe for the acoustic samples, with the exception for the top facesheet. The cooling fan was set at 100% due to the presence of suspended zones, i.e. bridging layer. Without a cooling fan, the first layers of the top facesheet was not able to cool down quickly enough, creating printing defects. Concerning the other printing parameters, for PLA panels the same parameters as the ones

previously described for the acoustic samples were used. While, for PA panels, the T_{extr} and the T_b were 255°C and 80°C. The extrusion width was set at 0.3 mm while the extrusion multiplier at 0.83. The printing parameters were chosen based on a previous work carried out at LM2 [136] and after the printing of some test samples. A detailed table showing the printing parameters for the abovementioned materials can be found in Appendix I.

A multi-material process was also developed to additively manufacture sandwich panels featuring two different materials for the facesheets and the core. The facesheet were fabricated with CFR PA, because the skins of the panel need to have higher stiffness. While the core was fabricated with neat PA, since usually sandwich panels have a more compliant core with respect to the facesheets. It was not possible to use the materials developed in Chapter 3 due to time reasons. The use of an ooze shield, i.e. a printing feature that avoids contaminations between different printing materials, was used to avoid printing defects.

5.2 Characterization techniques

5.2.1 Acoustic characterization

Acoustic characterization was carried out at LAVA facilities at Polytechnique Montréal. The impedance tube, also known as Kundt's tube, tests were carried out to evaluate the absorption coefficient of the developed unit cells. The acoustic samples were circular, with a diameter of 29.8 mm, to fit inside the tube. ASTM E1050 standard was followed to perform the test [137]. The impedance tube was equipped with two microphones with hardbacking configuration and the measured frequency range was between 500 and 7000 Hz. In addition, the presence of an external wall on the samples is necessary in order to avoid air leakage between different chambers.

An acoustic optimization was performed to improve the acoustic behavior of the structures. First, the behavior of a single resonator was modeled using the Stinston model [138]. The model was adjusted by implementing the parameter *E,* which takes into account the loss at the edge of the resonator neck, following Komin *et al.* approach [99]. Then, the behavior of multiple resonators was computed summing the admittances (i.e. the inverse of the impedance) of each resonator. Finally, the optimization is performed using the Nelder-Mead algorithm [139].

5.2.2 Mechanical characterization

3-point bending test was carried out on the 3D printed structures in order to evaluate their mechanical performances. The MTS Insight electromechanical testing machine (Eden Prairie, USA), equipped with a 50 kN load cell, was used to perform the tests. Preliminary tests were performed on sandwich panels made of PLA, CFR PA and CFR PA/neat PA without the presence perforations on the top facesheet to evaluate the mechanical properties of the structures in the absence of additional features that could have weakened the structures. The sandwich panel were placed above supports with a span length of 100 mm. A testing speed of 2 mm/min was chosen. Finally, a test on samples of bigger dimension made CFR PA with perforations was performed. The test was carried out according to ASTM C393 standard [140]. Therefore, the span length was set as 150 mm and the speed was kept at 2 mm/min.

5.3 Sandwich panels geometry

The unit cells were developed to contain single and multiple Helmholtz resonators. Helmholtz resonators have been described in Section 2.4.1. Figure 5.1 shows the schematic of a traditional Helmholtz resonator compared with two that have been used in this work. The neck of the Helmholtz resonators is represented in blue, while the cavity is in green. Since the unit cells were supposed to be used in a sandwich panels, the perforated top facesheet was the neck of the resonators. The cavity of the resonator, instead, was used as the core of the sandwich panel. Figure 5.2 shows the geometry of the unit cell. The basic unit of the unit cell is a trapezoidal prism (Figure 5.2a, Figure 5.2b, and Figure 5.2c). The unit cell is constituted by four prisms, with two of them rotated 90°. An external wall confines the four prism and creates an additional cavity that comprise the volume between the four prisms (Figure 5.2d and Figure 5.2e). Thus, two different types of cavities were created, i.e., the internal cavity of each trapezoidal prism and the one between each prism. The central cavity has a bigger volume than the prism cavity, allowing the sound absorption at lower frequencies.

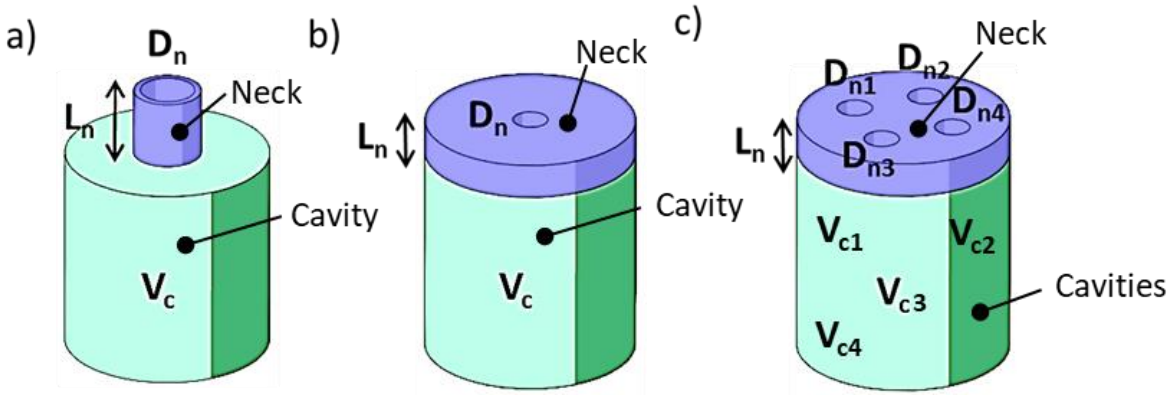

Figure 5.1 a) Traditional representation of a Helmholtz resonator, b) Helmholtz resonator with a facesheet featuring a single neck, c) Helmholtz resonator with a facesheet featuring multiple necks. L_n represents the neck length, D_{ni} the neck diameters and V_{ci} the volume of the cavities.

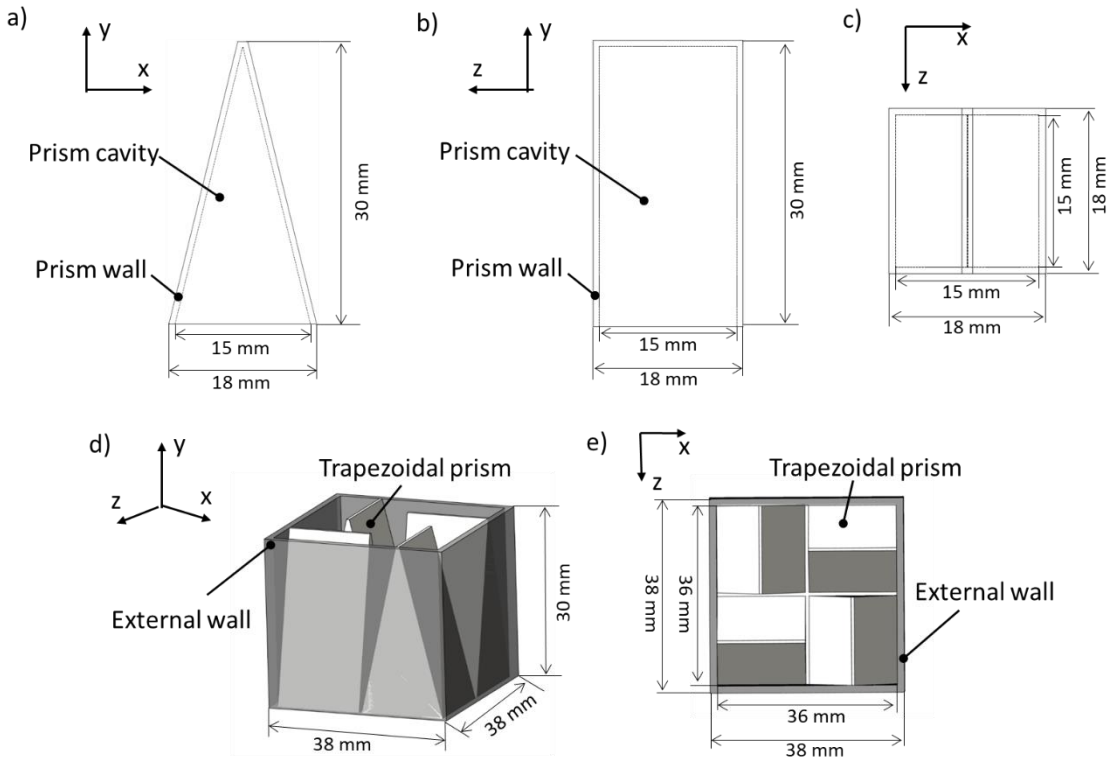

Figure 5.2 a,b) Side views of the trapezoidal prism; c) Top view of the trapezoidal prism, d) Isometric view of the repetitive cell and the external wall; e) Top view of the repetitive cell and the external wall.

The geometries that were developed and tested featured one, three, four and five resonators on each repeating unit respectively. The geometric values of each configurations, i.e. neck diameter, neck thickness and total thickness, are represented in Table 5.1. The size and the number of prisms were chosen in order to have a specimen of the appropriate size for the acoustic tests, due to the geometrical limitations imposed by the Kundt's tube.

Based on the result of the acoustic tests (Section 5.4), the geometries featuring three and five resonators were selected as the most promising. Sandwich panels with a 4×2 and a 6×2 array of repetitive cells have been developed. The dimensions of the 3D printed sandwich panels are reported in Table 5.2. The thickness of the facesheets, and of the core were set at 3 mm and 30 mm, respectively. The choice was made after inputs from Safran Composites and preliminary acoustic tests. Figure 5.3 shows the schematics of the sandwich panel featuring the three and five Helmholtz resonators core geometry. The facesheets of the sandwich panels are in blue and the core is in green. It is also possible to observe the presence of fillets at the narrow tip of the trapezoidal prism. The addition of fillets was done to increase printing ease. For sandwich panels without fillets, failures during the printing process were experienced more frequently.

Table 5.1 Measurement of the main geometrical features or the proposed acoustic structures

Configuration	**Neck diameter (mm)**	**Neck thickness (mm)**	**Core thickness (mm)**
Single resonator	2 and 3	1.5, 3	30
Three resonators	2, 2.5, 3 and 2.5, 2.5, 3	4	30
Five resonators	2, 2.5, 3, 3, 3.5	1, 2, 3, 4	30
Five resonators (optimized)	1.52, 1.74, 2.03, 2.25, 4.06	3	30

Table 5.2 Sandwich panel dimensions

Sandwich panel configuration	Length (mm)	Width (mm)	Number of unit cells
Three resonators	144	72	4×2
Five resonators	164	80	4×2
	220	80	6×2

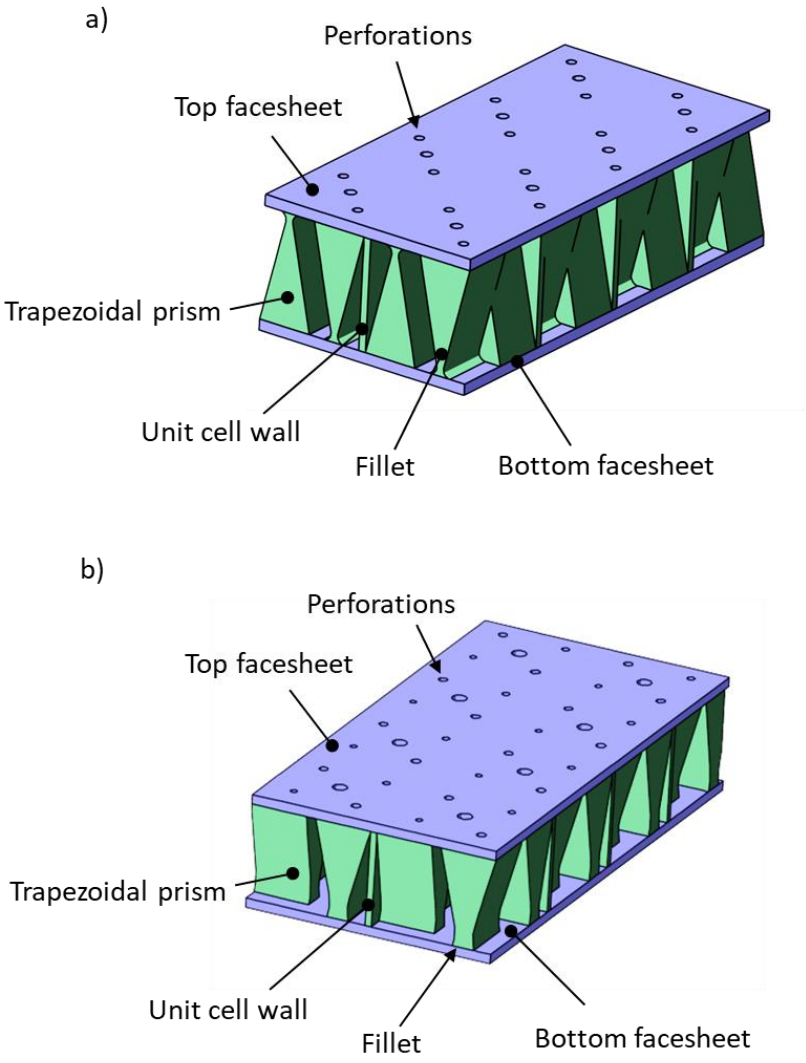

Figure 5.3 Schematics of sandwich panel with the a) three resonators and b) five resonators configurations

5.4 Impedance tube test results

Impedance tube tests were performed on acoustic samples featuring a single, three and five Helmholtz resonators. The results of a configuration featuring four Helmholtz resonators are reported in Appendix J.

5.4.1 Single resonator configuration

Figure 5.4 shows the results of the absorption test. The curves of six samples with different geometrical features are reported. The effect of the variation of the aperture diameter and neck thickness was evaluated. Firstly, the diameter was fixed at 3 mm and the neck thickness was set as 1.5, 3 and 4 mm (Figure 5.4a). The resonant frequency was shifted towards lower values increasing the neck thickness. Then, the neck thickness was fixed at 3 mm and the neck diameter was set at 2, 2.5 and 3 mm (Figure 5.4b). The resonant frequency was shifted towards lower values decreasing the neck diameter. Thus, it is possible to target a specific frequency to absorb changing D_n, L_n and V_c. The possibility of customizing the absorbed frequencies of the structure based on the specific needs represents a key aspect of the work.

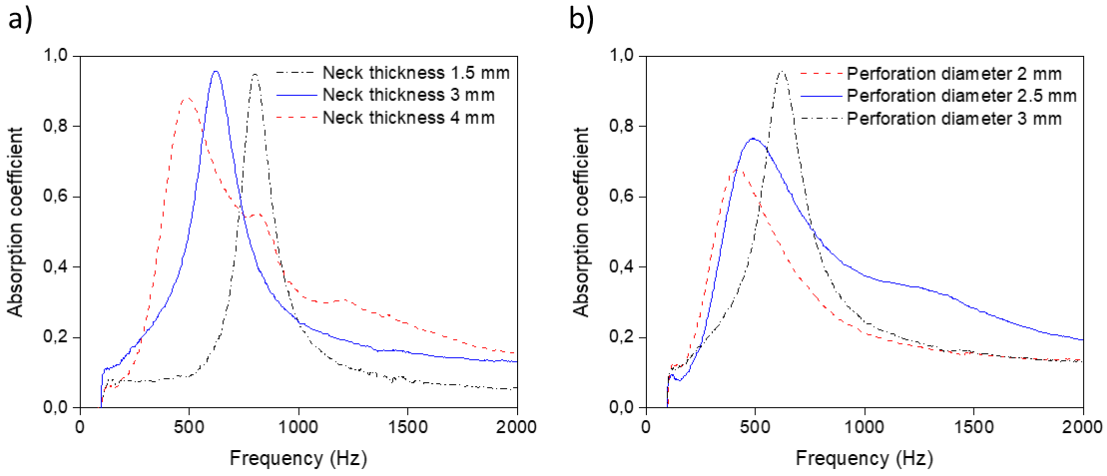

Figure 5.4 a) Absorption coefficient of three samples featuring one neck with a diameter of 3 mm and a neck thickness of 1.5, 3 and 4 mm. b) Absorption coefficient of three samples featuring one neck with a neck thickness of 3 mm and a neck diameter of 2, 2.5 and 3 mm.

In addition, it is possible to observe the presence of two secondary peaks for the sample featuring a neck thickness of 4 mm and a neck diameter of 3 mm. The appearance of the secondary peaks

was unexpected. Their presence could be explained by harmonics, since the secondary peaks are located at ~800 Hz and ~1200 Hz, which are multiples of the natural frequency of the resonator, that is at ~400 Hz. However, this is only a hypothesis and requires a further investigation, finding the source of the secondary peaks.

5.4.2 Three resonators configuration

Proven the capability of obtaining high absorption peaks and the possibility of selecting the desired resonant frequency, two different structures featuring multiple Helmholtz resonators were developed. The structures had three and five necks with different dimensions and, consequently, three and five Helmholtz resonators, respectively. The goal was to obtain multiple absorption peaks changing the necks diameters and keeping fixed the neck thickness and the cavity volumes.

Figure 5.5 shows the geometry of the sample featuring three Helmholtz resonators and the result of the impedance tube tests. The geometry of the unit cell was modified to achieve high absorption at relatively low frequencies. Two trapezoidal prisms were rotated 180°. Thus, it was possible to put a hole above the central cavity, i.e. the cavity between the four prisms. Moreover, the remaining two holes were placed above the rotated prisms (Figure 5.5a). Acoustic test revealed the presence of three absorption peaks (Figure 5.5b). The resonator featuring the central cavity generates the peak at low frequency (~500 Hz), while the resonators featuring the trapezoidal prism cavities generates the two peaks at higher frequencies (~1100 and 1400 Hz). However, the acoustic behaviour could be improved changing the diameter of the necks to achieve sound absorption also in the frequency range between 600 and 1000 Hz. The use of two different type of cavities, i.e. central and prism cavities, represented one key aspect that allowed us to achieve this result. Without the use of the central cavity, whose volume is bigger, absorption at relatively low frequencies would not have been possible.

5.4.3 Five resonators configuration

Figure 5.6 shows the geometry of the sample featuring five Helmholtz resonators and the result of the impedance tube tests. The core geometry is the same as the one of the samples having one Helmholtz resonator. A hole was placed above each prism cavity in order to have one resonator for each trapezoidal prism. An additional neck is present at the center of the specimen, that is placed

above the central cavity between the trapezoidal prisms (Figure 5.6a). The acoustic test revealed a high absorption peak at low frequencies (~600 Hz) and four peaks at higher frequencies (~800, 1100, 1400 and 1500 Hz). The use of two additional resonators allowed to have sound absorption over a wider range of frequencies. Indeed, sound absorption between 500 and 1500 Hz was obtained (Figure 5.6c). Unlike the sample with three resonators, the region between 600 and 1000 Hz presented good sound absorption levels.

Then, we investigated the effect o the absorption coefficient of each resonator in the structures featuring five and three Helmholtz resonators. Figure 5.7 shows the comparison in the absorption behavior of samples with all the resonators acting at the same time and of each resonator of the same sample acting alone. The results highlighted that the absorption peak given by a single resonator fit the corresponding peak of the global structure, showing that the absorption curve of the whole sample is generated by the contribution of each resonator. Therefore, the developed unit cells relied on the possibility of specific frequencies changing the geometrical features of the structure.

Figure 5.8 shows an example in which the neck diameters of the structure having five Helmholtz resonators were optimized to maximize the absorption coefficient. The structure was optimized thanks to an analytical model developed by the Ph.D. candidate Jean Boulvert, which is working in the LAVA research group leaded by Prof. Annie Ross. After the optimization, the neck diameters were set to 1.52, 1.74, 2.03, 2.25 and 4.06 mm, while the neck thickness was kept at 3 mm. The impedance tube tests highlighted that the average absorption coefficient of the optimized structure is higher than the non-optimized one (i.e., 0.95 compared to 0.85), even though the frequency range in which sound is absorbed is reduced. With the optimized neck diameters, sound absorption level greater than 0.9 was obtained for the frequency range between 700 and 1250 Hz. The optimized specimen was the one showing the best acoustic performances, proving that an acoustic optimization is essential to obtain a high absorption over a wide range of frequency. In addition, the result shows the feasibility of obtaining absorption close to one over ~550 Hz.

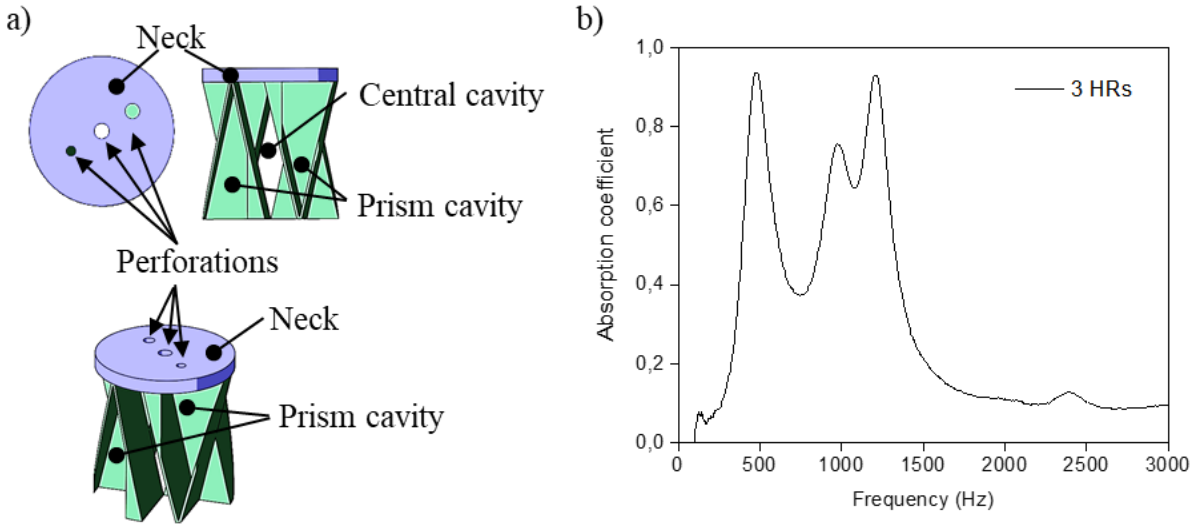

Figure 5.5 a) Top, side and isometric view of the sample for acoustic tests featuring three resonators. b) Absorption coefficient of the samples featuring three resonators with a neck thickness 4 mm and neck diameters of 2, 2.5 and 3 mm.

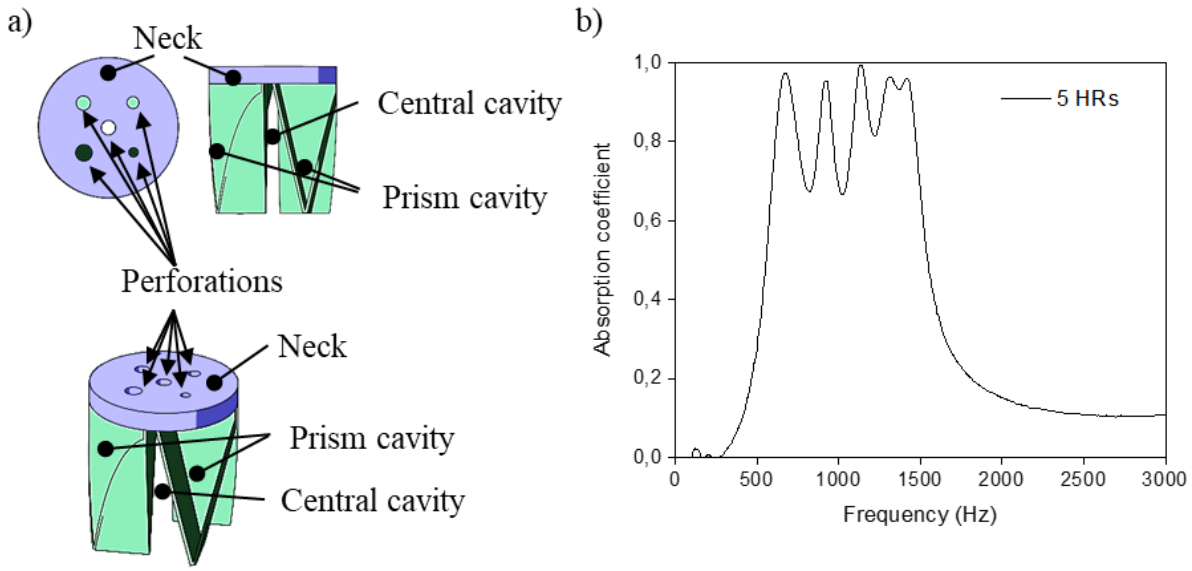

Figure 5.6 a) Top, side and isometric view of the sample for acoustic tests featuring five resonators. b) Absorption coefficient of the samples featuring five resonators with a neck thickness 3 mm and neck diameters of 2, 2.5, 3, 3 and 3.5 mm.

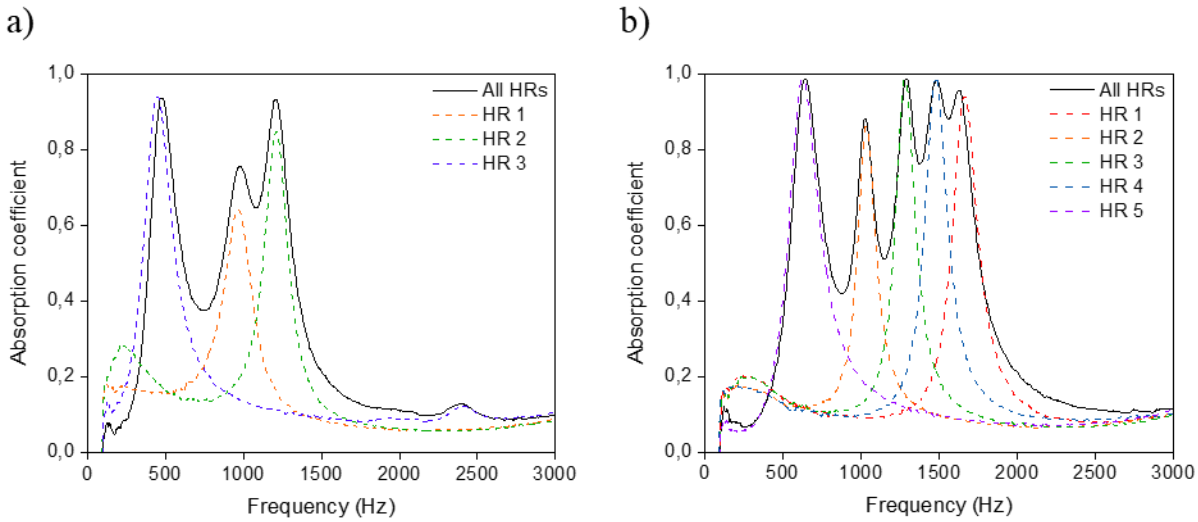

Figure 5.7 Comparison of the absorption behaviour of a sample with all the resonators acting together (solid line) and the behaviour of each single resonator of the same structure (dashed lines) of the structure with a) three resonators and b) five resonators.

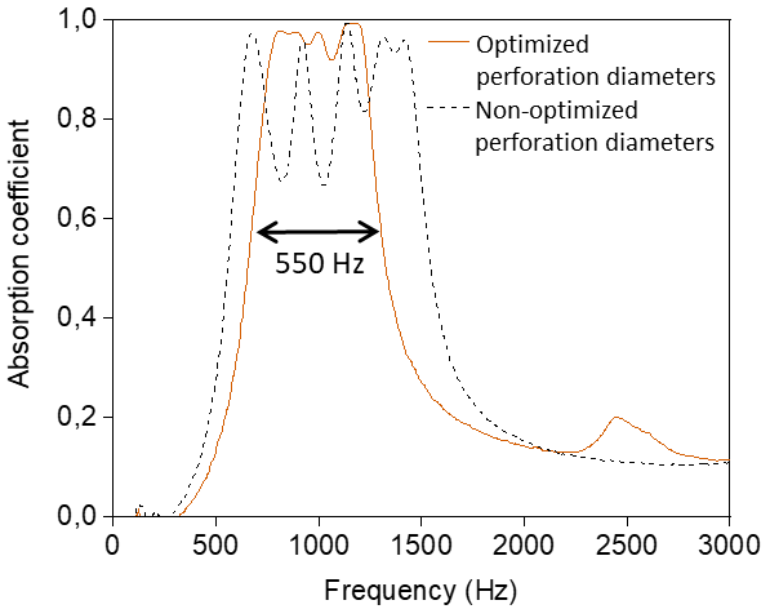

Figure 5.8 Comparison of the absorption coefficient of a geometry with optimized neck diameters and non-optimized neck diameters

5.5 Results of 3-point bending tests

Sandwich panels were 3D printed and tested under bending to asses their load-bearing mechanical properties. Firstly, tests were carried out on panels made of PLA. Then, panels made of CFR PA and CFR PA/neat PA were investigated.

5.5.1 PLA sandwich panels

Figure 5.9 shows the results of the 3-point bending tests made on PLA sandwich panels and the pictures of the panels after failure. The three and five resonators configuration were tested. The three resonators configuration showed much better mechanical performances, sustaining a load of 14 kN before failure. In addition, no detachments between skins and core was present, causing the failure of the panel because of core breakage. The absence of delamination between facesheets and core allowed the structure to withstand higher loads and a catastrophic failure. Instead, the five resonators configuration showed a peak load of 2.5 kN. Moreover, a progressive failure until the final fracture was observed. This behavior was caused by the progressive detachment between skins and core.

The huge difference in the mechanical properties has been attributed to the different contact area between core and skins of the two geometries. The structure featuring three resonators has a higher contact area, which turns into better mechanical properties. To improve the mechanical performance, fillets were added to the narrower edge of each prism of the core. Fillets were added for two main reasons: they increase the contact surface between facesheet and core and reduce stress concentrations caused by the presence of a steep angle. Figure 5.10 shows the results of the bending test and a picture of the panel with the addition of fillets. The peak load showed an increase of 43%, going from 3.5 to 5 kN. However, the results were still not as good as the one exhibited by the three resonators configuration. In addition, delamination was still the cause of the panel failure.

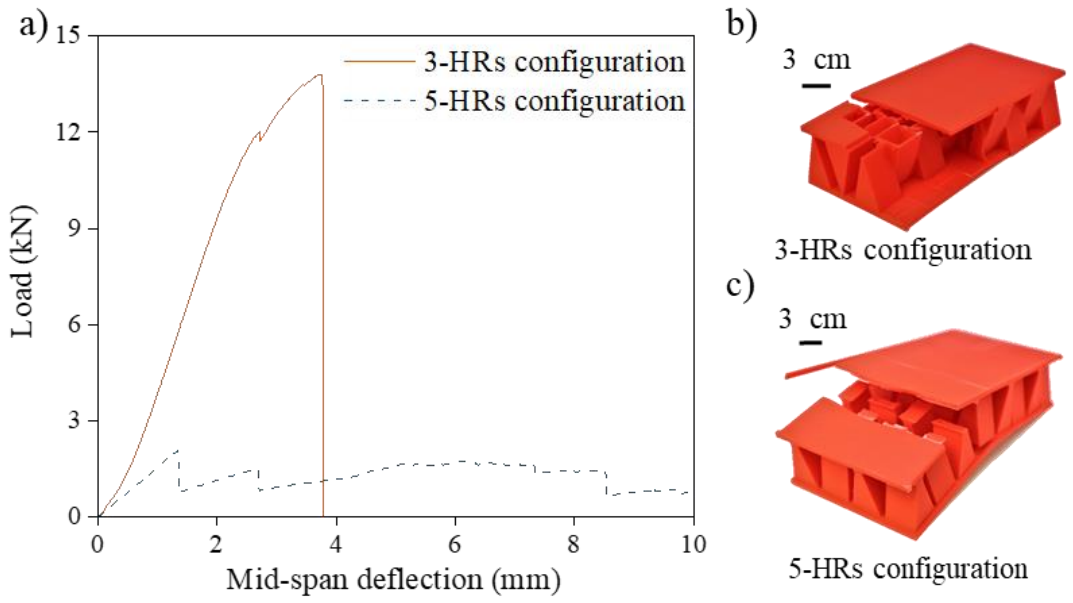

Figure 5.9 a) Result of 3-point bending test performed on sandwich panels with the three and five resonators configuration made of PLA. b) Picture of a three resonators configuration panel after failure. c) Picture of a five resonators configuration panel after failure PA sandwich panels

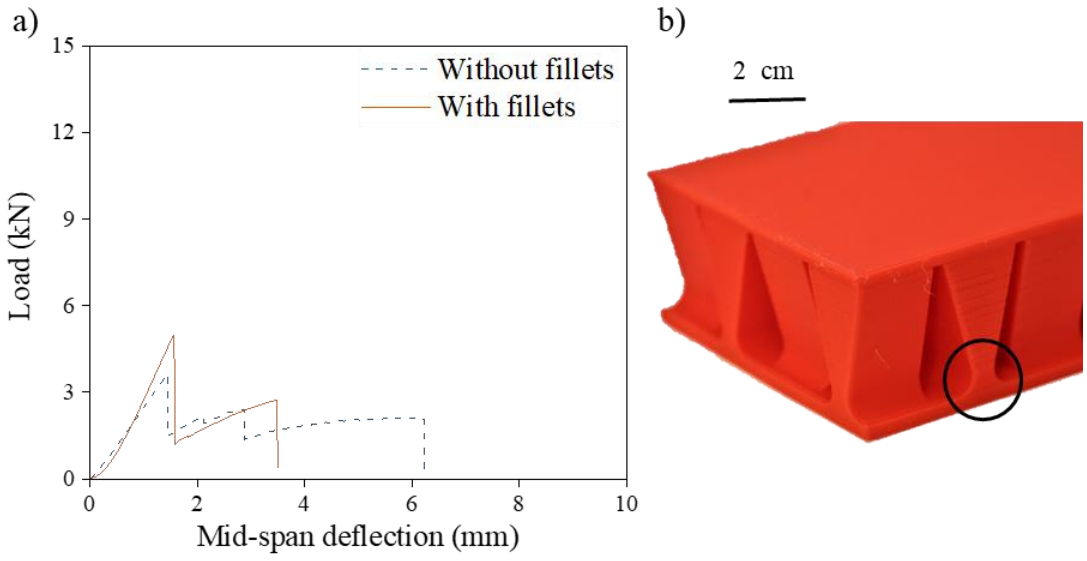

Figure 5.10 a) Result of 3-point bending test performed on sandwich panels with resonators configuration made of PLA. b) Picture of a five resonators configuration panel featuring fillets. The position of one fillet is indicated by the circle

5.5.2 PA sandwich panels

Proven the feasibility of fabricating sandwich panels and assessed their load-bearing capabilities, panels were printed with a different materials, i.e., neat and CFR PA. Figure 5.11 shows two pictures of 3D printed sandwich panels made of neat and CFR PA (i.e multi-material panel) and entirely made of CF-reinforced PA (i.e. single-material panel).

Figure 5.12a shows the results of the 3-point bending test of sandwich panels made of PA. PA sandwich panels were compared to PLA ones to evaluate the effect of the materials on the mechanical properties. The resonators configuration was used to make the comparison. The mechanical test results showed that both the CFR PA and the CFR PA/Neat PA panels have lower peak load (~2.5 kN) with respect to the PLA panels. The reason of the worst results is not fully clear, but it is probably due to either a weaker interface quality or to the presence of printing defects that weaken the structures. Figure 5.12b shows a magnified view of the results of the abovementioned 3-point bending test, highlighting the elastic regime. CFR PA/Neat PA panels had initially a better behavior, showing a higher stiffness. However, the first damage appeared soon at ~2 kN. Instead, CFR PA panels showed the worst stiffness.

Figure 5.12c and Figure 5.12d shows two pictures of the sandwich panels after failure. It is possible to observe the presence of delamination that was happening in the early stage of the test, leading to a premature failure of the panel. In addition, delamination damages were observed all along the test until the final fracture occurred, where complete delamination happened. No difference was observed between the panel made fully of CF reinforced PA and the one made of CF reinforced and neat PA.

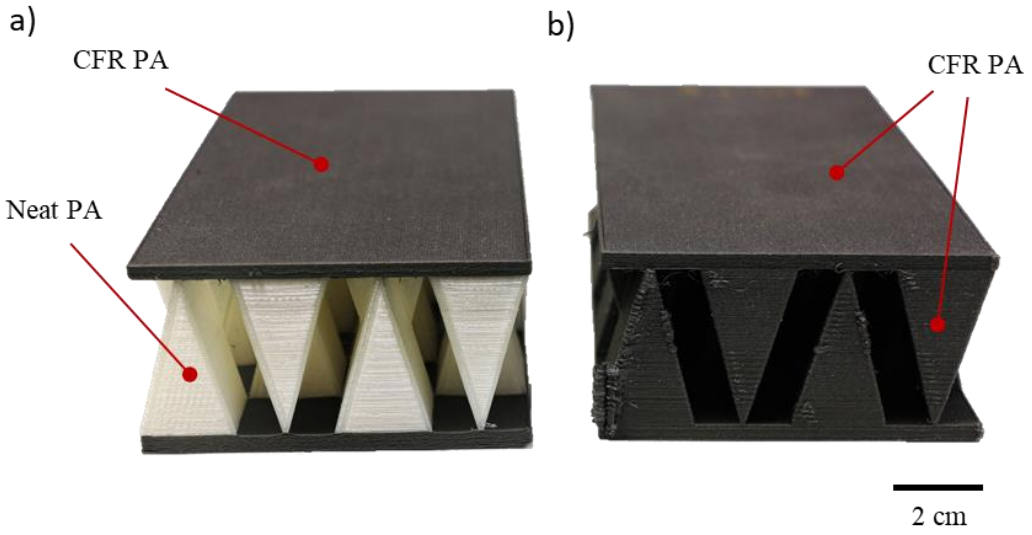

Figure 5.11 a) Picture of a sandwich panel made of CFR and neat PA. b) Picture of a sandwich panel made of CFR PA

Figure 5.13 shows the results of the 3-point bending tests made on PA panels with and without fillets. It was observed that fillets helped to improve the mechanical properties of the structures. For multi-material sandwich panels, the peak load was increased up to 6 kN, leading to an improvement of 140%. The first damage that appears is caused by the detachment between skins and core. After the structure was still able to sustain load until final failure occurred, that is caused by a combination of delamination and fracture of the core. Panels made of CFR PA also showed a huge improvement in mechanical present. The fillets produced an increase of more than three times of the peak load, passing from 2.5 to 9 kN. The better performances of the single-material sandwich panel with respect to the multi-material one is probably due to the higher stiffness of the CFR PA with respect to neat PA. In addition, the final failure was caused by the combination of core fracture and delamination. Therefore, the addition of fillets for sandwich panels made of PA had a much more pronounced effect wit h respect to the case observed with PLA panels.

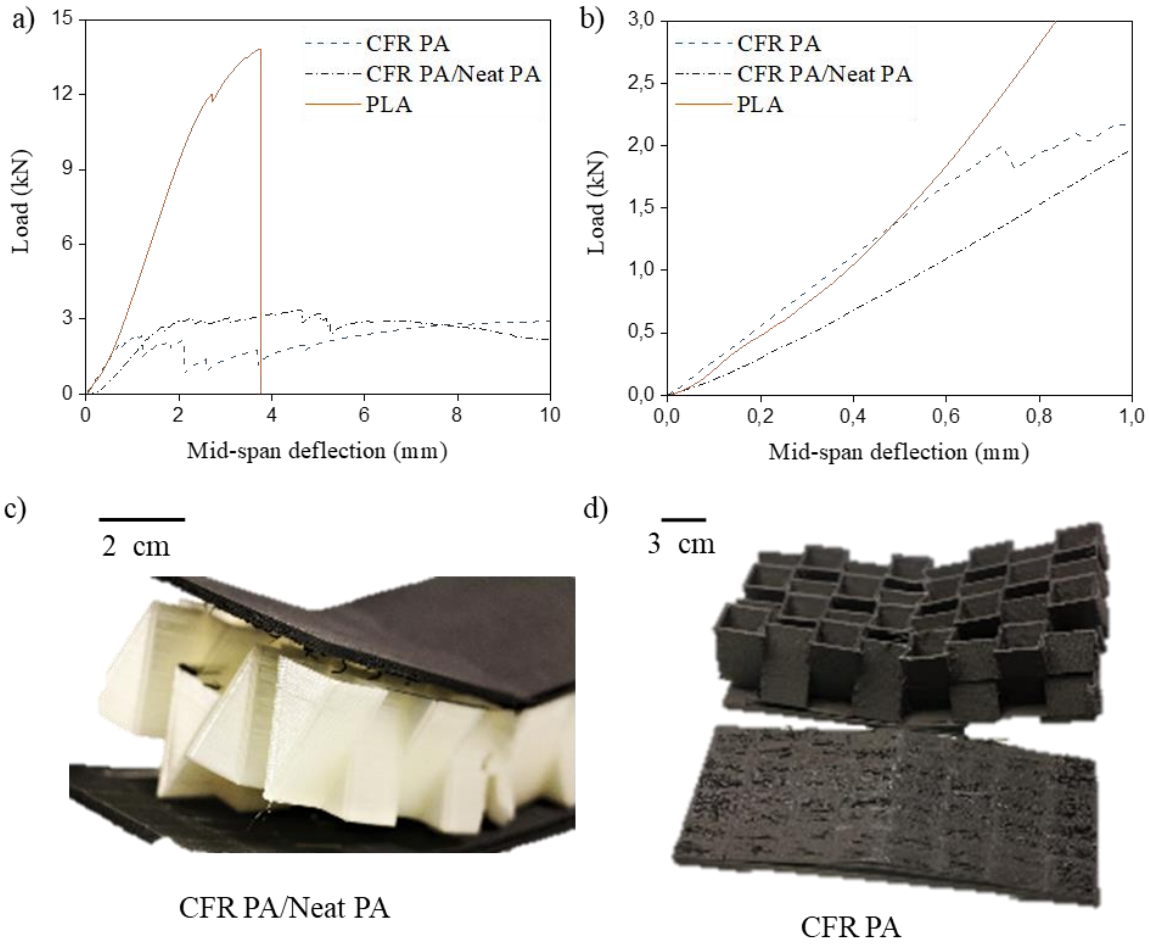

Figure 5.12 a) Result of 3-point bending test performed on sandwich panels with the three resonators configuration made of PLA, CFR PA/Neat PA and CFR PA. b) Magnified view of the results of of the 3-point bending test performed on sandwich panels with the three resonators configuration made of PLA, CFR PA/Neat PA and CFR PA. c) Picture of the three resonators configuration panel made of CFR PA/Neat PA after failure. d) Picture of the three resonators configuration panel made of CFR PA after failure

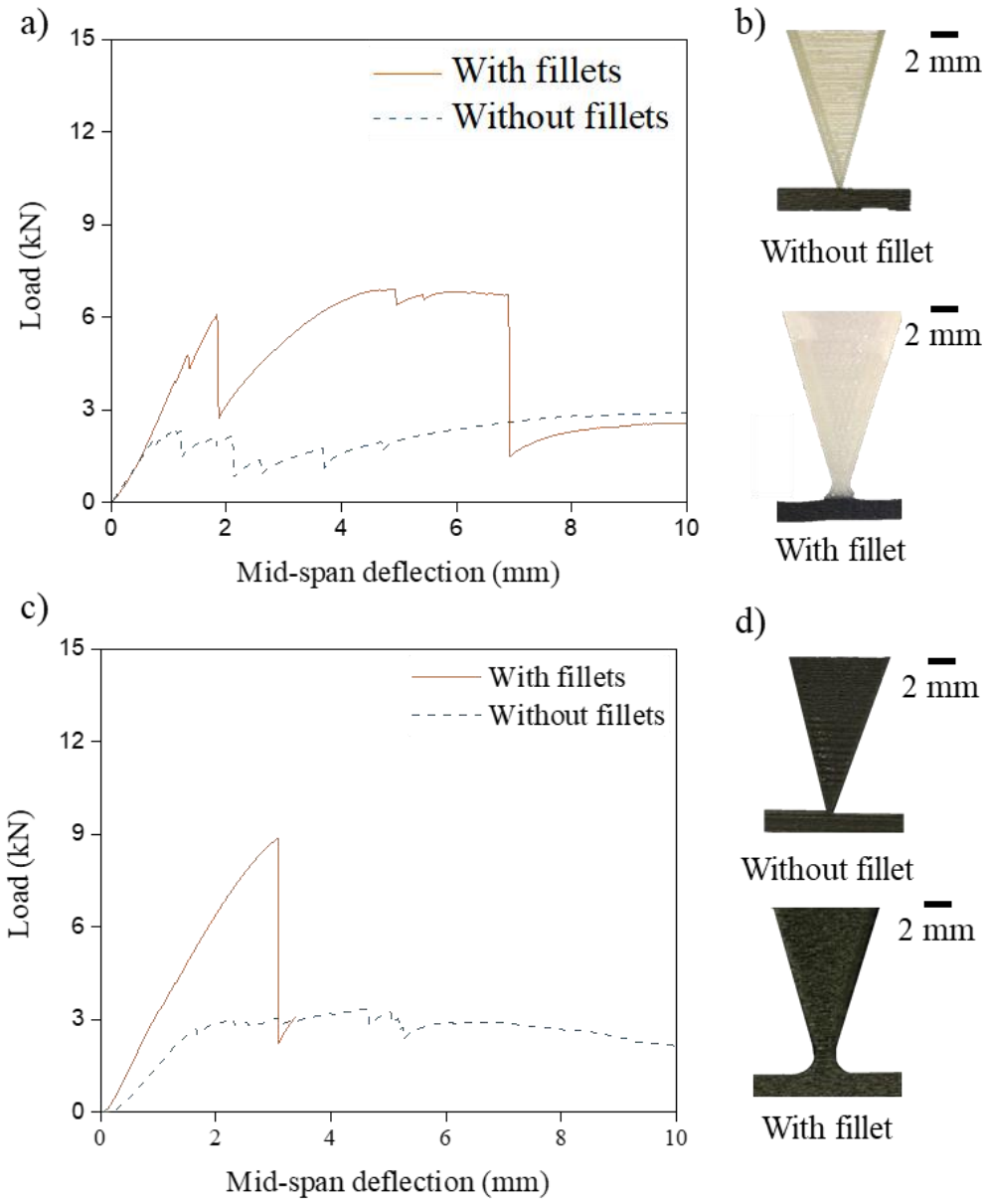

Figure 5.13 a) Result of 3-point bending test performed on sandwich panels with three resonators configuration made of CFR PA/Neat PA panels. b) Close-up images of the CFR PA/Neat PA panels showing the absence and the presence of fillets. c) Result of 3-point bending test performed on sandwich panels with three resonators configuration made of CFR PA. d) Close-up images of the CFR PA panels showing the absence and the presence of fillets.

Finally, 3-point bending tests were carried out on CFR PA sandwich panels in the presence of perorations and according to ASTM C393 standard [140]. Figure 5.14a shows a picture of the 3D printed sandwich panel. The span length suggested by the standard is 15 cm, therefore the length of the panels was increased from 16.4 cm to 22 cm. Having regard to the very high printing time required for the panels, i.e. ~35h, only one configuration was tested. It was chosen the five resonators configuration since it is much more interesting from the acoustic point of view. For the same reason, the neck diameters were the same as the optimized five resonators acoustic sample, since it is the configuration having the best acoustic properties. Three panels with these features were tested to evaluate the repeatability of the test. Figure 5.14b shows the result of the mechanical tests. Sample #1 and #3 showed similar results, both having the peak load at ~3kN. Sample #2 showed a slightly lower peak load, probably due to the presence of printing defects. A direct comparison with the tests performed on PA smaller panels cannot be done, since the used span length for the test was different. Figure 5.14c shows two pictures of the core of the panel taken during the test. It is possible to notice that the peak load corresponded to the appearance of the delamination damages, highlighted by the arrows. The detachment between skins and core was present despite the presents of fillets. As it was stated in Section 5.5.1, the severe delamination strongly affects the mechanical performance of structures, lowering the maximum load the panel would be able to with stand.

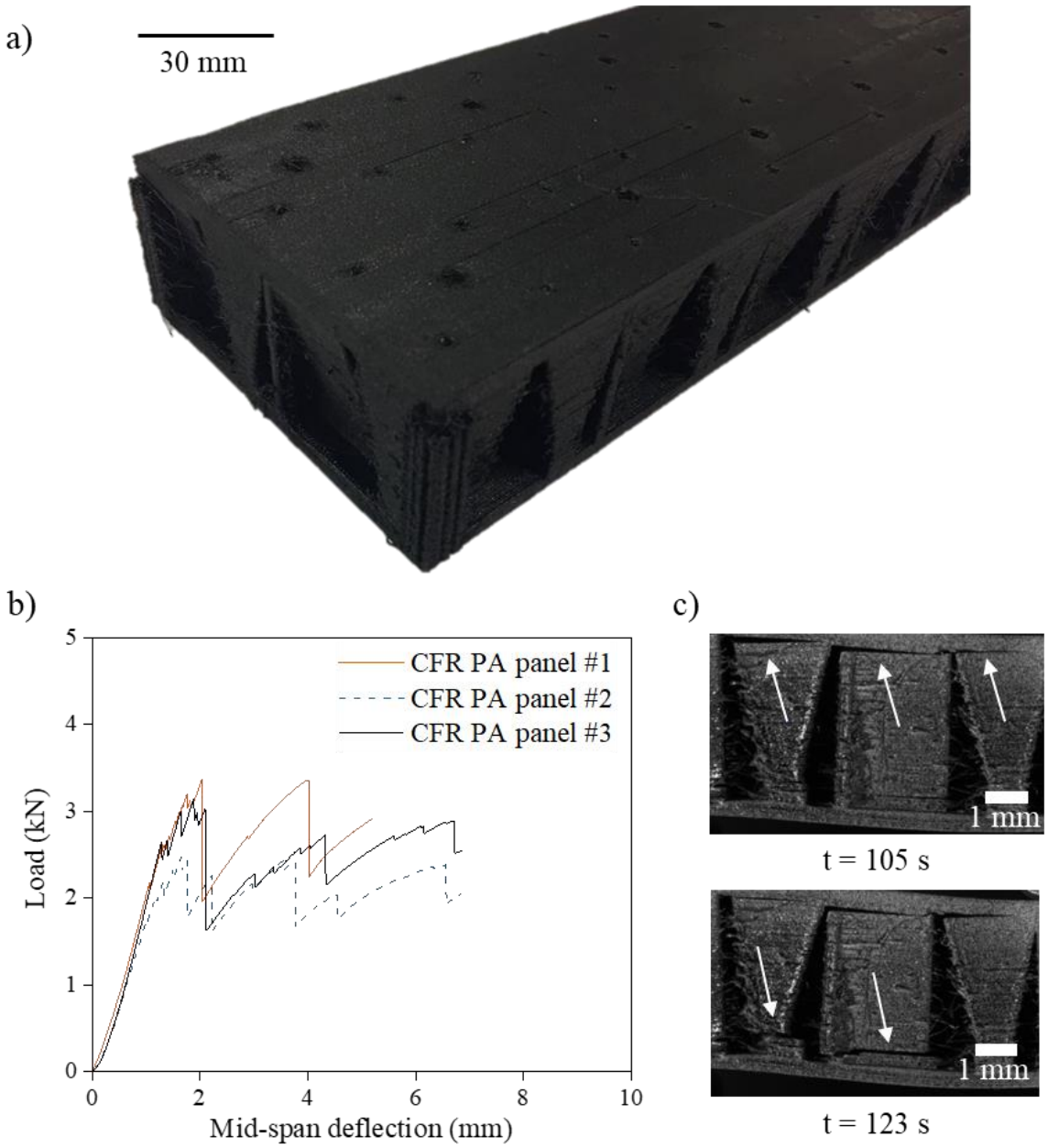

Figure 5.14 a) Picture of the five resonators sandwich panel configuration made of CFR PA. b) Result of 3-point bending test performed on sandwich panels with a bigger length (22cm). c) Time-lapse of the flexion test showing the appearance of delamination damages.

5.6 Chapter conclusion

Unit cells featuring multiple resonators were developed to provide sound absorption starting at relatively low frequencies. A summary of the impedance tube test results is presented in Table 5.3. Helmholtz resonators were chosen due to the possibility of targeting the absorbed frequency changing the geometric parameters of the resonator. In addition, the Helmholtz resonators were easily adapted to the core of the sandwich panels: the cavities of the resonators were the core of the panel, while the neck was the top facesheet.

Multiple Helmholtz resonators, featuring three and five resonators were manufactured. Each structure showed multiple absorption peaks. Both the three resonators and the five resonators structure showed absorption starting at relatively low frequencies. Therefore, these two geometries were selected as the most promising and used for the development of the sandwich panels.

Moreover, it was showed that each absorption peak of a sample with all the resonators acting together corresponded to the peak of a single resonator of the same sample acting alone. Therefore, it is possible to modify the geometric features of each Helmholtz resonator to target specific frequencies or to achieve unitary absorption over the desired frequency range. As an example, an optimization of the aperture diameters was performed. Absorption always higher than 90% was obtained for the rage of frequency 700-1200 HZ.

Table 5.3 Summary of the results of the impedance tube tests

Number of Helmholtz resonators	**Lowest absorbed frequency (Hz)**	**Absorbed frequency range (Hz)**	**Average absorption coefficient**
1	500	-	-
3	450	800	0.64
5	600	900	0.85
5 (optimized)	700	550	0.95

The fabrication with FDM of single and multi-material sandwich panels was shown. Single-material panels were fabricated with PLA and CFR PA, while multi-material panels with CFR PA for the facesheets and neat PA for the core. Firstly, 3-point bending tests were performed with a short span length to evaluate the quality of the interface between skins and core.

PLA samples featuring the three resonators and five resonators configurations were tested and compared. The three resonators configuration showed a much higher peak load and delamination between facesheets and core was not present. The five resonators had a much lower peak load and the delamination between the facesheets and the core was the cause of the final failure. The difference is probably due to the higher contact surface between skins and core of the three resonators configuration. Therefore, the addition of fillets helped to improve mechanical properties.

Then, sample made of PA were tested. Both single and multi-material PA panel had worse mechanical properties than PLA panels, which is probably due to the lower interfacial strength of PA with respect to PLA or due to the presence of printing defects. The addition of fillets caused a huge increase in the mechanical properties of both samples, especially for the CFR nylon sample, which had an improvement of more than three times. However, delamination damages were still present, even if the final failure was a combination of delamination and core fracture. Additional tests were performed on CFR PA sample using a higher span length (i.e. 150 mm). During the tests, the panels exhibited sever delamination damages, meaning that the geometry of the core should be still optimized to improve mechanical performances.

CHAPTER 6 CONCLUSION AND RECOMMANDATIONS

The project proposed HTRT composite materials featuring improved mechanical and thermal properties and suitable for FDM 3D printing. PEEK, PEI and PEEK/PEI polymer matrices were mixed with CFs and 3D printed to obtain thin filaments and Type IV dogbone specimens. The use of PEEK/PEI blends enabled a higher T_g with respect to PEEK to reach higher maximum service temperatures. Our microscopic images of the HTRT composite filaments showed a good distribution of the CFs inside the polymer matrix. In addition, the SEM images showed a good wetting between the matrix and the CFs. However, the presence of air bubbles inside the extruded and 3D printed filaments was detected. The HTRT composite filament that showed the highest Young's modulus was PEEK/CF 40wt.% (i.e. 20.1 GPa). Concerning 3D printed dogbone specimens, PEEK/PEI (80wt.%/20wt.%)/CF 30wt.% had the highest stiffness, featuring a modulus of 16.6 GPa. The feasibility of manufacturing by FDM sandwich panels for both acoustic and structural applications was also proved in this project. An unit cell containing five resonators that features almost unitary absorption over 550 Hz (i.e., 700 to 1050 Hz) was developed. In addition, 3-point bending test highlighted that delamination between facesheets and core has been found as the principal cause of failure, reducing the peak load of the structures. Improvements of the developed geometries were made with the goal to increase the peak load, through the addition of fillets to the core geometry.

However, some results presented in this thesis had some limitations or were not fully explained, requiring additional investigations. The use of the PEEK/PEI (80wt.%/20wt.%) as polymer matrix seemed to have improved the printability of the material, however quantitative data supporting these results are not available. Other limitations/issues that need to be addressed are: (i) defects such as air bubbles and interfaces in 3D printed part were present, lowering the mechanical properties of the material, (ii) a in-depth study of the crystallinity of the HTRT composites was not performed, (iii) the creation of the unit cells was limited by the dimensions of the impedance tube test (i.e. 30 mm), and (iv) our additively manufactured first generation of sandwich panels showed some limitations in the mechanical performances. Therefore, the followings are our recommendations:

- The printability of the HTRT composite materials should be comprehensively studied. Additionally, rheology tests allow to obtain information on the viscosity and, consequently, the flow of the materials during the printing process.
- A further investigation of both the mixing procedure and the FDM printing parameters should be performed to reduce or avoid the presence of voids inside the materials, by finding the possible sources, and the presence of an interface between adjacent printed layers.
- Consideration on the service temperature of the material were made base only on the T_g of the material. However, the presence of a crystalline phase is important because it retains the mechanical properties above T_g. Therefore, a study on the effect of degree of crystallinity on the mechanical properties of the material at high temperature should be carried out.
- The use of an impedance tube with a larger diameter (>30 mm) would allow the creation of acoustic samples with more than five Helmholtz resonators and, therefore, a sound absorption over a wider range of frequencies.
- An in-depth study on the effect of different types of materials on the interface quality between the factsheets and the core of the developed sandwich panels should be performed.

Future developments of the work presented in this project involves the characterization of the mechanical properties of the developed HTRT at elevated temperatures (>100°C). Characterization techniques such as Dynamic Mechanical Analysis (DMA) and Heat Deflection Temperature (HDT) may help determining the maximum service temperature at which these materials can be used, while tensile test in a heated environmental chamber could provide more precise measurements of the exact mechanical properties at these temperatures. Concerning the sandwich panels, a simulation tool able to predict the mechanical performances of the structure could help the optimization phase of the creation of the acoustic concepts and reduce the number of tests to perform. Finally, panels made of the developed HTRT composites could be 3D printed, creating a multi-functional component able to absorb sounds over a wide range of frequencies, withstand mechanical loads and resist to high temperatures and to harsh environments.

REFERENCES

[1] P. Argüelles and P. Busquin, “A Vision for 2020: Meeting Society’s Needs and Winning Global Leadership,” European Commission, 2001.

[2] Europäische Kommission and Europäische Kommission, Eds., *Flightpath 2050: Europe’s vision for aviation ; maintaining global leadership and serving society’s needs ; report of the High-Level Group on Aviation Research*. Luxembourg: Publ. Off. of the Europ. Union, 2011.

[3] “AERO - Boeing 787 from the Ground Up.” [Online]. Available: https://www.boeing.com/commercial/aeromagazine/articles/qtr_4_06/article_04_2.html. [Accessed: 26-Apr-2019].

[4] “A350 XWB Family,” *Airbus*. [Online]. Available: https://www.airbus.com/aircraft/passenger-aircraft/a350xwb-family.html. [Accessed: 26-Apr-2019].

[5] “LEAP,” *Safran Aircraft Engines*, 01-Jun-2015. [Online]. Available: https://www.safran-aircraft-engines.com/commercial-engines/single-aisle-commercial-jets/leap/leap. [Accessed: 26-Apr-2019].

[6] L. J. Kumar and C. K. Nair, “Current trends of additive manufacturing in the aerospace industry,” in *Advances in 3D Printing & Additive Manufacturing Technologies*, Springer, 2017, pp. 39–54.

[7] T. S. Srivatsan, K. Manigandan, and T. S. Sudarshan, “Additive Manufacturing of Materials: Viable Techniques, Metals, Advances, Advantages, and Applications,” *Addit. Manuf.*, pp. 1–48, 2015.

[8] A. Bandyopadhyay, T. Gualtieri, and S. Bose, “Global engineering and additive manufacturing,” *Addit. Manuf.*, vol. 1, 2015.

[9] R. D. Farahani, M. Dubé, and D. Therriault, “Three-Dimensional Printing of Multifunctional Nanocomposites: Manufacturing Techniques and Applications,” *Adv. Mater.*, vol. 28, no. 28, pp. 5794–5821, Jul. 2016.

[10] “Standard Terminology for Additive Manufacturing – General Principles – Terminology,” 15.

[11] R. Vaidyanathan, “Additive Manufacturing Technologies for Polymers and Composites,” *Addit. Manuf.*, pp. 19–64, 2015.

[12] W. L. Kempton, “A Design Sociotechnical Making of 3D Printing.” Pan Stanford Publishing, 2017.

[13] B.-J. de Gans, P. C. Duineveld, and U. S. Schubert, “Inkjet Printing of Polymers: State of the Art and Future Developments,” *Adv. Mater.*, vol. 16, no. 3, pp. 203–213, 2004.

[14] X. Xu, S. Meteyer, N. Perry, and Y. F. Zhao, “Energy consumption model of Binder-jetting additive manufacturing processes,” *Int. J. Prod. Res.*, vol. 53, no. 23, pp. 7005–7015, Dec. 2015.

[15] D. Therriault, R. F. Shepherd, S. R. White, and J. A. Lewis, “Fugitive Inks for Direct-Write Assembly of Three-Dimensional Microvascular Networks,” *Adv. Mater.*, vol. 17, no. 4, pp. 395–399, 2005.

[16] D. Therriault, S. R. White, and J. A. Lewis, “Chaotic mixing in three-dimensional microvascular networks fabricated by direct-write assembly,” *Nat. Mater.*, vol. 2, no. 4, p. 265, Apr. 2003.

[17] “The Power of Direct Writing | Science.” [Online]. Available: https://science.sciencemag.org/content/289/5481/879. [Accessed: 05-May-2019].

[18] R. L. Truby and J. A. Lewis, “Printing soft matter in three dimensions,” *Nature*, vol. 540, no. 7633, pp. 371–378, Dec. 2016.

[19] B. Bhushan and M. Caspers, “An overview of additive manufacturing (3D printing) for microfabrication,” *Microsyst. Technol.*, vol. 23, no. 4, pp. 1117–1124, Apr. 2017.

[20] K. S. Boparai, R. Singh, and J. S. Chohan, “Fused Deposition Modelling: Applications and Advancements,” in *Additive Manufacturing*, CRC Press, 2018, pp. 127–186.

[21] S. S. Crump, “Apparatus and method for creating three-dimensional objects,” US5121329A, 09-Jun-1992.

[22] R. D. Farahani, K. Chizari, and D. Therriault, “Three-dimensional printing of freeform helical microstructures: a review,” *Nanoscale*, vol. 6, no. 18, pp. 10470–10485, 2014.

[23] R. D. Farahani, D. Therriault, M. Dubé, S. Bodkhe, and M. Mahdavi, “6.13 Additive Manufacturing of Multifunctional Nanocomposites and Composites,” in *Comprehensive Composite Materials II*, P. W. R. Beaumont and C. H. Zweben, Eds. Oxford: Elsevier, 2018, pp. 380–407.

[24] M. Shojib Hossain, D. Espalin, J. Ramos, M. Perez, and R. Wicker, “Improved Mechanical Properties of Fused Deposition Modeling-Manufactured Parts Through Build Parameter Modifications,” *J. Manuf. Sci. Eng.*, vol. 136, no. 6, pp. 061002-061002–12, Oct. 2014.

[25] D. Popescu, A. Zapciu, C. Amza, F. Baciu, and R. Marinescu, “FDM process parameters influence over the mechanical properties of polymer specimens: A review,” *Polym. Test.*, vol. 69, pp. 157–166, Aug. 2018.

[26] J. S. Chohan and R. Singh, “Pre and post processing techniques to improve surface characteristics of FDM parts: a state of art review and future applications,” *Rapid Prototyp. J.*, vol. 23, no. 3, pp. 495–513, Mar. 2017.

[27] A. K. Sood, R. K. Ohdar, and S. S. Mahapatra, “Parametric appraisal of mechanical property of fused deposition modelling processed parts,” *Mater. Des.*, vol. 31, no. 1, pp. 287–295, Jan. 2010.

[28] B. V. Reddy, N. V. Reddy, and A. Ghosh, “Fused deposition modelling using direct extrusion,” *Virtual Phys. Prototyp.*, vol. 2, no. 1, pp. 51–60, Mar. 2007.

[29] D. Odell, P. K. Wright, M. Montero, S. Roundy, and S. Ahn, “Anisotropic material properties of fused deposition modeling ABS,” *Rapid Prototyp. J.*, vol. 8, no. 4, pp. 248–257, Oct. 2002.

[30] J. E. Renaud, J. F. Rodriguez, and J. P. Thomas, “Characterization of the mesostructure of fused-deposition acrylonitrile-butadiene-styrene materials,” *Rapid Prototyp. J.*, vol. 6, no. 3, pp. 175–186, Sep. 2000.

[31] T.-M. Wang, J.-T. Xi, and Y. Jin, “A model research for prototype warp deformation in the FDM process,” *Int. J. Adv. Manuf. Technol.*, vol. 33, no. 11, pp. 1087–1096, Aug. 2007.

[32] “List of High Temperature Plastic: Uses, Structure & Material Guide.” [Online]. Available: https://omnexus.specialchem.com/selection-guide/high-temperature-thermoplastics. [Accessed: 10-May-2019].

[33] L. A. Utracki, “2 - Characterization methods for high temperature polymer blends,” in *High Temperature Polymer Blends*, M. T. DeMeuse, Ed. Woodhead Publishing, 2014, pp. 14–69.

[34] P. M. Hergenrother, “The use, design, synthesis, and properties of high performance/high temperature polymers: an overview,” *High Perform. Polym.*, vol. 15, no. 1, pp. 3–45, 2003.

[35] N. A. B. Nordin, M. A. B. Johar, M. H. I. B. Ibrahim, and O. M. F. bin Marwah, “Advances in High Temperature Materials for Additive Manufacturing,” *IOP Conf. Ser. Mater. Sci. Eng.*, vol. 226, p. 012176, Aug. 2017.

[36] X. Wang, M. Jiang, Z. Zhou, J. Gou, and D. Hui, “3D printing of polymer matrix composites: A review and prospective,” *Compos. Part B Eng.*, vol. 110, pp. 442–458, 2017.

[37] M. Dosière, *Crystallization of Polymers*. Springer Netherlands, 2012.

[38] A. B. Strong, *Fundamentals of Composites Manufacturing, Second Edition: Materials, Methods and Applications*. Society of Manufacturing Engineers, 2008.

[39] R. V. Hoffman, *Organic Chemistry: An Intermediate Text*. Wiley, 2004.

[40] G. Pertici, “2 - The effect of molecular structure on the properties of biomedical polymers,” in *Durability and Reliability of Medical Polymers*, M. Jenkins and A. Stamboulis, Eds. Woodhead Publishing, 2012, pp. 30–48.

[41] S. J. Grunewald, “Stratasys Custom Creates New ESD PEKK 3D Printing Material for Use in Space,” *3DPrint.com | The Voice of 3D Printing / Additive Manufacturing*, 08-Feb-2016. .

[42] S. Xiaoyong, C. Liangcheng, M. Honglin, G. Peng, B. Zhanwei, and L. Cheng, “Experimental analysis of high temperature PEEK materials on 3D printing test,” presented at the 9th International Conference on Measuring Technology and Mechatronics Automation, ICMTMA 2017, January 14, 2017 - January 15, 2017, 2017, pp. 13–16.

[43] W. Wu, P. Geng, G. Li, D. Zhao, H. Zhang, and J. Zhao, “Influence of layer thickness and raster angle on the mechanical properties of 3D-printed PEEK and a comparative mechanical study between PEEK and ABS,” *Materials*, vol. 8, no. 9, pp. 5834–5846, 2015.

[44] K. M. Rahman, T. Letcher, and R. Reese, “Mechanical properties of additively manufactured peek components using fused filament fabrication,” presented at the ASME 2015 International Mechanical Engineering Congress and Exposition, IMECE 2015, November 13, 2015 - November 19, 2015, 2015, vol. 2A-2015, p. American Society of Mechanical Engineers (ASME).

[45] A. M. Díez-Pascual and A. L. Díez-Vicente, “Nano-TiO2 Reinforced PEEK/PEI Blends as Biomaterials for Load-Bearing Implant Applications,” *ACS Appl. Mater. Interfaces*, vol. 7, no. 9, pp. 5561–5573, 2015.

[46] W. Z. Wu, P. Geng, J. Zhao, Y. Zhang, D. W. Rosen, and H. B. Zhang, “Manufacture and thermal deformation analysis of semicrystalline polymer polyether ether ketone by 3D printing,” *Mater. Res. Innov.*, vol. 18, pp. S5-12-S5-16, 2014.

[47] P. Wang, B. Zou, H. Xiao, S. Ding, and C. Huang, “Effects of printing parameters of fused deposition modeling on mechanical properties, surface quality, and microstructure of PEEK,” *J. Mater. Process. Technol.*, vol. 271, pp. 62–74, Sep. 2019.

[48] C. Yang, X. Tian, D. Li, Y. Cao, F. Zhao, and C. Shi, “Influence of thermal processing conditions in 3D printing on the crystallinity and mechanical properties of PEEK material,” *J. Mater. Process. Technol.*, vol. 248, pp. 1–7, 2017.

[49] X. Deng, Z. Zeng, B. Peng, S. Yan, and W. Ke, “Mechanical Properties Optimization of Poly-Ether-Ether-Ketone via Fused Deposition Modeling,” *Mater. Basel*, vol. 11, no. 2, Jan. 2018.

[50] T. Liu, Y. Tong, and W.-D. Zhang, “Preparation and characterization of carbon nanotube/polyetherimide nanocomposite films,” *Compos. Sci. Technol.*, vol. 67, no. 3, pp. 406–412, 2007.

[51] R. O. Johnson and H. S. Burlhis, “Polyetherimide: A new high-performance thermoplastic resin,” *J. Polym. Sci. Polym. Symp.*, vol. 70, no. 1, pp. 129–143, 1983.

[52] K. C. Chuang, J. E. Grady, R. D. Draper, E.-S. E. Shin, C. Patterson, and T. D. Santelle, “Additive manufacturing and characterization of ultem polymers and composites,” presented at the 2nd Annual Composites and Advanced Materials Expo, CAMX 2015, October 26, 2015 - October 29, 2015, 2015, pp. 448–463.

[53] H. Wu, M. Sulkis, J. Driver, A. Saade-Castillo, A. Thompson, and J. H. Koo, “Multi-functional ULTEM^{TM}1010 composite filaments for additive manufacturing using Fused Filament Fabrication (FFF),” *Addit. Manuf.*, vol. 24, pp. 298–306, Dec. 2018.

[54] G. Cicala *et al.*, “Comparison of Ultem 9085 used in fused deposition modelling (FDM) with polytherimide blends,” *Materials*, vol. 11, no. 2, 2018.

[55] J. M. Spikowski, E. R. Harrell, and S.-W. Wang, “Fatigue performance of fused deposition modeling style 3D printed vs. injection molded ultem 9085,” presented at the 73rd Annual Technical Conference and Exhibition of the Society of Plastics Engineers, SPE ANTEC Orlando 2015, March 23, 2015 - March 25, 2015, 2015, pp. 809–816.

[56] G. Taylor, S. Anandan, D. Murphy, M. Leu, and K. Chandrashekhara, “Fracture toughness of additively manufactured ULTEM 1010,” *Virtual Phys. Prototyp.*, vol. 14, no. 3, pp. 277–283, Jul. 2019.

[57] G. Taylor *et al.*, “Flexural behavior of additively manufactured Ultem 1010: experiment and simulation,” *Rapid Prototyp. J.*, vol. 24, no. 6, pp. 1003–1011, Aug. 2018.

[58] A. Bagsik and V. Schoppner, “Mechanical properties of fused deposition modeling parts manufactured with Ultem*9085,” presented at the 69th Annual Technical Conference of the

Society of Plastics Engineers 2011, ANTEC 2011, May 1, 2011 - May 5, 2011, 2011, vol. 2, pp. 1294–1298.

[59] "NASA Technical Reports Server (NTRS) - High Temperature Thermoplastic Additive Manufacturing Using Low-Cost, Open-Source Hardware." [Online]. Available: https://ntrs.nasa.gov/search.jsp?R=20170000214. [Accessed: 15-May-2019].

[60] M. T. Demeuse, "1 - Introduction to high temperature polymer blends," in *High Temperature Polymer Blends*, M. T. DeMeuse, Ed. Woodhead Publishing, 2014, pp. 1–13.

[61] R. Ramani and S. Alam, "Composition optimization of PEEK/PEI blend using model-free kinetics analysis," *Thermochim. Acta*, vol. 511, no. 1–2, pp. 179–188, 2010.

[62] T. G. Fox, "Influence of Diluent and of Copolymer Composition on the Glass Temperature of a Poly-mer System," *Bull Am Phys Soc*, vol. 1, p. 123, 1956.

[63] H. S. Lee and W. N. Kim, "Glass transition temperatures and rigid amorphous fraction of poly (ether ether ketone) and poly (ether imide) blends," *Polymer*, vol. 38, no. 11, pp. 2657–2663, 1997.

[64] M. Shibata, Z. Fang, and R. Yosomiya, "Miscibility and crystallization behavior of poly (ether ether ketone ketone)/poly (ether imide) blends," *J. Appl. Polym. Sci.*, vol. 80, no. 5, pp. 769–775, 2001.

[65] "DSC - A beginner's guide," *https://www.perkinelmer.com/lab-solutions/resources/docs/GDE_DSCBeginnersGuide.pdf*. .

[66] S. D. Hudson, D. D. Davis, and A. J. Lovinger, "Semicrystalline morphology of poly (aryl ether ether ketone)/poly (ether imide) blends," *Macromolecules*, vol. 25, no. 6, pp. 1759–1765, 1992.

[67] M. K. Ostberg Gunilla and C. Seferis James, "Annealing effects on the crystallinity of polyetheretherketone (PEEK) and its carbon fiber composite," *J. Appl. Polym. Sci.*, vol. 33, no. 1, pp. 29–39, Apr. 2018.

[68] J. Sandler, P. Werner, M. S. P. Shaffer, V. Demchuk, V. Altstädt, and A. H. Windle, "Carbon-nanofibre-reinforced poly(ether ether ketone) composites," *Compos. Part Appl. Sci. Manuf.*, vol. 33, no. 8, pp. 1033–1039, 2002.

[69] J. Hanchi and N. S. Eiss, "Dry sliding friction and wear of short carbon-fiber-reinforced polyetheretherketone (PEEK) at elevated temperatures," *Wear*, vol. 203–204, pp. 380–386, 1997.

[70] A. Saleem, L. Frormann, and A. Iqbal, "High performance thermoplastic composites: Study on the mechanical, thermal, and electrical resistivity properties of carbon fiber-reinforced polyetheretherketone and polyethersulphone," *Polym. Compos.*, vol. 28, no. 6, pp. 785–796, Apr. 2018.

[71] T. Q. Li, M. Q. Zhang, and H. M. Zeng, "Processing dependent morphology, interfacial interaction and shear behavior of short carbon fiber reinforced PEEK," *Compos. Part Appl. Sci. Manuf.*, vol. 32, no. 12, pp. 1727–1733, 2001.

[72] G. Xian and Z. Zhang, “Sliding wear of polyetherimide matrix composites: I. Influence of short carbon fibre reinforcement,” *Wear*, vol. 258, no. 5, pp. 776–782, 2005.

[73] S. Kumar *et al.*, “Study on mechanical, morphological and electrical properties of carbon nanofiber/polyetherimide composites,” *Mater. Sci. Eng. B*, vol. 141, no. 1, pp. 61–70, 2007.

[74] S. Berretta, R. Davies, Y. T. Shyng, Y. Wang, and O. Ghita, “Fused Deposition Modelling of high temperature polymers: Exploring CNT PEEK composites,” *Polym. Test.*, vol. 63, pp. 251–262, 2017.

[75] S. F. Bartolucci *et al.*, “Investigation of the Properties of PEEK-Nanotube Composites Prepared by Solution Methods,” no. 43857 C2-ASME International Mechanical Engineering Congress and Exposition, pp. 279-282 C1-Volume 12: Micro and Nano Systems, Parts A and B, 2009.

[76] A. M. Díez-Pascual, J. Guan, B. Simard, and M. A. Gómez-Fatou, “Poly(phenylene sulphide) and poly(ether ether ketone) composites reinforced with single-walled carbon nanotube buckypaper: II – Mechanical properties, electrical and thermal conductivity,” *Compos. Part Appl. Sci. Manuf.*, vol. 43, no. 6, pp. 1007–1015, 2012.

[77] D. S. Bangarusampath, H. Ruckdäschel, V. Altstädt, J. K. W. Sandler, D. Garray, and M. S. P. Shaffer, “Rheology and properties of melt-processed poly(ether ether ketone)/multi-wall carbon nanotube composites,” *Polymer*, vol. 50, no. 24, pp. 5803–5811, 2009.

[78] A. M. Díez-Pascual and M Naffakh and M A Gómez and C Marco and G Ellis and J M González-Domínguez and A Ansón and M T Martínez and Y Martínez-Rubi and B Simard and B Ashrafi, “The influence of a compatibilizer on the thermal and dynamic mechanical properties of PEEK/carbon nanotube composites,” *Nanotechnology*, vol. 20, no. 31, p. 315707, 2009.

[79] J. Chen, K. Wang, and Y. Zhao, “Enhanced interfacial interactions of carbon fiber reinforced PEEK composites by regulating PEI and graphene oxide complex sizing at the interface,” *Compos. Sci. Technol.*, vol. 154, pp. 175–186, 2018.

[80] M. C. Kuo, J. C. Huang, and M. Chen, “Non-isothermal crystallization kinetic behavior of alumina nanoparticle filled poly(ether ether ketone),” *Mater. Chem. Phys.*, vol. 99, no. 2, pp. 258–268, 2006.

[81] W. Haibin, Z. Fugui, W. Tingting, Z. Hang, L. Tao, and Y. Yanhua, “Isothermal and nonisothermal crystallization kinetics of poly(ether ether ketone)/gadolinium oxide composites,” *High Perform. Polym.*, vol. 25, no. 5, pp. 584–593, Apr. 2018.

[82] G. L. Converse, T. L. Conrad, C. H. Merrill, and R. K. Roeder, “Hydroxyapatite whisker-reinforced polyetherketoneketone bone ingrowth scaffolds,” *Acta Biomater*, vol. 6, no. 3, pp. 856–63, Mar. 2010.

[83] K. H. Tan, C. K. Chua, K. F. Leong, M. W. Naing, and C. M. Cheah, “Fabrication and characterization of three-dimensional poly(ether- ether- ketone)/-hydroxyapatite biocomposite scaffolds using laser sintering,” *Proc Inst Mech Eng H*, vol. 219, no. 3, pp. 183–94, May 2005.

[84] K. H. Tan *et al.*, “Scaffold development using selective laser sintering of polyetheretherketone–hydroxyapatite biocomposite blends,” *Biomaterials*, vol. 24, no. 18, pp. 3115–3123, Aug. 2003.

[85] M. Vaezi *et al.*, “Characterization of New PEEK/HA Composites with 3D HA Network Fabricated by Extrusion Freeforming,” *Molecules*, vol. 21, no. 6, May 2016.

[86] azonano, “Comparative Study of Carbon Nanotubes and Carbon Nanofibers,” 2011. .

[87] J. Gonçalves *et al.*, “Electrically conductive polyetheretherketone nanocomposite filaments: from production to fused deposition modeling,” *Polymers*, vol. 10, no. 8, p. 925, 2018.

[88] A. A. Stepashkin, D. I. Chukov, F. S. Senatov, A. I. Salimon, A. M. Korsunsky, and S. D. Kaloshkin, “3D-printed PEEK-carbon fiber (CF) composites: Structure and thermal properties,” *Compos. Sci. Technol.*, vol. 164, pp. 319–326, 2018.

[89] “Stratasys Additive Manufacturing Tooling Efficiency Case Study,” *Javelin 3D Solutions*, 23-Nov-2018. .

[90] J. Hiemenz, “Additive manufacturing trends in aerospace,” *Strat. Ltd*, 2014.

[91] E. Atzeni and A. Salmi, “Economics of additive manufacturing for end-usable metal parts,” *Int. J. Adv. Manuf. Technol.*, vol. 62, no. 9–12, pp. 1147–1155, Oct. 2012.

[92] A. K. Misra, J. E. Grady, and R. Carter, “Additive manufacturing of aerospace propulsion components,” 2015.

[93] D. Zhao and X. Y. Li, “A review of acoustic dampers applied to combustion chambers in aerospace industry,” *Prog. Aerosp. Sci.*, vol. 74, pp. 114–130, 2015.

[94] L. E. Kinsler, A. R. Frey, A. B. Coppens, and J. V. Sanders, “Fundamentals of acoustics,” *Fundam. Acoust. 4th Ed. Lawrence E Kinsler Austin R Frey Alan B Coppens James V Sanders Pp 560 ISBN 0-471-84789-5 Wiley-VCH Dec. 1999*, p. 560, 1999.

[95] Y. Li, X. Wang, and D. Zhang, “Control strategies for aircraft airframe noise reduction,” *Chin. J. Aeronaut.*, vol. 26, no. 2, pp. 249–260, 2013.

[96] J. M. de Bedout, M. A. Franchek, R. J. Bernhard, and L. Mongeau, “ADAPTIVE-PASSIVE NOISE CONTROL WITH SELF-TUNING HELMHOLTZ RESONATORS,” *J. Sound Vib.*, vol. 202, no. 1, pp. 109–123, Apr. 1997.

[97] F. U. Khan and Izhar, “State of the art in acoustic energy harvesting,” *J. Micromechanics Microengineering*, vol. 25, no. 2, p. 023001, Jan. 2015.

[98] M. Han, “Sound reduction by a Helmholtz resonator,” 2008.

[99] A. I. Komkin, M. A. Mironov, and A. I. Bykov, “Sound absorption by a Helmholtz resonator,” *Acoust. Phys.*, vol. 63, no. 4, pp. 385–392, Jul. 2017.

[100] A. Selamet, P. M. Radavich, N. S. Dickey, and J. M. Novak, “Circular concentric Helmholtz resonators,” *J. Acoust. Soc. Am.*, vol. 101, no. 1, pp. 41–51, 1997.

[101] N. S. Dickey and A. Selamet, “HELMHOLTZ RESONATORS: ONE-DIMENSIONAL LIMIT FOR SMALL CAVITY LENGTH-TO-DIAMETER RATIOS,” *J. Sound Vib.*, vol. 195, no. 3, pp. 512–517, Aug. 1996.

[102] M. B. Xu, A. Selamet, and H. Kim, “Dual Helmholtz resonator,” *Appl. Acoust.*, vol. 71, no. 9, pp. 822–829, 2010.

[103] S. K. Tang, C. H. Ng, and E. Y. L. Lam, “Experimental investigation of the sound absorption performance of compartmented Helmholtz resonators,” *Appl. Acoust.*, vol. 73, no. 9, pp. 969–976, 2012.

[104] D. Zhao and A. S. Morgans, “Tuned passive control of combustion instabilities using multiple Helmholtz resonators,” *J. Sound Vib.*, vol. 320, no. 4–5, pp. 744–757, 2009.

[105] C. Wang and L. Huang, “On the acoustic properties of parallel arrangement of multiple micro-perforated panel absorbers with different cavity depths,” *J. Acoust. Soc. Am.*, vol. 130, no. 1, pp. 208–218, 2011.

[106] Z. Liu, J. Zhan, M. Fard, and J. L. Davy, “Acoustic measurement of a 3D printed micro-perforated panel combined with a porous material,” *Measurement*, vol. 104, pp. 233–236, 2017.

[107] Z. Liu, J. Zhan, M. Fard, and J. L. Davy, “Acoustic properties of a porous polycarbonate material produced by additive manufacturing,” *Mater. Lett.*, vol. 181, pp. 296–299, 2016.

[108] F. Setaki, M. Tenpierik, M. Turrin, and A. van Timmeren, “Acoustic absorbers by additive manufacturing,” *Build. Environ.*, vol. 72, pp. 188–200, 2014.

[109] A. Arjunan, “Acoustic absorption of passive destructive interference cavities,” *Mater. Today Commun.*, vol. 19, pp. 68–75, Jun. 2019.

[110] E. R. Fotsing, A. Dubourg, A. Ross, and J. Mardjono, “Acoustic properties of a periodic micro-structures obtained by additive manufacturing,” *Appl. Acoust.*, vol. 148, pp. 322–331, 2019.

[111] X. Cai, Q. Guo, G. Hu, and J. Yang, “Ultrathin low-frequency sound absorbing panels based on coplanar spiral tubes or coplanar Helmholtz resonators,” *Appl. Phys. Lett.*, vol. 105, no. 12, p. 121901, Sep. 2014.

[112] C. Zhang and X. Hu, “Three-Dimensional Single-Port Labyrinthine Acoustic Metamaterial: Perfect Absorption with Large Bandwidth and Tunability,” *Phys. Rev. Appl.*, vol. 6, no. 6, p. 064025, Dec. 2016.

[113] C. R. Liu, J. H. Wu, X. Chen, and F. Ma, “A thin low-frequency broadband metasurface with multi-order sound absorption,” *J. Phys. Appl. Phys.*, vol. 52, no. 10, p. 105302, Mar. 2019.

[114] J. Grünewald, P. Parlevliet, and V. Altstädt, “Manufacturing of thermoplastic composite sandwich structures: A review of literature,” *J. Thermoplast. Compos. Mater.*, vol. 30, no. 4, pp. 437–464, 2017.

[115] V. Birman and G. A. Kardomateas, “Review of current trends in research and applications of sandwich structures,” *Compos. Part B Eng.*, vol. 142, pp. 221–240, 2018.

[116] D. Casalino, F. Diozzi, R. Sannino, and A. Paonessa, “Aircraft noise reduction technologies: a bibliographic review,” *Aerosp. Sci. Technol.*, vol. 12, no. 1, pp. 1–17, 2008.

[117] M. Toyoda, R. L. Mu, and D. Takahashi, “Relationship between Helmholtz-resonance absorption and panel-type absorption in finite flexible microperforated-panel absorbers,” *Appl. Acoust.*, vol. 71, no. 4, pp. 315–320, 2010.

[118] K. Sakagami, M. Morimoto, and M. Yairi, “A note on the relationship between the sound absorption by microperforated panels and panel/membrane-type absorbers,” *Appl. Acoust.*, vol. 70, no. 8, pp. 1131–1136, 2009.

[119] K. Sakagami, Y. Fukutani, M. Yairi, and M. Morimoto, “Sound absorption characteristics of a double-leaf structure with an MPP and a permeable membrane,” *Appl. Acoust.*, vol. 76, pp. 28–34, 2014.

[120] K. Sakagami, I. Yamashita, M. Yairi, and M. Morimoto, “Sound absorption characteristics of a honeycomb-backed microperforated panel absorber: Revised theory and experimental validation,” *Noise Control Eng. J.*, vol. 58, no. 2, pp. 157–162, 2010.

[121] Y. Tang, F. Li, F. Xin, and T. J. Lu, “Heterogeneously perforated honeycomb-corrugation hybrid sandwich panel as sound absorber,” *Mater. Des.*, vol. 134, pp. 502–512, 2017.

[122] H. Meng, M.-A. Galland, M. Ichchou, O. Bareille, F. X. Xin, and T. J. Lu, “Small perforations in corrugated sandwich panel significantly enhance low frequency sound absorption and transmission loss,” *Compos. Struct.*, vol. 182, pp. 1–11, 2017.

[123] W. W. Lin, M. M. Martinez, R. K. Majjigi, D. P. Calder, and A. Goldsholl, “Continuous degree of freedom acoustic cores,” US20180218723A1, 02-Aug-2018.

[124] X. Peng, J. Ji, and Y. Jing, “Composite honeycomb metasurface panel for broadband sound absorption,” *J. Acoust. Soc. Am.*, vol. 144, no. 4, pp. EL255–EL261, Oct. 2018.

[125] I. M. Daniel and J. L. Abot, “Fabrication, testing and analysis of composite sandwich beams,” *Compos. Sci. Technol.*, vol. 60, no. 12–13, pp. 2455–2463, 2000.

[126] T. N. Bitzer, *Honeycomb technology: materials, design, manufacturing, applications and testing*. Springer Science & Business Media, 2012.

[127] H. Y. Sarvestani, A. H. Akbarzadeh, H. Niknam, and K. Hermenean, “3D printed Architected Polymeric Sandwich Panels: Energy Absorption and Structural Performance,” *Compos. Struct.*, 2018.

[128] H. Y. Sarvestani, A. H. Akbarzadeh, A. Mirbolghasemi, and K. Hermenean, “3D printed meta-sandwich structures: Failure mechanism, energy absorption and multi-hit capability,” *Mater. Des.*, vol. 160, pp. 179–193, 2018.

[129] A. Bagsik, S. Josupeit, V. Schoeppner, and E. Klemp, “Mechanical analysis of lightweight constructions manufactured with fused deposition modeling,” presented at the 29th International Conference of the Polymer Processing Society, PPS 2013, July 15, 2013 - July 19, 2013, 2014, vol. 1593, pp. 696–701.

[130] D. Pollard, C. Ward, G. Herrmann, and J. Etches, “The manufacture of honeycomb cores using Fused Deposition Modeling,” *Adv. Manuf. Polym. Compos. Sci.*, vol. 3, no. 1, pp. 21–31, 2017.

[131] T. Li and L. Wang, “Bending behavior of sandwich composite structures with tunable 3D-printed core materials,” *Compos. Struct.*, vol. 175, pp. 46–57, 2017.

[132] L. C. Thomas, “Modulated DSC® Paper# 1 Why Modulated DSC®?; An Overview and Summary of Advantages and Disadvantages Relative to Traditional DSC,” *TA Instrum. Technol Pap*, 2005.

[133] “Standard Test Method for Tensile Properties of Single Textile Fibers,” 2014.

[134] Standard ASTM, “D638-14 Standard Test Method for Tensile Properties of Plastics; ASTM International: West Conshohocken, PA, 2014.”

[135] “ZOLTEK PX 35 Carbon Fiber | ZOLTEK.” [Online]. Available: https://zoltek.com/products/px35/. [Accessed: 25-Jun-2019].

[136] Hérard, Chloé, “LES EFFETS DE LA TEMPÉRATURE LORS DE LA FABRICATION ADDITIVE PAR FDM DE COMPOSITES THERMOPLASTIQUES RENFORCÉS ET LEURS PROPRIÉTÉS MÉCANIQUES,” Polytechnique Montréal, Montréal, Canada, 2017.

[137] ASTM, “ASTM E1050-12 Standard Test Method for Impedance and Absorption of Acoustical Materials Using a Tube, Two Microphones and a Digital Frequency Analysis System,” 2012.

[138] M. R. Stinson, “The propagation of plane sound waves in narrow and wide circular tubes, and generalization to uniform tubes of arbitrary cross-sectional shape,” *J. Acoust. Soc. Am.*, vol. 89, no. 2, pp. 550–558, Feb. 1991.

[139] J. A. Nelder and R. Mead, “A Simplex Method for Function Minimization,” *Comput. J.*, vol. 7, no. 4, pp. 308–313, Jan. 1965.

[140] ASTM, “Standard Test Method for Core Shear Properties of Sandwich Constructions by Beam Flexure,” 2016.

[141] “PEEK KetaSpire® Solvay KT-880 Flakes.” [Online]. Available: http://catalog.ides.com/datasheet.aspx?I=42041&FMT=PDF&E=96636. [Accessed: 15-Jul-2019].

[142] “Victrex PEEK 381G.” [Online]. Available: https://www.victrex.com/~/media/datasheets/victrex_tds_381g.pdf. [Accessed: 15-Jul-2019].

[143] “Victrex PEEK 90G.” [Online]. Available: https://www.victrex.com/~/media/datasheets/victrex_tds_90g.pdf. [Accessed: 15-Jul-2019].

[144] “Ultem Resin 1010.” [Online]. Available: https://pc-api-public.sabic.com/uploads/d37169ab/ca55/e711/80fb/005056857ef3/ULTEM%E2%84%A2%20%20Resin_1010_Europe_Technical_Data_Sheet.pdf. [Accessed: 15-Jul-2019].

[145] “ZOLTEK PX 30 Carbon Fiber | ZOLTEK.” [Online]. Available: https://zoltek.com/products/px30/. [Accessed: 22-Jul-2019].

[146] “Pitch-based Carbon Fiber(CF) ‘DIALEAD’ | Products,” *Mitsubishi Chemical Corporation*. [Online]. Available: https://www.m-chemical.co.jp/en/products/departments/mcc/cfcm/product/1201229_7502.html. [Accessed: 22-Jul-2019].

[147] “Pitch Fiber,” *Mitsubishi Chemical Carbon Fiber Composites*. [Online]. Available: http://mccfc.com/pitch-fiber/. [Accessed: 22-Jul-2019].

[148] “HexTow Chopped Carbon Fiber | Hexcel.” [Online]. Available: https://www.hexcel.com/Products/Carbon-Fiber/HexTow-Chopped-Carbon-Fiber?ljs=en. [Accessed: 22-Jul-2019].

[149] I. Oterno Navas, “Processing of Carbon Fiber Reinforced High Temperature Resistance Thermoplastics for 3D Printing Applications,” Polytechnique Montréal, Sep. 2018.

APPENDIX A SUMMARY OF THE PROPERTY OF THE USED POLYMERS AND CFS

Table A.1 Summary of properties of polymers used in this project

Polymer	Tensile Modulus	Tensile Strength	Reference
PEEK KetaSpire® Solvay KT-880 Flakes	3700 MPa (ASTM D638)	100 MPa (ASTM D638)	[141]
PEEK Victrex® 381G	4000 MPa (ISO527)	98 MPa (ISO527)	[142]
PEEK Victrex® 90G	4100 MPa (ISO527)	105 MPa (ISO527)	[143]
PEI ULTEM® 1010	3200 MPa (ISO527)	105 MPa (ISO527)	[144]

Table A.2 Summary of the properties of as received CFs used in this project

Type	Carbon Content	Diameter	Length	Sizing Content	Reference
PANEX PX30 Milled	99 %	7.2 μm	100-150 μm	0.0 %	[145]
PANEX PX35 Chopped Type 83	95 %	7.2 μm	6 mm	1.5 % %	[135]
K223HM Milled	99 %	11 μm	50-200	0.0 %	[146]
K223HM Chopped	99 %	11 μm	6 mm	1-3 %	[147]
Hextow sizing 1925	N/A	N/A	6.4 mm	3-7 %	[148]

APPENDIX B ANALYSIS OF AS RECEIVED CFS

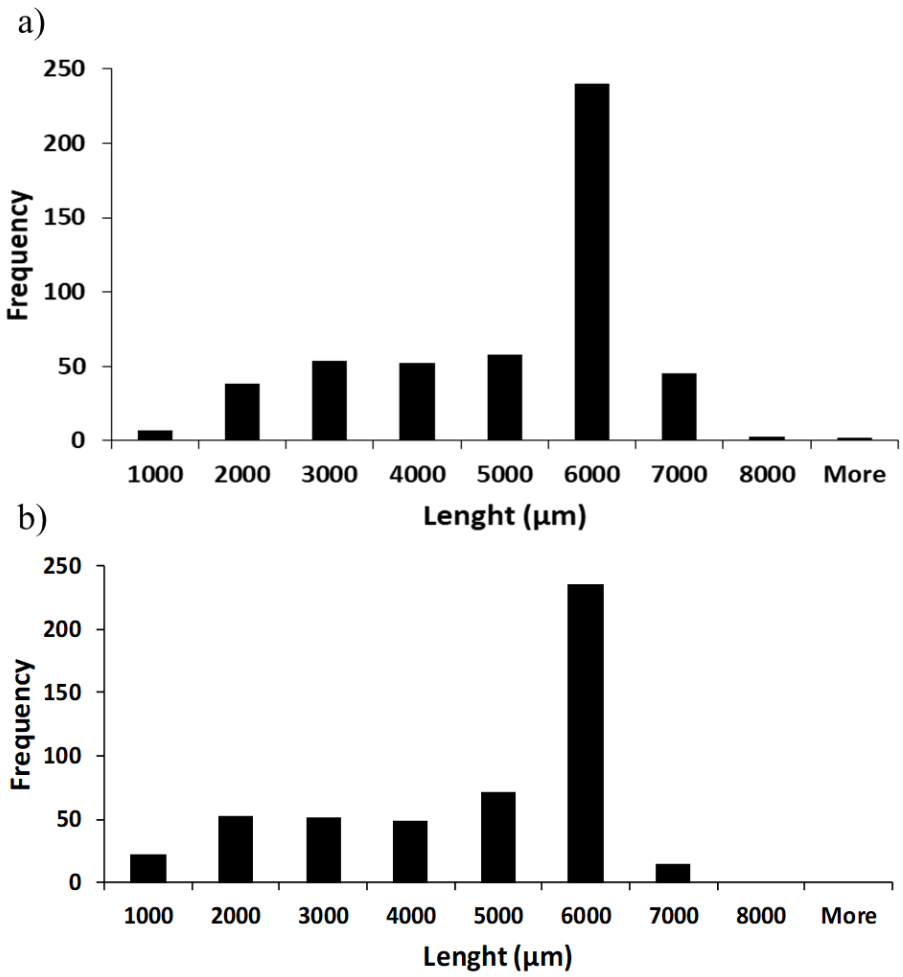

Figure B.1 Length distribution of a) Zoltek CFs and b) Mitsubishi CFs [149]

APPENDIX C DSC RESULTS ON PEEK AND PEEK/CF

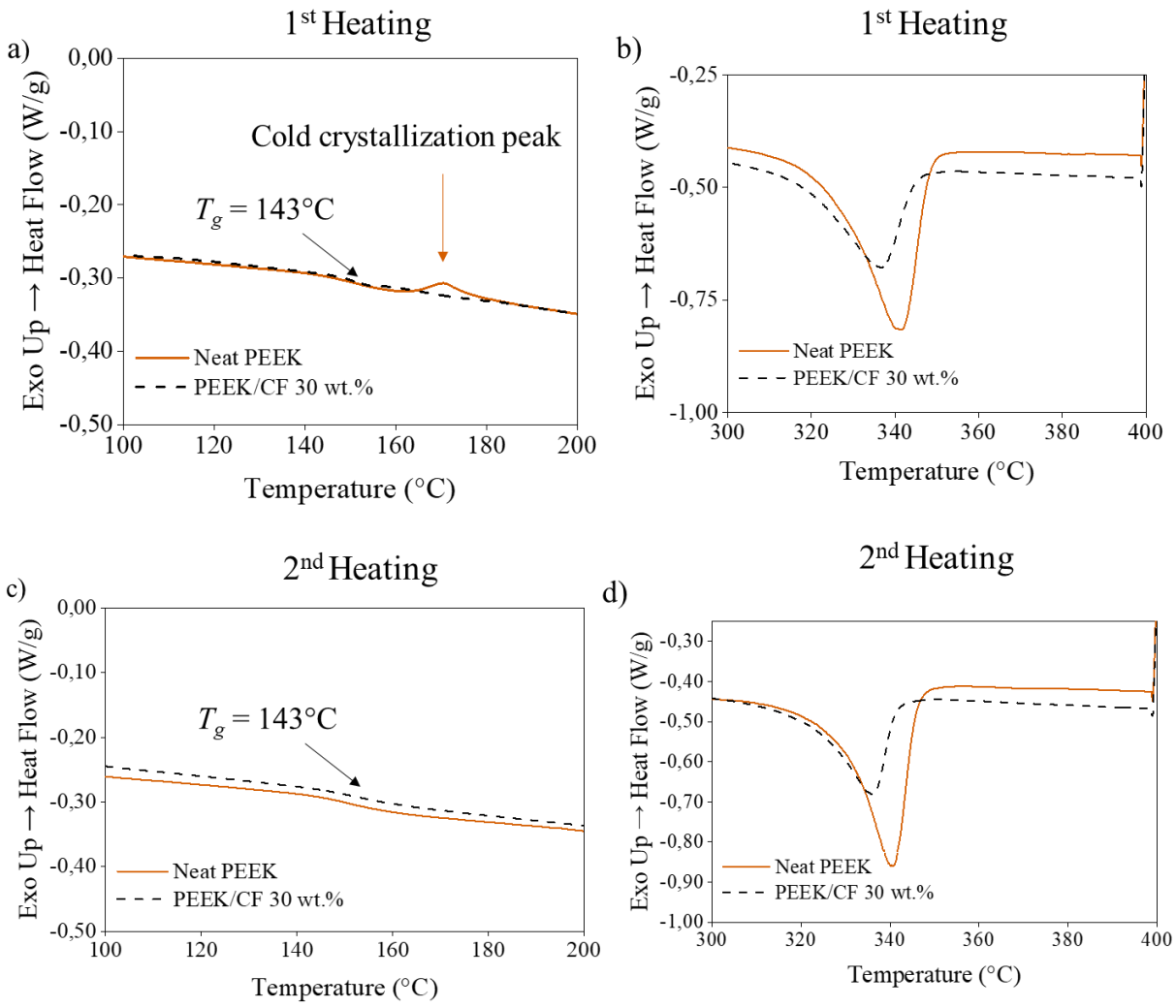

Figure C.1 a) DSC thermograms between 100 and 200°C of the 1st heating of neat PEEK and PEEK/CFs 30wt.%. b) DSC thermograms between 300 and 400°C of the 1st heating of neat PEEK and PEEK/CFs 30wt.%. c) DSC thermograms between 100 and 200°C of the 2nd heating of neat PEEK and PEEK/CFs 30wt.%. d) DSC thermograms between 300 and 400°C of the 2nd heating of neat PEEK and PEEK/CFs 30wt.%. The location of the T_g is highlighted.

Table C.1 Summary of the DSC results on PEEK and PEEK /CF 30wt.%

Material	**Cycle**	T_m **(°C)**	T_c **(°C)**	T_g **(°C)**	χ_c **(%)**
Neat PEEK	1st heating	340	N/A	143	35
	1st cooling	N/A	292	N/A	N/A
	2nd heating	340	N/A	143	35
PEEK/CFs 30wt.%	1st heating	336	N/A	143	22
	1st cooling	N/A	287	N/A	N/A
	2nd heating	336	N/A	143	19

APPENDIX D DSC RESULTS ON PEI AND PEI/CF

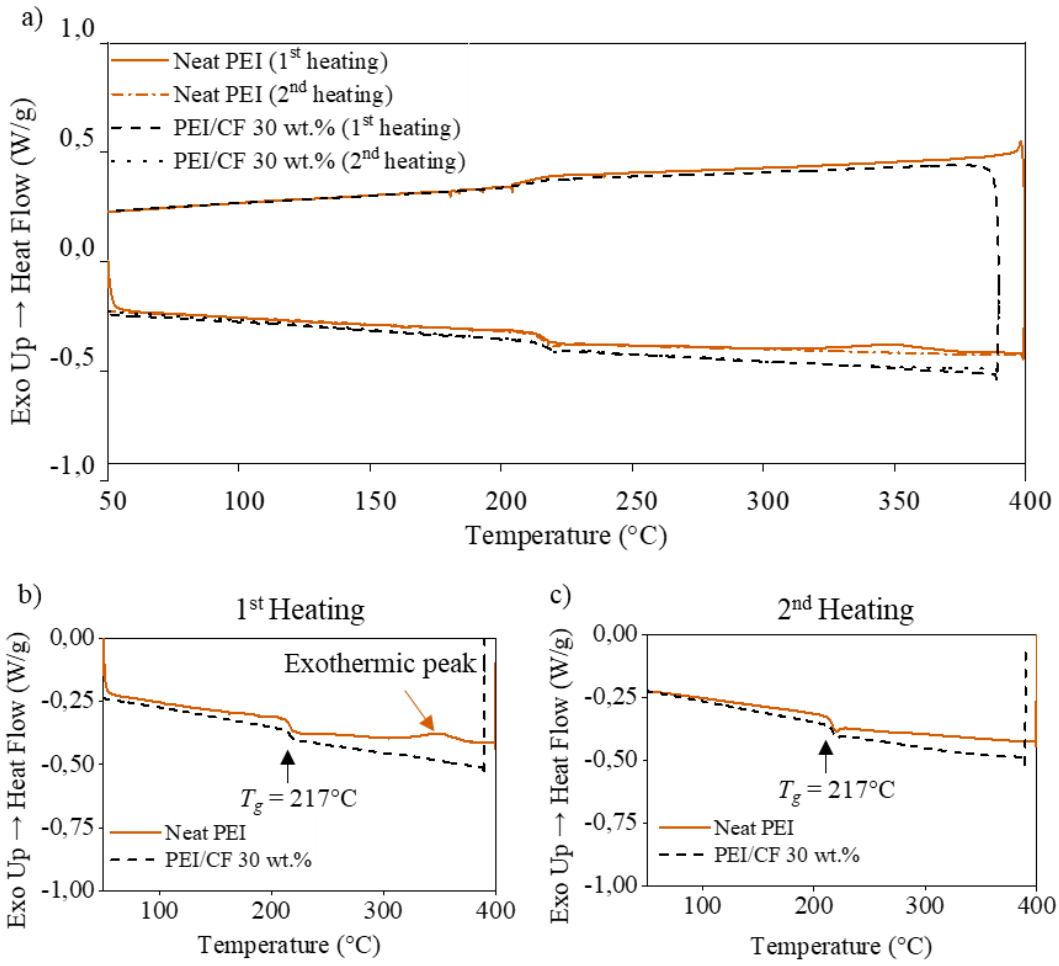

Figure D.1 a) DSC thermograms between 50 and 400°C of neat PEI vs PEI/ CFs 30wt.%. b) Detailed view of the 1st heating between 50 and 400°C. The locations of the T_g and the exothermic peak are highlighted. c) Detailed view of the 2st heating between 50 and 400°C. The location of the T_g is highlighted.

APPENDIX E TGA RESULTS OF CFS REINFORCED COMPOSITES

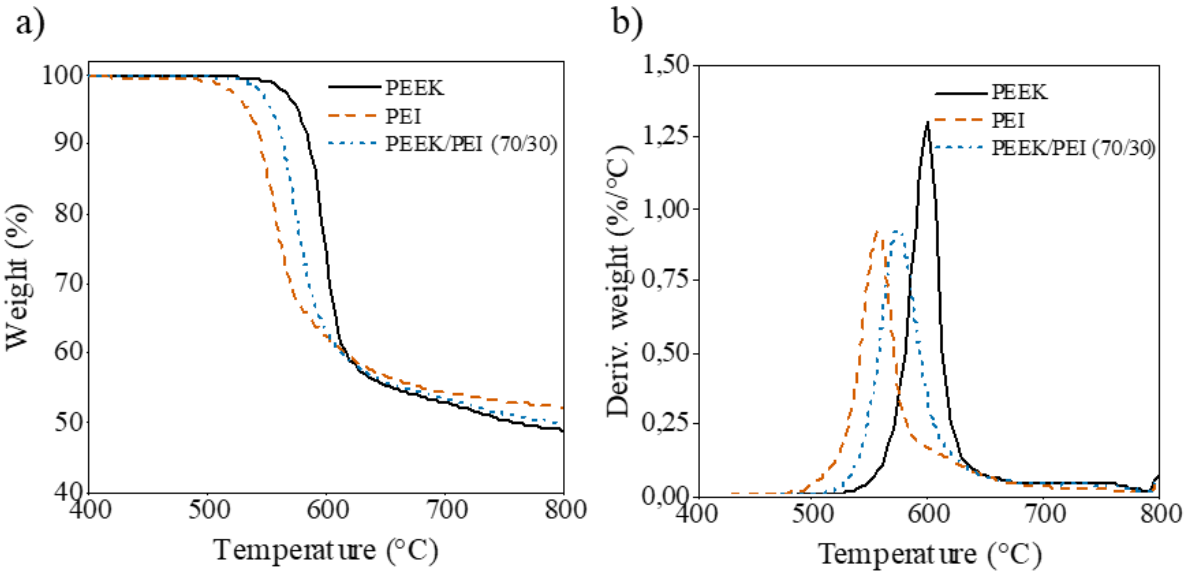

Figure E.1 Weight loss evolution (a) and derivative of weight loss (b) with respect to temperature for neat PEEK, PEI and PEEK/PEI (70wt.%/30wt.%)

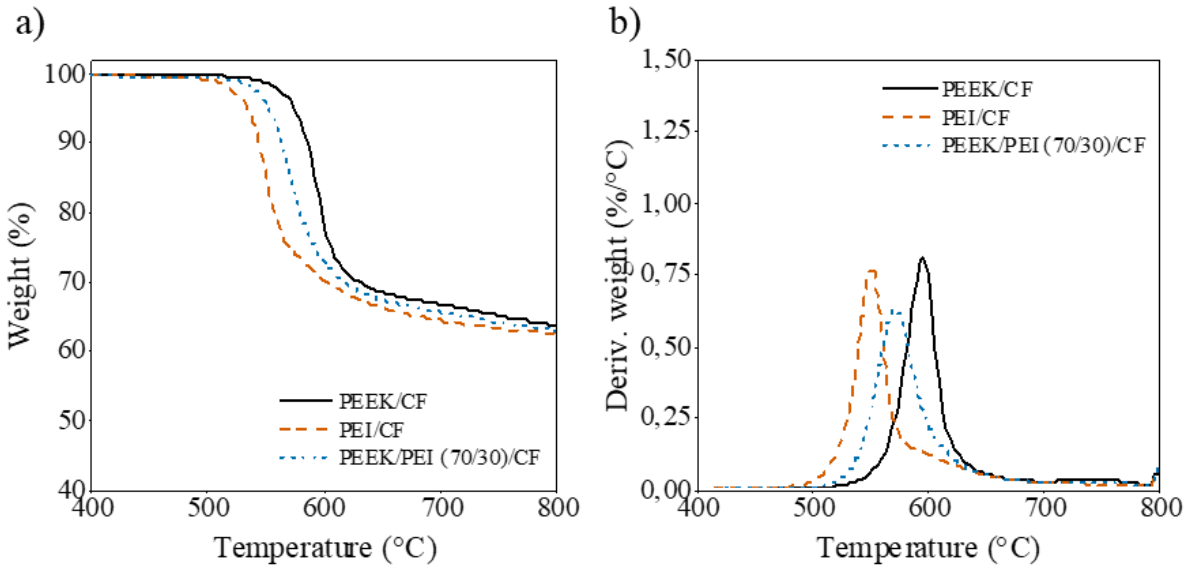

Figure E.2 Weight loss evolution (a) and derivative of weight loss (b) with respect to temperature for PEEK, PEI and PEEK/PEI (70wt.%/30wt.%) reinforced with 30wt.% of CFs

Table E.1 TGA results of neat and 30wt.% CF reinforced PEEK, PEI and PEEK/PEI (70wt.%/30wt.%)

Polymer matrix	**Type of material**	**Onset of Degradation (°C)**	**Maximum Degradation Rate (°C)**
PEI	Neat polymer	535	557
	Composite	532	550
PEEK	Neat polymer	580	599
	Composite	574	595
PEEK/PEI (70wt.%/30wt.%)	Neat polymer	552	574
	Composite	547	568

APPENDIX F EFFECT OF DIFFERENT TYPE OF POLYMER MATRIX ON THE YOUNG'S MODULUS OF HTRT FILAMENTS

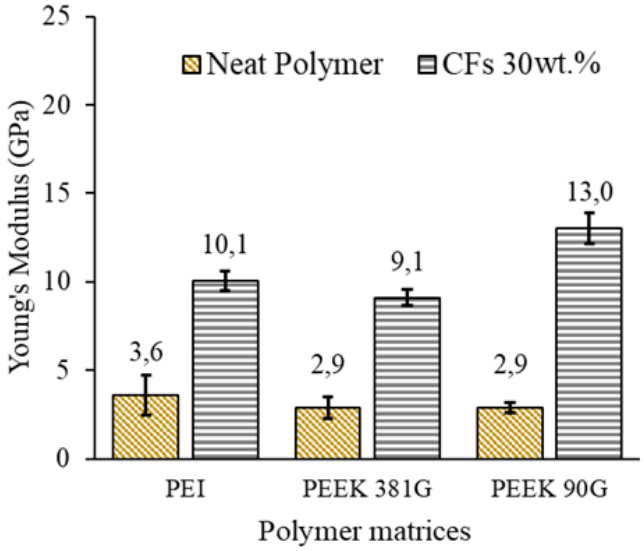

Figure F.1 Young's modulus of neat and CF reinforced PEI Ultem 1010, PEEK 381G and PEEK 90G

APPENDIX G MECHANICAL PROPERTIES OF HTRT FILAMENTS EXTRUDED WITH THE BÜHLER AND BRABENDER EXTRUDERS

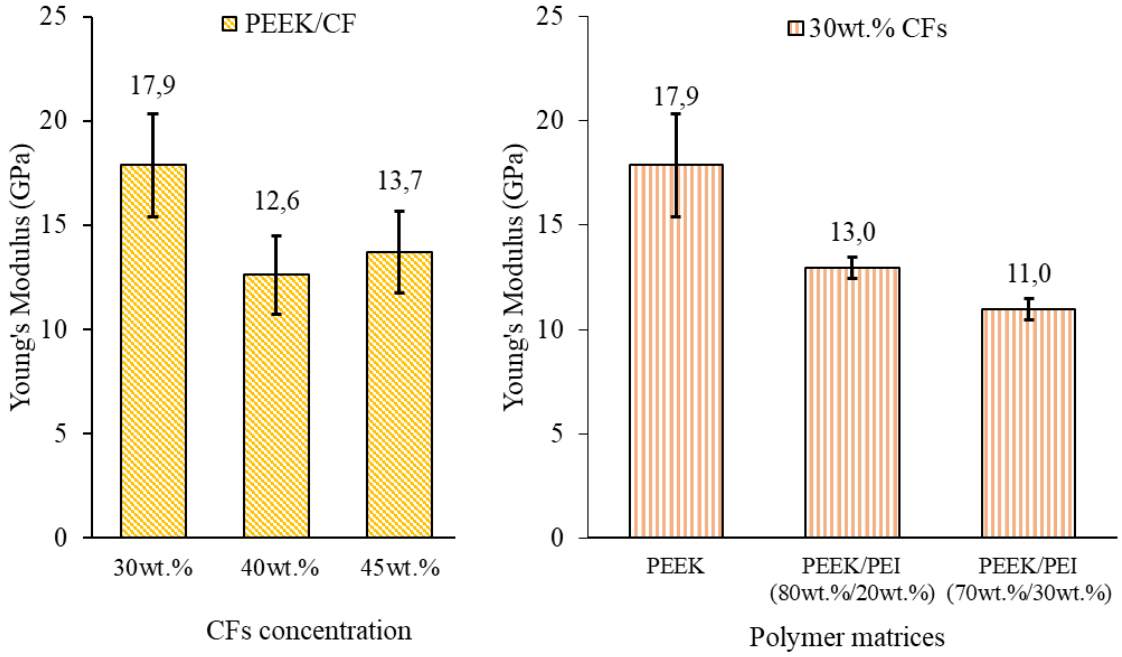

Figure G.1 a) Young's modulus of PEEK/CF composite filaments with different concentrations of CFs mixed with the Bülher and Brabender extruders. b) Young's modulus of 30wt.% composite filaments with different polymer matrices mixed with the Bülher and Brabender extruders

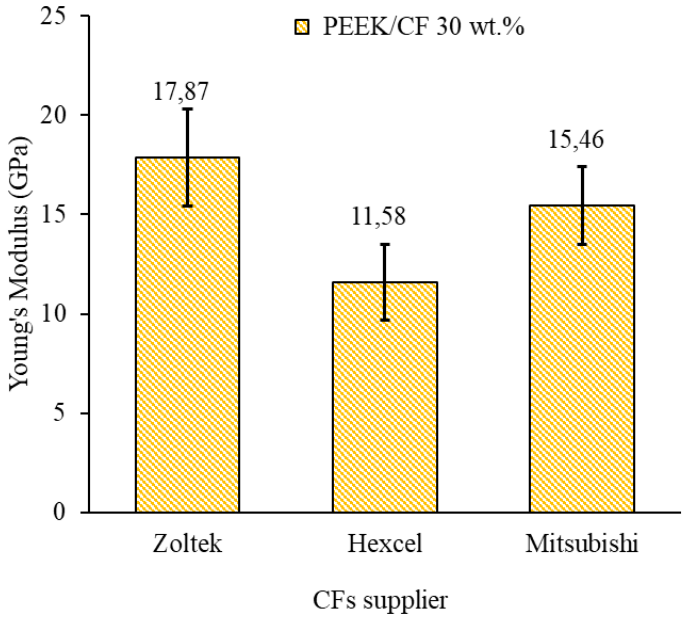

Figure G.2 Young's modulus of PEEK/CF composite filaments with different types of CFs mixed with the Bülher and Brabender extruders

APPENDIX H MECHANICAL PROPERTIES OF FDM DOGBONE SAMPLES PRINTED IN TH FW CONFIGURATION

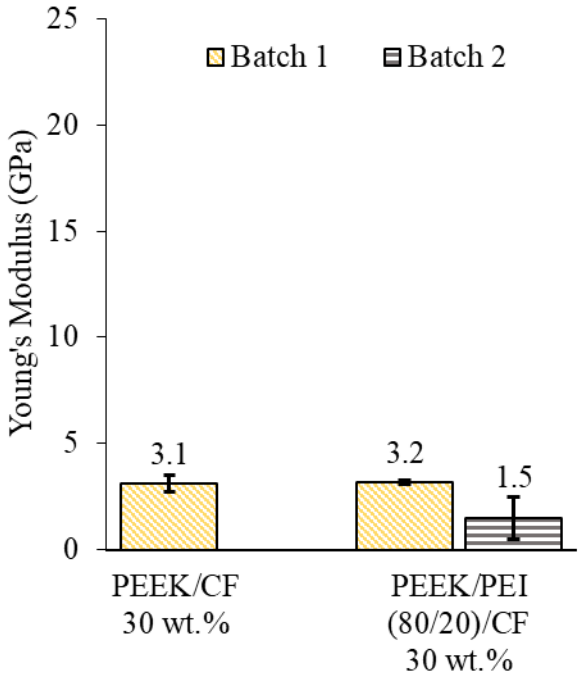

Figure H.1 Young's modulus of PEEK/CF 30wt.% dogbone samples printed in the FW configuration

APPENDIX I PRINTING PARAMETERS FOR THE SANDWICH PANELS

Table I.1 Printing parameters for PLA and CFR PA and Neat PA sandwich panels on the Raise3D model Pro2

Printing parameter	**PLA**	**CFR PA**	**Neat PA**
Extrusion temperature (°C)	210	255	255
Bed temperature (°C)	60	80	80
Chamber temperature (°C)	N/A	N/A	N/A
Extrusion width (mm)	0,4	0,3	0,3
Extrusion multiplier	0,9	0,83	0,83
Printing speed (mm/s)	60 mm/s	60 mm/s	60 mm/s
Infill angle (°)	± 45	± 45	± 45
Infill percentage (%)	100	100	100
Number of shell	2	2	2
Retraction speed (mm/s)	60	60	60
Retraction distance (mm)	50	50	50
Cooling fan	60% (100% for bridging)	60% (100% for bridging)	60% (100% for bridging)

APPENDIX J FOUR RESONATORS CONFIGURATION

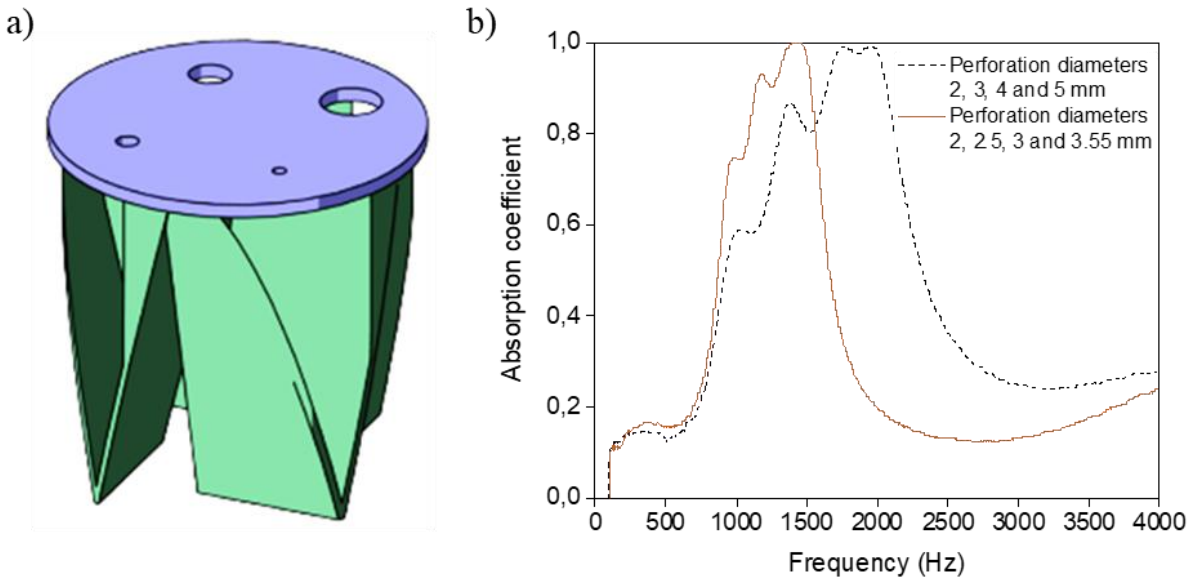

Figure J.1 a) Schematic of the samples for acoustic tests featuring four apertures. b) Absorption coefficient of two samples featuring four resonators with a neck thickness 3 mm and resonators diameters of 2, 3, 4, 5 mm and 2, 2.5, 3, 3.5 mm.